Automatic Segmentation of Airway Wall Components in Optical Coherence Tomography Images

by
Rashika Raizada

A THESIS SUBMITTED IN PARTIAL FULFILLMENT
OF THE REQUIREMENTS FOR THE DEGREE OF
BACHELOR OF APPLIED SCIENCE

in the
School of Engineering Science

SIMON FRASER UNIVERSITY
January 17, 2015

APPROVAL

Name: Rashika Raizada

Degree: Bachelor of Applied Science

Title of Thesis: Automatic Segmentation of Airway Wall Components in Optical Coherence Tomography Images

Examining Committee:

Dr. Kamal Gupta, P.Eng
Director, School of Engineering Science, SFU

Co-academic Supervisor:

Dr. Mirza F. Beg, P.Eng
Professor, School of Engineering Science, SFU

Technical Supervisor:

Dr. Pierre M. Lane, P.Eng
Senior Scientist, BC Cancer Research Centre
Associate Professor, School of Engineering Science, SFU

Co-academic Supervisor/ Committee member:

Dr. Marinko V. Sarunic, P.Eng
Associate Professor, School of Engineering Science, SFU

Date Approved: ____________________

Abstract

This thesis presents the investigation and experimental results on various image processing techniques as well as segmentation and analysis of volumetric Porcine Airway data. The Porcine airway data was acquired using Optical Coherence Tomography (OCT) using a fiber based probe. The data set used in this project comprised of ten Porcine Airway volumes. Six frames were manually segmented by two expert observers per porcine airway volume. Three hundred frames were automatically segmented in this thesis project per porcine airway volume and were compared against the manually segmented frames. Root mean square errors and Jaccard similarity were used to compare the segmentation contours and Bland-Altman plots were used to compare measurements with the manually segmented frames. Results and analysis of all three hundred frames automatically segmented form the final results of the thesis project.

Acknowledgements

This thesis would not have been possible without the help of my supervisors Dr. Pierre M. Lane and Dr. Mirza Faisal Beg, my committee member, Dr. Marinko V. Sarunic and my mentor Sieun Lee. I would like to take this opportunity to thank Dr. Lane for his continuous efforts and patience in helping me complete this thesis project as well as the thesis write up. I would also like to thank Dr. Lane, Dr. Anthony Lee and Dr. Miranda Kirby for their invaluable advice and guide in the clinical relevance as well as the performance measurement tools, as well as for helping me through the different image processing tools. I would also like to thank Dr. Beg for his help and support throughout the course of this project and I would also like to thank Dr. Beg for his guidance with the image processing and analysis techniques and his endless encouragement. Furthermore, I would like to thank Sieun Lee for her continuous help with the graph cut algorithm and also for her extremely helpful and kind attitude while helping me with all the lab rules as well as for her guidance regarding image processing techniques and for the thesis write up. I would also like to thank Dr. Marinko V. Sarunic for his invaluable advice and encouragement throughout the thesis project and also for his extremely helpful opinions on image processing and presentation improvements. Furthermore, I would like to thank all the members of the Medical Image Analysis Lab, Dr. Pradeep Reddy Ramana, Amanmeet Garg, Dr. Karteek Popuri, Masoud S. Nosrati and Donghuan as well the undergraduate program secretary, Margaret Crandell for their help and support throughout the length of my thesis. Finally, I would like to thank my parents Asit Raizada, Rumi Raizada and my younger sister, Aarushi Raizada for their love and support.

+Table of Contents

List of Tables

List of Figures

Chapter 1: Introduction

Airway Imaging

There is an increasing interest in the investigation of airway wall structure as highly prevalent lung diseases such as asthma and chronic obstructive pulmonary disease (COPD) are characterized by significant airway remodelling. COPD is a progressive disease that can lead to lung cancer. In a 2008 study, it was shown that COPD was responsible for 10% of the lung cancer cases reported in non-smokers [1]. Both asthma and COPD are obstructive airway diseases that involve airway inflammation, airway obstruction (AO) and airway hyper-responsiveness (AHR). Both airway inflammation and airway obstruction have structural components that can serve as biomarkers for these diseases [2]. Imaging the airway can therefore help improve the diagnosis and management of these lung conditions that are characterized by the remodelling of the airway wall structure. Furthermore, AO is the end product of airway inflammation and thus imaging for inflammation can be the key to early detection.

COPD and Asthma

Chronic Obstructive Pulmonary Disease (COPD)

Definition and Overview

The world Health Organization defines COPD as "a lung disease characterized by chronic obstruction of lung airflow that interferes with normal breathing." COPD is a progressive disease as it is known to exacerbate with time. COPD is considered an umbrella term that includes two main lung conditions namely emphysema and chronic bronchitis [NIH, 2013].

COPD is the fourth leading cause of death in Canada [3] and up untill 2005, over 700,000 patients in Canada were diagnosed with COPD.

Pathophysiology

COPD is characterized by reduction in lung function, including airflow limitation, which can be significantly attributed to airway remodelling. Cell damage, airway narrowing and inflammation of the airways due to recruitment of cells like neutrophils, macrophages and CD8 T lymphocytes constitute airway remodelling [4]. Airway remodelling, causing obstruction of airflow, mainly occurs in the smaller airways. Small airways are known as the "silent zones" [5] of the lungs, as they contribute minimally to the overall airflow resistance in a healthy lung and often go unnoticed in the diagnostic procedures.

Chronic Bronchitis

Chronic Bronchitis is similar to airway obstruction. In chronic bronchitis, however, the obstruction is predominantly found in the small airways that are less than 2 mm in diameter [6]. Chronic Bronchitis is characterized by inflammation in the epithelium of the central airways that are 4 mm or larger in internal diameter [7]. Furthermore, thickening of the bronchial walls is another significant characteristic of chronic bronchitis. This thickening is mainly a result of deposition of connective tissue in the layers of bronchi. [8]

Emphysema

In Emphysema, which involves the destruction of lung parenchyma [9], the lungs undergo a functional change wherein their elastic tissue gets replaced by inelastic fibrotic tissue. As a result of this replacement, the lungs lose their elastic recoil causing the patients to experience hyperinflation. This premature collapse of the airways leads to air trapping, reduction in expiratory volume, and even impairment of gas exchange. [10]. Emphysema also involves appearance of cyst-like emphysematous areas called bulla in the lungs which are surgically removed in some severe obstructive cases.

Asthma

Asthma is a chronic inflammatory respiratory disease that causes difficulty in breathing and frequent episodes of wheezing, coughing and shortness of breath known as "asthma attacks" [11].

Asthma affects 300 million people worldwide and leads to 250, 000 casualties annually [12]. In Canada, Asthma affects 8.5% of the entire population [13] and 20 children and 500 adults are estimated to die attributing to asthma [3].

Most of the deaths in asthma cases occur due to misdiagnosis or under diagnosis and advancement in imaging and early detection can therefore be ideal to help eradicate this cause.

Pathophysiology

Asthma affects the airways and makes them inflamed and sensitive overtime. Airway obstruction and excessive mucus production is also associated with asthma symptoms which causes restriction of airflow in the patients, further reducing lung function [11]. Airway remodelling, in asthma, includes airway wall thickening and airway inflammation. However, airway wall inflammation in asthma, unlike COPD, occurs due to recruitment of eosinophils and CD4 T lymphocytes [4].

Current Diagnostic Techniques

Functional diagnosis

Spirometry

One of the symptoms of COPD involves residual air in the lungs after the expiration stage. For example, in Emphysema, as mentioned earlier, changes in the lung tissue decreases the elastic recoil of the lungs responsible for emptying the air spaces in the lungs thus reducing maximum expiratory flow.

A spirometer is an instrument that can measure this residual volume indirectly by measuring lung function. It measures how much air is inhaled and exhaled and also how fast the exhalation is occurring by measuring the following:

- Peak Expiratory Flow Rate (PEFR) refers to how quickly the patient can exhale the air out
- Forced Expiratory Volume in 1 second (FEV_1) refers to how much air the patient can exhale in 1 second

The procedure of using a spirometer for diagnostic purposes is referred to as spirometry. Spirometry is capable of detecting COPD in its early stages before the symptoms become apparent. However small airways have been shown to be a major site of obstruction in the early stages that cannot be detected by spirometry as small airway obstruction does not have a significant functional impact. Furthermore, lung function can be altered without the presence of lung diseases. For example, airflow limitation can occur due to the patterns of the folding of the mucosal membrane. Spirometry in this case can result in false positives.

Structural diagnosis

Bronchoscopy

The procedure of imaging an airway with a bronchoscope is referred to as bronchoscopy. The procedure is used for diagnosis as well as management of airway and chest diseases. A bronchoscope is an instrument that helps clinicians examine the internal structure of the airways for lesions, tumors and inflammations.

Since both COPD and Asthma are characterized by airway remodelling, bronchoscopy is often used for observing inflammations and determining the appropriate treatment. Bronchoscopy is also used during the treatment of airway thickening- that often occurs in Asthma patients- as it allows the doctors to observe the result of the treatment such as balloon dilation in real time.

Chest X-Ray

X rays are electromagnetic waves which are on the order of an angstrom (10^{-10}). X-ray imaging involves sending ionising radiation through the organ of interest and results in internal pictures of the organ. Different tissues have different absorption characteristics and appear light or dark accordingly. Therefore changes in the appearance of the tissues and other structures can provide useful information regarding the diagnoses and management of a disease such as COPD and asthma.

A chest X ray is often suggested by physicians to patients suffering from airway obstruction as a means of confirming the diagnosis. X ray results also help in ruling out other diseases or conditions associated with airway disease-like symptoms such as heart failure.

Spiral CT

Computed Tomography (CT) is another imaging method that is often employed for the accurate diagnosis of COPD. It uses x rays and computer processing to achieve cross-sectional images of the organ of interest. Spiral CT employs scanning in a spiral or helical pattern in order to increase the imaging resolution.

CT helps distinguish COPD from other causes of COPD-like symptoms and can also be used for the management and treatment of COPD. For example CT can help determine if surgery is an appropriate approach of COPD management in a patient. CT can also distinguish between the different phenotypes of COPD namely airway obstruction versus emphysematous lungs [14]. Furthermore, CT scanning has also been shown useful in measuring the disease's severity and extent on a regional basis, in particular emphysema [15]

CT is increasingly used for the diagnosis of emphysema as it can detect the emphysematous areas (bulla) as well as destruction of lung parenchyma. Figure 1 shows CT images of a healthy control patient (left) and a patient with emphysema (right). Presence of bulla as well as lung parenchyma destruction are clearly evident in the figure on the right.

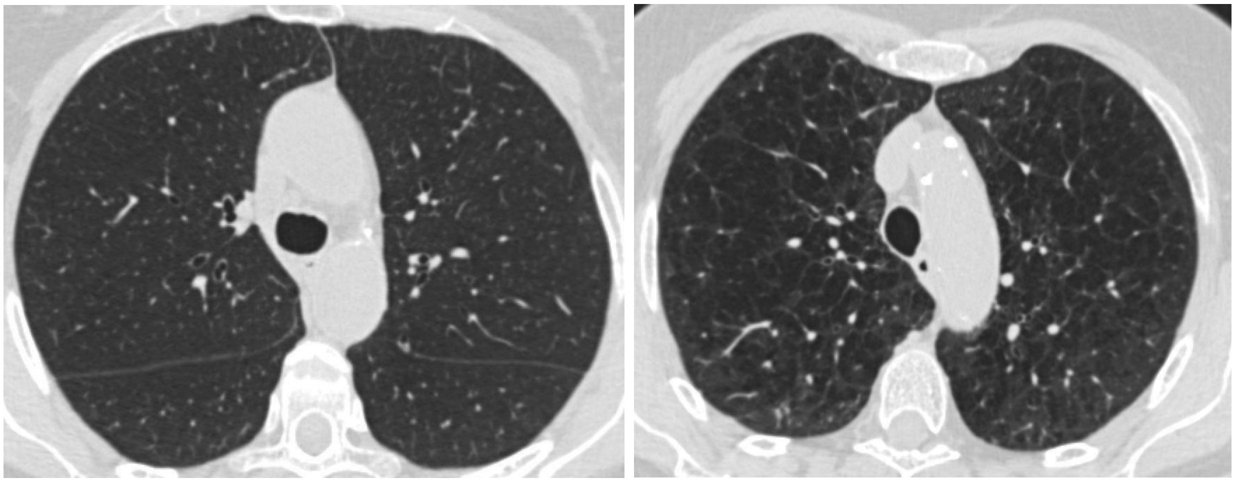

Figure 1: Left: control Smoker with no emphysema and Right: GOLD stage 1 Emphysema patient

OCT

Optical Coherence Tomography (OCT) is another imaging technique that can be used for non-invasive in-vivo imaging of the airways without the use of harmful contrasting agents. OCT uses light and interference to examine the structural changes in the tissue.

OCT can penetrate up to 1mm into the tissue and thus can provide not only structural information on the surface like bronchoscopy, but also below the tissue surface thus allowing very early detection of signs of airway remodelling which are below the surface level.

Segmentation of various airway wall components from Airway OCT images can highlight airway remodelling. Furthermore, automated segmentation can provide a non-invasive, safe, fast and reliable method for understanding the progression of diseases such as COPD and Asthma.

Goal of thesis

The goal of this project is to automate the segmentation of various layers- mucosal and sub-mucosal layers, as well as the cartilage- in the Porcine Airway images acquired using Optical

Coherence Tomography with the aim of extending the algorithm to Human airway segmentation in the future. This can help highlight the advantages of Optical Coherence Tomography as an imaging modality as well as provide an insight into the morphological changes that are associated with various lung diseases such as COPD, lung cancer and asthma. The segmentation will be able to segment 3D volume sets of OCT images directly and hence will provide more accurate segmentation compared to 2D slice by slice segmentation.

Thesis Structure

This document is divided into 9 chapters. The first chapter provides the motivation behind this thesis project along with the thesis goal and structure. Chapter 2 provides the anatomy of the airways and the histology for layers of interest in the diagnosis of COPD and Asthma. Chapter 3 provides an overview of the image acquisition technique, Optical Coherence Tomography, employed for the data set used in this project. Chapter 3 also includes a description of the OCT system used and the importance of OCT imaging in Airway disease management. Chapter 4 provides an overview of related work done previously in the segmentation of OCT images and airway images, as well as the related work done using the main algorithm employed in this project. Chapters 5 and 6 provide the theory and methods for the design and implementation of the segmentation. Chapter 7, 8 and 9 provides results, discussion, conclusion and future work.

Chapter 2: Airway Anatomy and Histology

Airway Anatomy

Airway wall layers starting from the lumen in the radial direction to the airway wall, in order, are epithelium, basement membrane, lamina propria, sub mucosa, cartilage, and Adventitia as shown in figure 2 [16]. The epithelium is the inner most layer of the airway (closest to the luminal space). Lamina propria, sometimes also referred to as the sub epithelial zone is composed of collagen and elastin fibres as well as blood vessels and connective tissue. The epithelium, basement membrane and lamina propria are together referred to as the mucosal layer or the mucosa. The sub-mucosa is composed of smooth muscles and the adventitia is composed of connective tissue for connecting the airway to the surrounding structures.

The smooth muscle and cartilaginous layer become less distinctly defined in different generations of airways. For example in small airways cartilage layer completely disappears and smooth muscle predominates between lamina propria and adventitia. For this reason, airways can be subdivided into 3 major layers for the purpose of investigating airway remodelling in COPD and Asthma patients: mucosa, sub-mucosa and adventitia. When adventitia is not clearly visible, the entire region after lamina propria is considered as the sub-mucosa [16].

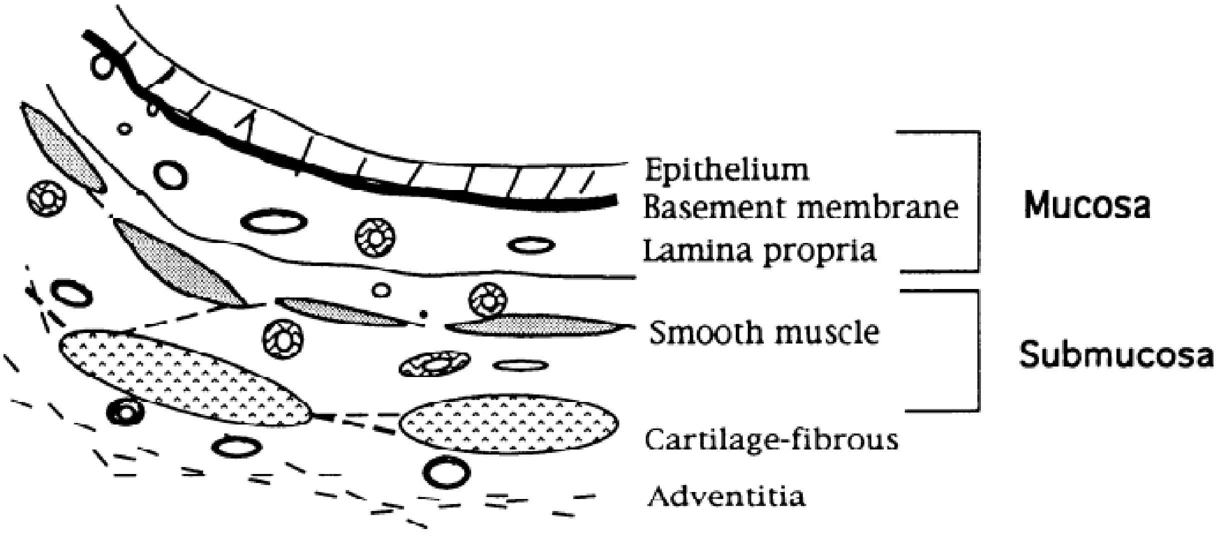

Figure 2: Airway wall layers [16]

This division was proposed by A. Bai and agreed upon by various researchers [16] for the following reasons:

1. These layers have distinct composition
2. Pathophysiology of different airway diseases may result in specific and exclusive remodelling of one layer only
3. The mechanism behind structural alterations such as thickening of each layer may be different
4. Thickening of individual layers have different impacts on lung function

Healthy Lung

Healthy lungs are defined by the presence of all the identified anatomical airway wall layers. Since histology remains the gold for detecting anatomical structures in any biological tissue, a healthy lung histology image is which clearly demarcates the different layers in the airway anatomy. These layers are the epithelium (E), the lamina propria (LP), the smooth muscle layer (SM), and the cartilage(C). The figure below shows a histology image of a healthy lung. This figure shows another layer-the perichondrium, a layer of connective tissue that surrounds the cartilage.

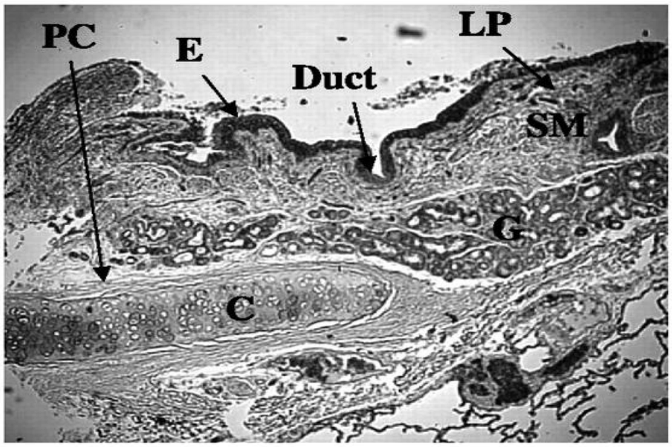

Figure 3: Histology of a healthy human airway

COPD

Airways of the COPD patients undergo structural remodelling due to a chronic inflammatory response. COPD is characterized by a significant amount of bronchial wall thickening [16]. However, the basement membrane thickness in particular is unchanged as compared to the healthy lungs [4]. COPD, particularly chronic bronchitis is marked by squamous metaplasia where the epithelial cells become more squamous (rectangular) in appearance [4]. Figure 4a shows a histology image of a lung with squamous metaplasia.

Asthma

Asthma patients also undergo chronic inflammation of the airways, but have some characteristics distinct from COPD patients. Airways of asthma patients have substantial thickening of the basement membrane and smooth muscle layer and also a significant amount of disintegration of the epithelium [4]. Figure 4b shows a histology image of the mucosa of an asthma patient. It can clearly be observed that the epithelial layer has considerably disappeared, and the basement membrane is thickened.

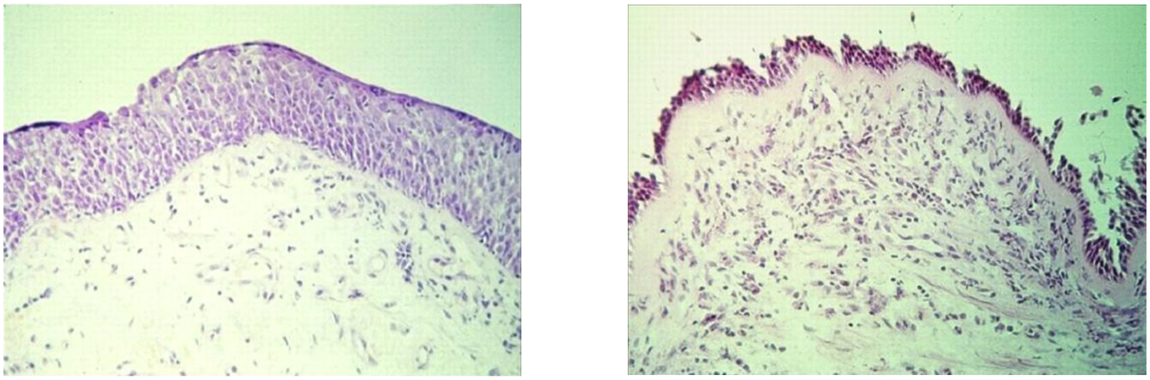

Figure 4: a)(left) Airway histology of a smoker with metaplasia and b) (right) Airway histology of asthma patient

Image analysis and measurements (airway area)

Imaging the airway can help improve the diagnosis and management of lung conditions like asthma and COPD as they are capable of detecting the structural changes in the airway wall structures that serve as biomarkers for the diseases. The analysis of the structural changes, however, is incomplete without the quantification of the changes. Image processing and segmentation prove as excellent tools, aiding in the analysis procedure of the airway wall structure.

It has been shown that, in healthy lungs (irrespective of the inflation state of the lungs), the internal perimeter of the airway wall basement membrane is relatively constant [16]. Thus, keeping this as the reference, structural changes in the layers such as thickening of the basement membrane, can be quantified. Another significant structural feature is the pattern of the folding of the mucosal membrane and Lambert [17] showed that the pattern is quite variable and can lead to airway narrowing and impede smooth muscle contraction thus limiting airflow. Therefore segmentation of the lamina propria along with analysis of the folding patterns can help eliminate false positives that may result from functional tests and hence help in the correct management of the condition.

Three major layers of interest have been shown to undergo significant changes in COPD and Asthma patients. As a result image segmentation and area measurement studies have seen tremendous growth. For example a study segmented airway lumen and airway outer walls and measured the total airway wall area [18].

Chapter 3: Optical Coherence Tomography and Data acquisition

OCT Overview

Optical Coherence Tomography (OCT) is a relatively new imaging technique that is non-invasive and uses light waves to image millimeters into the tissue with micrometer resolution [10 to 20 um]. OCT typically uses infrared wavelengths for imaging, as the longer wavelengths penetrate deeper into the tissue. OCT results in stacks of images that can be rendered into a 3D volume. OCT can be understood as an optical analogue of ultrasound with sound waves replaced by light waves which provides a comparatively better resolution with a compromise on imaging depth. A qualitative chart of the trade-off between imaging depth, resolution and imaging space is shown for different imaging modalities in figure 4 .

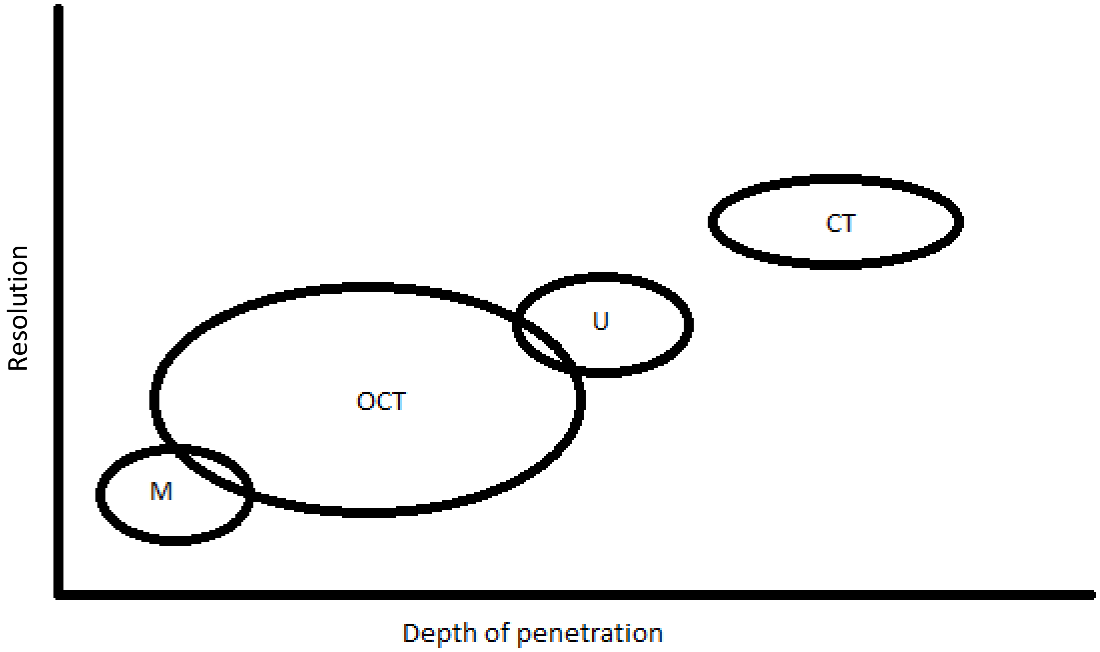

Figure 5: Comparison of different imaging modalities in terms of resolution and imaging depth. M: Microscopy, OCT, U: ultrasound, CT

As can be seen in figure 2, microscopy provides the best resolution [~1um] but the lowest imaging depth among the imaging modalities shown as it can only penetrate up to 100 um into the tissue [19]. As a result, microscopy is often done on thin slices of tissue after removal from the organ of interest. This is often a disadvantage as it is invasive. Ultrasound on the other hand is capable of imaging deeper into the tissue (few cm) allowing in vivo imaging. This however is done at the cost of image resolution which is in the range of 0.1 to 1 mm depending on the frequency of the sound waves employed. Computed Tomography is another structural imaging modality that is capable of imaging an entire organ with even greater penetration depth but a relatively poor resolution (≤0.2mm). CT, however, involves the use of harmful contrasting agents such as X-rays.

OCT bridges the gap between microscopy and ultrasound imaging with a resolution better than that of ultrasound (5-15 um, [20]) and depth of penetration better than microscopy (~ 1mm). Furthermore OCT is an optical imaging modality which is non-invasive and does not involve the use of harmful contrasting agents. Moreover due to the optical nature of the modality, it is possible to combine OCT with other imaging tools and designs such as endoscopes and catheters to image difficult to reach areas of the human body such as small airways.

OCT Theory

The principle behind OCT is low coherence interferometry. OCT set up involves a broadband light source, so that it has a short coherence length for rejection of background noise and for imaging only the layers of interest in the tissue because they lie within the coherence length of the light source. This broadband light is split equally into two directions with one going to the sample of interest and the other going to a path known as the 'reference arm' where it hits a mirror and reflects. The light wave going to the sample gets scattered from most of the tissue sample and gets reflected from the layers of interest. The scattered beam loses coherence and does not match the path length of the reference arm within the tolerance referred to as the coherence length (i.e. is not within the coherence length of the source) and hence does not interfere and thus gets rejected. The beam coming from the layers of interest however is within the coherence length of the source and thus interferes with the reflected beam coming from the 'reference arm' creating fringes. These fringes are then processed to give 2D image slices which stack together to result in a 3D volume.

The coherence length that keeps the layers of interest but rejects the other information from the tissue of interest is a function of the spectral width of the light source. As can be seen from the equation below, broader the bandwidth, lower the coherence length. l_c is the coherence length, λ is the centre wavelength of the light source and $\Delta\lambda$ is the bandwidth of the light source. Coherence length is also the axial resolution of the system that is how well the system can resolve two objects in the axial direction.

$$l_c = \frac{2\ln 2\lambda^2}{\pi \Delta\lambda} \tag{1}$$

The transverse resolution of the system is given by the beam size of the focused spot of the scanning beam. This is given by the equation below, where ω_o is half of the beam waste, f is the focal distance of the final focussing lens of the system, also known as the working distance, λ is the central wavelength of the light source and d is the diameter of the beam incident at the final focussing lens.

$$2\omega_o = \frac{4\lambda f}{\pi d} \tag{2}$$

There are two different methods of obtaining the path length mismatch for rejection of background and interference of light from desired layers with light from the 'reference' path. This gives rise to two kinds of OCT systems: Time Domain OCT and Frequency Domain OCT

Time Domain OCT

In time domain, the mirror of the reference arm is translated longitudinally, varying the length of the path the light travels in this direction, this is known as the path length. Light also travels to the sample arm (where the tissue sample is) and gets reflected and meets the light coming from the reference arm. The difference between the lengths of the paths the light takes in the direction of the sample and in the direction of the reference mirror is called the path length difference. If this path length difference is within the coherence length of the broadband light source of the system, then the light from both the sample and reference arms interferes and produces images otherwise no interference occurs.

Fourier Domain (FD) OCT

In frequency domain or Fourier domain OCT, the reference arm path length is fixed and the depth information is encoded by the frequency. Interferometric data is therefore acquired as a function of wavenumber which is the reciprocal of the wavelength ($k = 1/\lambda$). The different layers of interest in a sample are detected at different wavelengths of the source.

Based on the method of separation of wavelengths, Fourier domain OCT is of two types- spectral domain OCT and swept source OCT. In spectral domain OCT system, the wavelengths are separated in pixels at the detector whereas in swept source OCT system, the wavelengths are separated in time using a grating. In both cases, however, data of all the layers of interest is acquired simultaneously without the requirement of changing the reference path length. Hence FD OCT is faster than time domain OCT systems.

Our OCT system – Probe geometry/data acquisition

The OCT system used for acquiring the images used in this project is a swept source OCT system from light labs, C7XR. The imaging was done with 0.9mm rotary pullback C7 Dragonfly probe [St. Jude Medical, St. Paul, MN]. The probe is such that the infrared light exits from it in a forward-looking direction with a measured angle of 68.5 degrees in air, and 74.7 degrees in PBS/formalin [21] from the axis of the probe. The laser source of the system is centred at 1310 nm which provides an axial resolution of 15µm. Cross-sectional images were acquired at a frame rate of 100 Hz and a 2 to 5mm/s pullback rate.

The probes used, were fiber-based probes which scan the airway in a helical pattern such that there is a radial (r) as well as azimuthal (θ) component along with a z component (length of imaged airway section) due to the pull-back imaging method. Thus the images are acquired in the polar coordinates (r, θ). The probe allows access to the hard to reach areas of the lung such as smaller airways where obstruction is most prevalent. Figure 6 shows the optical design for the probe used for acquiring the data along with the propagation of the scanning infrared beam.

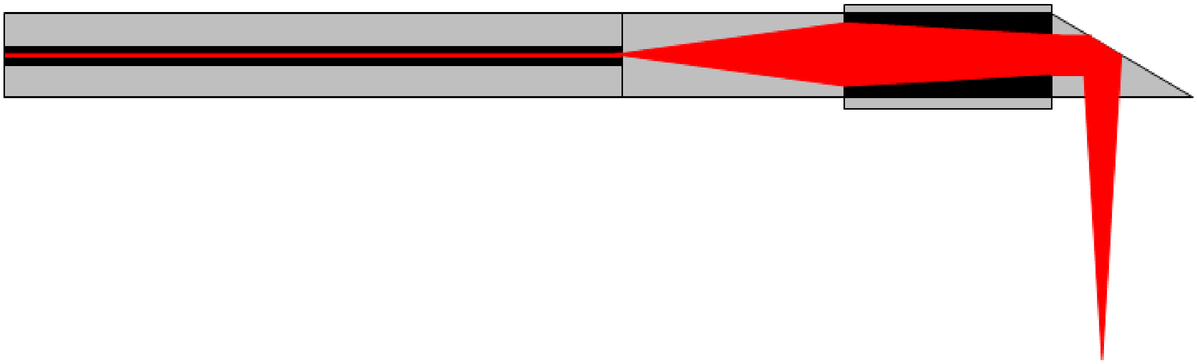

Figure 6: Probe showing light propagation

OCT of Airways

With its high resolution imaging capabilities, OCT images of the airway can help detect the morphological changes associated with airway diseases. OCT imaging has been used for detecting morphological changes in airways such as bronchial lesions [22], inflammation [23] and neoplastic pathology [20] with the aim of early lung cancer detection, COPD as well as asthma. Research is moving in the direction of replacing the current invasive biopsy procedure with non-invasive optical biopsy using OCT.

The figure below shows differences between OCT lung images of healthy controls and patients suffering from airway pathology. Lung inflammation and squamous metaplasia of the epithelium are characteristic features of COPD and as shown below, OCT can detect these changes due to its micrometre resolution and depth imaging capabilities. Furthermore, with the help of a probe, these changes can be detected non-invasively as well as without the use of harmful contrasting agents.

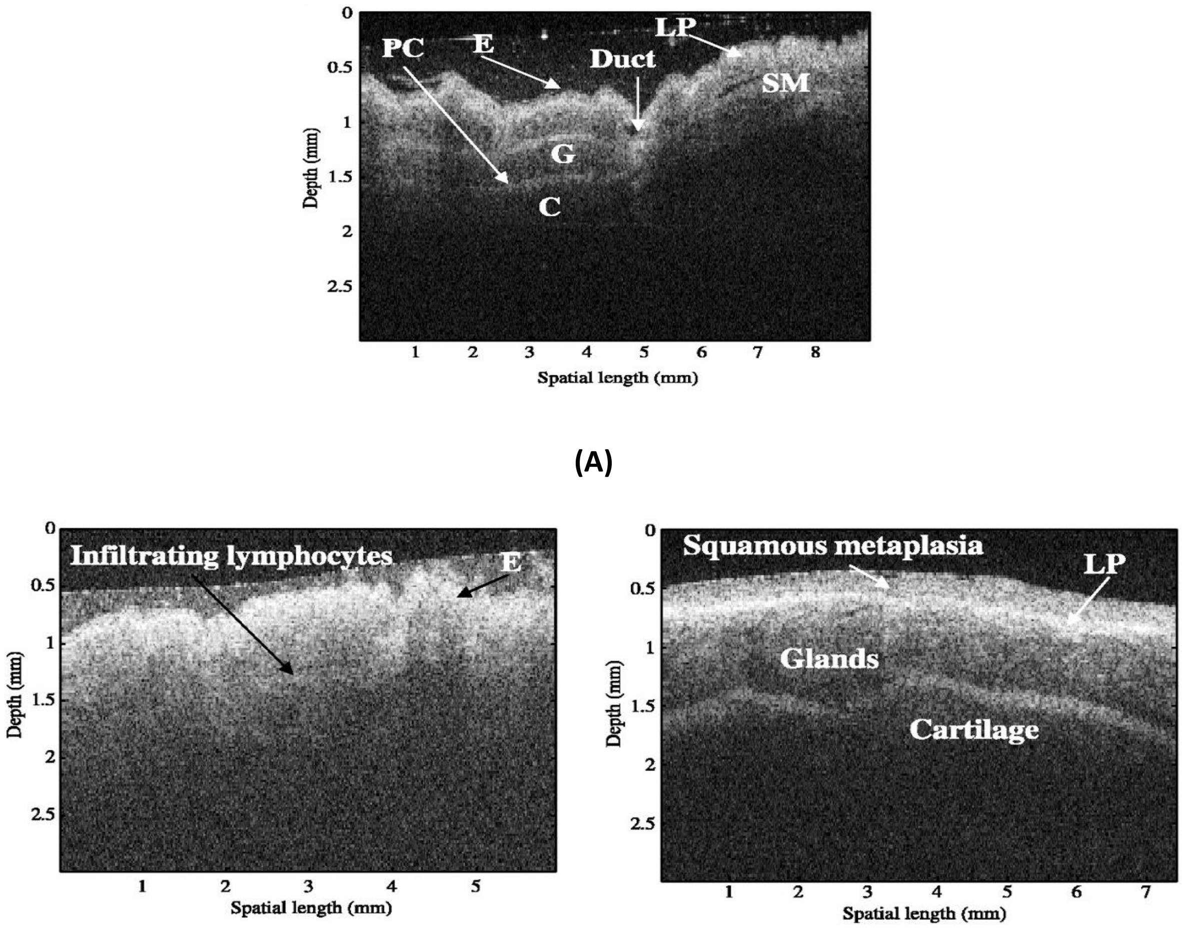

(A)

(B) **(C)**

Figure 7: [A] Healthy Lung Airway showing epithelium (E), Lamina Propria (LP), Smooth Muscle (SM), Cartilage (C), perichondrium (PC); [B] Lung Airway with inflammation; [C] Lung Airway showing Squamous metaplasia of the epithelium

Segmentation

Examination and quantification of specific features such as the mucosa, submucosa as well as the cartilage can give insight into the progression of lung diseases. Segmentation is the most critical step in the process of quantification of any structural feature. Furthermore, it also distinguishes between hard-to-separate layers and makes qualitative assessment of features trivial and quantitative measurements possible.

Manual

Manual segmentation results in precise extraction of the components of interest from the images for analysis. Currently, experts trained in anatomy are responsible for accurate segmentation of images for medical purposes.

Manual segmentation is, however, is very time consuming. For example, patient OCT image databases in clinics consist of large number of collected OCT volumes and each of those volumes are further composed of large number of 2D frames. The OCT system used in this project for example, results in volumes composed of 1200 frames. Manual segmentation can only tackle 2D frames, rather than the entire volume and it is extremely time consuming to segment each frame of every volume. Moreover, manual segmentation also suffers from observer's bias and the observer may segment differently based on the contrast and brightness of the display screen as well. Furthermore, different observers achieve different segmentation results; up to 22% of disagreement among observers has been reported [24].

Automated

Patient databases in clinics consist of large number of collected OCT volumes and each of those volumes are further composed of large number of 2D frames. Manual segmentation can only tackle 2D frames, rather than the entire volume and it is extremely time consuming to segment each frame of every volume. Moreover, manual segmentation also suffers from observer's bias. For complete examination of structural features in a lung volume, an automated algorithm must thus be applied for efficient and accurate segmentation of the images. For complete examination of structural features in a lung volume, an automated algorithm must thus be applied for efficient and accurate segmentation of the images. Automated segmentation has the added benefit of repeatability as well.

Chapter 4: Previous Work

Not much has been reported in segmentation of OCT airway wall layers. Airway tree segmentation has been reported using graph cuts [27]. Furthermore, manual segmentation of airway wall and airway wall layers has been done and correlated with CT images [28] and histology [18] respectively. Manual segmentation, however as mentioned earlier, has many disadvantages. Automation of airway wall segmentation have been reported [29] & [18], but the approaches are two dimensional and cannot be easily extended to 3D. The data sets are acquired as a collection of over 1000 2D images which provide structural information about the airway. Therefore, there is a need for a true 3D segmentation algorithm that is much faster and also relies on information from adjacent frames when segmenting a 2D frame for increasing the segmentation accuracy which may be compromised due to the presence of a branch point or artefact in one frame.

Airways/OCT

Manual segmentation background

In Lung OCT images, manual segmentation has been popularly used for accuracy of measurements. Groups have used manual segmentation of airway wall in order to successfully correlate its thickness measurements in OCT and CT images [18]. Hence, OCT segmentation can be reliably used for measuring airway wall thickness, which is a significant biomarker for COPD and Asthma. Furthermore, manual segmentation of airway wall layers -the mucosa, submucosa and cartilage - has also been done and successfully compared with histology image segmentation [21]. Since histology is considered as the gold standard in disease diagnosis based on structural remodelling, OCT segmentation agreeing with histology is highly encouraging.

Although Manual segmentation shows great promise, it faces multiple disadvantages as mentioned earlier and therefore there is a need for automated segmentation methods that are robust as well as significantly faster.

Automated Segmentation Background

Automated Segmentation of lung OCT images has been tricky and highly underexplored. With high correlation of OCT image measurements with CT and histology measurements, OCT image segmentation seems highly promising in the diagnosis and management of diseases such as COPD, asthma and even lung cancer.

Classical segmentation techniques have been used for automating image segmentation. Heydarian et. al proposed a fully automated algorithm for airway wall segmentation using Fuzzy c-means or K means clustering and Otsu thresholding [25]. There is, however, a lack of validation of the results against ground truth. Another group, Kirby et.al, developed an algorithm for automatically segmenting airway wall components – lumen, mucosa, submucosa, and cartilage. The results were used for airway wall area measurements which were also compared against manual segmentation results and measurements as well as histology [18].

Selectivity of image frames used

Both the automated segmentation methods, however, relied upon the selection of certain frames and the algorithm was developed to work specifically on similar frames. The segmentation algorithm, in other words, was a 2D segmentation algorithm. The algorithms thus addressed the manual segmentation's disadvantages of inter and intra observer variability; however they did not address the time-consuming nature of segmentation completely.

Lack of volumetric segmentation

For complete information on airway remodelling, the entire volumetric data is required to be segmented and used for measurements. Currently there is no algorithm that segments volumetric OCT airway data, because of the highly varying nature of the images that constitute the volume.

VOLUMETRIC SEGMENTATION on Similar data

Automated Volumetric (3D) segmentation has, however, been reported for OCT retinal layer segmentation [26] using graph-cut based segmentation algorithm. Graph-cut based segmentation has also been used for segmentation of intra-vascular ultrasound (IVUS) images [27].

Segmentation of Retinal layers for choroid thickness measurement

OCT is becoming increasingly popular in ophthalmology due to its high resolution, in vivo imaging capabilities. Furthermore, Choroid thickness has been shown to correlate with age-related macular degeneration. Thus, previously, groups have implemented graph cut segmentation algorithms to segment the retinal layers for measuring the choroid thickness [26]. These results have also been validated for repeatability as well as for agreement with segmentation results of expert raters [26]. Figure 8 shows the automatic segmentation result for choroid thickness measurement.

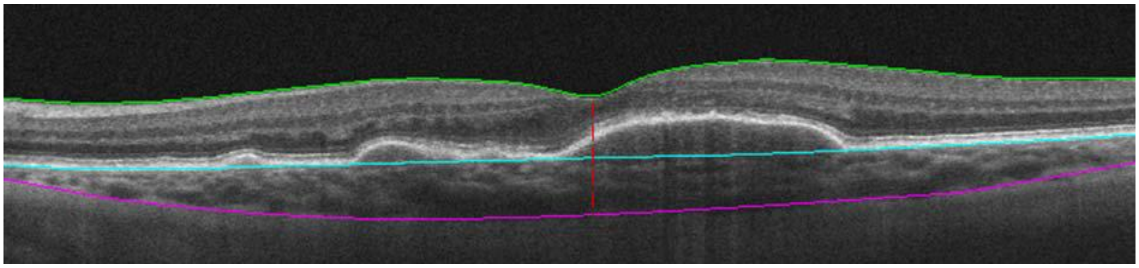

Figure 8: Retinal layer segmentation using 3D graph cut algorithm [25]

Intra Vascular Ultrasound Images

Graph cut algorithms have also been used for segmenting intra-vascular ultrasound images, which are much worse in resolution than OCT images [27]. The segmentation, however, also involved machine learning along with the graph cut method and the result is shown in Figure 9.

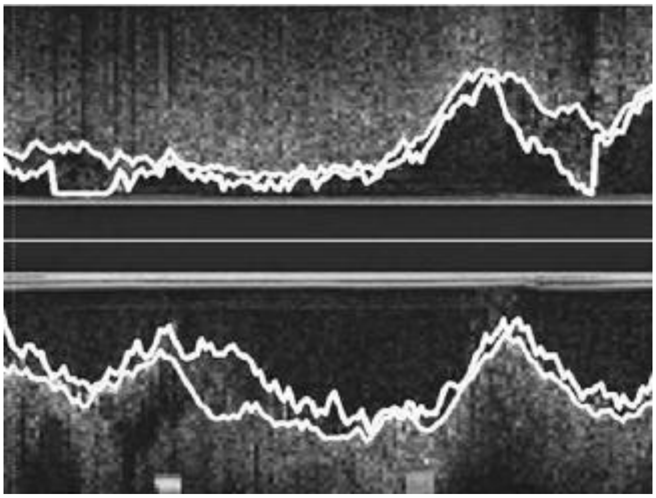

Figure 9: Segmentation of Intra vascular ultrasound images [26]

Chapter 5: Image Processing Theory

This chapter describes brief theories of the various pre-processing and segmentation methods tried in this project.

Image Pre-Processing

Smoothing

i. Non-linear Complex Diffusion filter (NCDF) for de-speckling

Linear smoothing filters include averaging and Gaussian smoothing which reduce the noise/speckle in the images at the cost of losing important information in the images due to blurring. A non-linear filter is an edge-preserving filter and non-linear complex diffusion works by facilitating diffusion in the smooth areas of the image while attenuating at the image edges [30]. This is done by having the diffusion coefficient in ncdf of the following form:

$$D = \frac{\exp(i\theta)}{1 + \left(\frac{Im(I)}{\kappa\theta}\right)^2}$$

Where i = $\sqrt{-1}$, θ is phase angle (~0), κ is a threshold parameter, I is the image and Im stands for the imaginary component. For small θ, the imaginary component of I is a smooth function of its second derivatives and the ratio $\frac{Im(I)}{\theta}$ is proportional to the Laplacian of I (in the limit when θ→ 0) leading to edge preservation [31]. The κ parameter modulates the spread of the diffusion coefficient at edges and homogenous regions where the Laplacian vanishes- increased diffusion in low intensity regions and decreased diffusion in high intensity regions of the image. Furthermore, the function employed in this project uses an adaptive approach where κ is modified locally such that κ increases in low-intensity regions and decreases in the high-intensity regions. This ensures edge- preservation smoothing.

ii. Bounded Variation smoothing

Bounded Variation (BV) smoothing is an edge preserving smoothing algorithm based on the BV norm. The smoothing works according to the following image de-noising equation:

$$E(I, I_0) = Q(I) + \lambda C(I, I_0)$$

Where I_0 is the degraded image and I is the restored image. Q (I) is the measure of the quality of the image based on a norm (in this case, BV norm), C(I, I_0) is the function of squared differences between the degraded and restored images and λ is a multiplier to penalise the differences. The specific restoration model is therefore:

$$E = \int_{\Omega} |\nabla I| dx + \lambda \int_{\Omega} |I - I_0|^2 dx$$

Where Ω is the volumetric region of interest. The restoration function, E, needs to be minimised for a good quality image. The minimization is performed using gradient descent, and a minimizer is incorporated in the equation:

$$div\left(\frac{\nabla I}{|\nabla I|}\right) + 2\,\lambda(I - I_0)$$

The BV smoothing equation therefore becomes:

$$\frac{\partial I}{\partial t} = |\nabla I|(div\frac{\nabla I}{|\nabla I|} - 2\,\lambda(I - I_0))$$

The iterative method of gradient descent follows the following equation:

$$I^{(n+1)} = I^{(n)} + \partial t \left|\nabla I^{(n)}\right| \left(div \frac{\nabla I^{(n)}}{|\nabla I^{(n)}|} - 2\,\lambda\left(I^{(n)} - I_0\right)\right)$$

By applying the iterative method of gradient descent, smoothing occurs along the edges not through the edges. The BV norm model preserves edges by handling discontinuities by computing finite-difference approximations of derivatives [32].

Pre-Segmentation Enhancements

Thresholding

i. Otsu

Otsu's method converts a gray scale image to a binary image by automatically selecting the optimum threshold. The optimum threshold is chosen such that the combined spread of the two intensities of the resulting binary image is minimal [33].

ii. Hysteresis

Hysteresis thresholding method converts gray scale images to binary using two threshold values, a low threshold and a high threshold. Hysteresis thresholding works by the assumption that edges of interest will form continuous curves in the images [34]. Thus, regions where low thresholded edges are not connected to the high thresholded pixels are discarded and regions where low thresholded edges are connected to the high thresholded edges are retained.

K means clustering

Clustering, as the name suggests, involves grouping number of pixels together to form sets or clusters based on a common property such as intensity. It is sometimes also considered as a thresholding method where multiple thresholds are used to segment respective multiple regions of an image.

This clustering method divides an image into K clusters and works as follows [35]:

i. K cluster centres are chosen

ii. Each pixel in the image is assigned to the cluster which minimizes the difference between the pixel and the cluster centre in terms of the distance, intensity or color (if the image is not a gray scale image)

iii. Cluster centre is recomputed by averaging all the pixels in that cluster

iv. Steps two and three are repeated until no pixels change clusters i.e. convergence is attained

Hessian-based Filtering

The filtering method was proposed by Alejandro F. Frangi and is used to enhance vessel-like or ridge-like features in an image (2D version) or volume (3D version). The method is based on the calculation of three eigenvalues of images from its hessian matrix which provides the second order information about the image [36]. The eigenvalue analysis gives the direction of the smallest curvature along the vessels present in the image [36].

Finally a measure is defined known as the 'second order structureness (s)' that depends on the eigenvalues ($\lambda_1, \lambda_2, \lambda_3$)and is low in the background and high in high contrast regions. The measure 's' along with two ratios R_B (which accounts for the deviation from blob like structure) and R_A (which distinguishes between plate-like and line-like structures) provides the function for 'vesselness' [36] :

$$V_0(s) = \begin{cases} 0 & if\ \lambda_2 > 0\ or\ \lambda_3 > 0 \\ \left(1 - exp\left(-\frac{R_A^2}{2\alpha^2}\right)\right) * exp\left(-\frac{R_B^2}{2\beta^2}\right) * (1 - exp\left(-\frac{S^2}{2c^2}\right)) & \end{cases}$$

Where α,β, and c are sensitivity thresholds.

Convex Hull

A convex hull of a set of pixels is the smallest envelope (convex set) that contains those pixels. A convex set is a set of points such that they contain all line segments connecting each pair of points. More formally, convex hulls of a set of pixels may be defined as the (unique) minimal convex set containing the pixels or the intersection of all convex sets containing the pixels [37].

Automated Segmentation

Graph cut

Graph- based segmentation converts the problem of segmentation into computation of minimum cost functions in a graph and thus is capable of yielding segmentation results in polynomial time. In this method, each pixel of the frame is considered as a node and edges (arcs) are assumed to exist between pixels of a chosen neighbourhood, thus forming a graph.

$$G = (V, E),$$

where V is the set of nodes and E is the set of arcs

A cost function determines whether an edge really exists between two nodes. These edges (arcs) in 2D are actually surfaces in 3D and nodes are voxels. There are two key features of the cost function:

- **Gradient constraint or data cost**- A constraint on intensity differences across boundaries for edge (boundary) detection
- **Smoothness constraint or smooth cost**- A constraint on intensity differences between pixels in a chosen neighbourhood for partitioning of arcs (2D). The intensity differences

are specified as weights on the edges and the validity of an edge is determined by whether or not its weight is within the constraint. In 3D, this constraint is on intensity differences among voxels to determine whether a surface exists between the nodes (voxels).

For example: Assuming the unwrapped image frames are in the xy planes and that z represents the direction perpendicular to the image frames. Consider the volume as a3D matrix with z being the volumes in columns, then for image volume I(x,y,z):

Smoothness constraint => Δx, Δy

and if I(x,y,z) and I(x+1,y,z') are two voxels such that $|z-z'| \leq \Delta x$

and I((x,y,z) and I(x,y+1,z') are two voxels such that $|z-z'| \leq \Delta y$ then a surface exists between these voxels. i.e. 3D connectivity is guaranteed [38].

Gradient constraint => δ^l, δ^u (called min and max separation constraints respectively for related surfaces)

Having layer boundaries in a frame translates to having multiple surfaces in the image volume and the relation between the surfaces is also taken into consideration. As mentioned earlier, z axis is the column in the 3D matrix holding the image volume, so feasible surfaces exist in (let's say) column 1 and 2 if :

a node V(x,y,z) in column 1 is such that $z \geq \delta^u$ and a node V(x,y,z) in column 2 is such that $z < \delta^l$

These constraints are carefully chosen in order to ensure that connected nodes result in segmentation of the desired features in the image.

Chapter 6: Experimental Methods

This chapter describes the data set used in this project as well as the various methods that were applied to segment the airway wall components.

Data set

The volumetric data used in this project comprised of 10 Porcine Airways with 1201 frames each. 2 observers independently manually segmented selected 6 frames per pig volume data set for lumen, mucosa and submucosa. Thus ground truth comprised of 2 sets of segmentations per 6 frames per pig volume. This gave a total of 60 frames and 120 sets of segmentations for the 10 pig volumes under study.

Process flow

The main motivation behind this thesis project was to segment the airway wall components namely, lumen, mucosa, submucosa, and cartilage (which was marked by submucosa boundary and outer airway wall boundary) automatically due to their clinical importance in diagnosis. The flow chart presented in Figure 10 shows the different steps applied to achieve the segmentation results. The process flow was not always followed step-by-step for each experiment. Some steps were skipped in different experiments. As a result, various experiments resulted in only image preprocessing and they weren't used further for segmentation, while other experiments resulted in segmentation of only one of the desired layers and while the others resulted in segmentation of 2 or 3 layers of interest.

Method Flow chart:

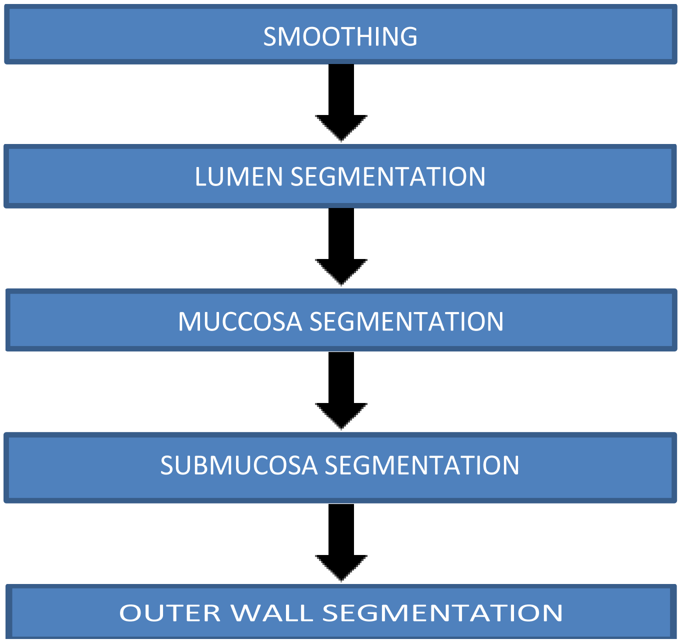

Figure 10: Experiment Flow Chart

Image Pre-processing

Smoothing

Optical coherence tomography images intrinsically suffer from speckle noise which makes edge detection difficult. The speckles are falsely detected as edges, because edges are detected at the pixel level. As a result, a smoothing filter is a necessary pre-processing tool. Three noise-reducing methods were experimented with.

a) Non-Complex Diffusion filter (NCDF[TMAX])

b) Bounded variation norm smoothing (BV [lambda, steps])

c) Frame Averaging (Avg [N])

Non-Complex diffusion filters were tried with diffusion times in the range of 0.75 to 3 seconds. BV smoothing was experimented with a lambda range of 0.1 to 0.001 and with iterations ranging between 6 and 15. Frame averaging was performed in the range of per 2 to 5 frames.

Outer Wall Segmentation

Pre-processing, Thresholding and Post-processing

The outer most wall of the airway is characterised by the end of all visible features in the image. There is a sharp distinction in the intensities at this boundary and therefore the airway's outer wall can be segmented using intensity-based thresholding. The following steps were taken to separate the airway wall components from the airway wall boundary:

i. De-speckling
ii. Gaussian high pass filtering
iii. Otsu's thresholding
iv. Morphological closing
v. Sobel's Edge detection
vi. Edge dilation
vii. Edge erosion
viii. Overlay of resulting boundary on original image

Hessian-based Filtering for cartilage segmentation followed by Otsu's thresholding and Convex Hulls

Cartilage appear as vessel like structures in the OCT images and thus Hessian-based vessel detection filters were used for enhancing the cartilage in the images. Hessian based-Frangi vesselness filter was also previously employed in the 2D segmentation algorithm for cartilage detection [17]. Despeckle filtering was used followed by High Pass Gaussian filtering followed by Frangi_Hessian function. Cartilage outer boundary also marks the outer airway wall. Therefore, a convex hull was applied on images that were hessian-filtered for cartilage and thresholded using Otsu's method. The bottom boundary of the convex envelope can be considered as the outer airway wall boundary.

2D Segmentation of Lumen, Mucosa and Submucosa

Clustering

2D K-means clustering was applied on the images to bundle pixels of similar intensities together as one layer. Despeckle filtering was applied before the clustering algorithm to reduce noise. Results with K values of 3, 5, 7, 9 and 11 were compared. Despeckle was considered as a meaningful filter for noise removal, since clustering had been previously used along with despeckle filtering on the Cartesian form of the data for segmentation of airway wall components in 2D for select frames (6 per pig in total 10 pigs) [17].

Combined 2D and 3D Lumen and Mucosa segmentation

Hysteresis followed by morphological opening and closing

It was also observed that the mucosal layer (more specifically the lamina propria) was the brightest region of the airway, hence 3D thresholding (hyteresis) was employed as a preprocessing method solely for better detection of lamina propria by significantly enhancing the layer’s intensity using thresholding. Thresholding was further followed by 2D morphological opening and closing to get continuous inner and outer boundaries for the lamina propria which in turn resulted in the segmentation of Lumen and Mucosa.

3D Automated Segmentation

Data Cropping

The original 2D image size of the volumetric data was 968X504 pixels. The images, however, consisted of large regions of unnecessary data (e.g. blank spaces). The images were therefore cropped at 500 pixels, after careful inspection, to reduce the size to 499X504 pixels for 3D segmentation. The matlab command imcrop() was used directly on the volumetric data for this purpose.

3D Graph cut

Sieun Lee at Medical Image Analysis lab (MIAL) implemented a graph cut algorithm which was previously successfully used to automatically segment retinal layers in the human eye for diagnosis of glaucoma [25]. Both 3D and 2D versions of the graph cut algorithm implemented in matlab were available for use. Since previous work in graph cut algorithms demonstrated success in segmenting retinal layers in the human eye, polar form of the pig lung data was used instead of previously popularly used Cartesian form because the airway layers in polar form resembled retinal layers.

The characteristics of the airway wall layers that made 3D graph-cut algorithm a good fit for the segmentation task at hand:

- Layers of interest had different intensities
- They were continuous through multiple adjacent frames
- They were coupled with one another in terms of their contours
- They had distinct directionality- one layer was always brighter than the other and the subsequent layer was always darker than the previous layer.

The implemented 3D graph cut algorithm had the following crucial parameters that controlled the segmentation:

1. Slope of the layer of interest (param1)
2. Intensity-based direction of the edge corresponding to the layer of interest (param2)
    a. Dark to bright
    b. Bright to dark
3. Existence of a prior layer of similarly varying edge (param3)
4. Distance between the prior edge and the new edge of interest (param4)

    a. New edge is assumed to be below the prior edge. E.g. 30 indicates the new edge is 30 pixels below the previously segmented edge

5. Down sampling size (param5)
    a. This number divides the original volume to a smaller size for crude initial segmentation. E.g. [8, 4] will divide the volume by 8 and 4, taking one every 4 frames, every 4 A scans and every 8 pixels. The down-sampling is sequentially reduced in the segmentation steps like [8,4]-> [4,2]->[2,1]->[1,1] in order to get refined segmentation on the original volume size
6. Variation in the location of edge pixels along an image frame (param6)
    a. Higher number corresponds to highly varying edge pixel locations

    b. Lower number corresponds to a more restricted edge space

    c. Values are different for different downsampling steps as can be seen in table and usually only two values are chosen:
        i. One for crude (large down sampling size)
        ii. Another for fine (small down sampling size)

3D Lumen Segmentation

3D segmentation of the Lumen involved was performed in the following steps:

1. The probe was semi-automatically masked out. The probe outer sheath radius was manually estimated in pixels on the first frame and used to mask out the probe in the volume used.
2. Smoothing was applied using either the NCDF, BV, or the frame averaging method
3. 3D Graph cut segmentation was performed with different parameter sets

3D Lumen and Mucosa Segmentation

Mucosa segmentation was always performed after lumen segmentation, taking luminal boundary as the reference contour in the following steps:

1. Assume mucosa boundary is X pixels below lumen boundary
2. Mask pixels outside this search area [OPTIONAL]
3. 3D Graph Cut Segmentation with different parameter sets

3D graph cut was tried on the first available data set- PIG2, with the aim of detecting 2 layers of interest (lumen and mucosa). The implemented graph cut was previously used along with BV smoothing for segmenting retinal layers. The exact same settings and parameters were used on the first dataset as the first trial. Segmentation results with same graph cut parameters, but different BV smoothing parameters were compared. Segmentation results as a result of different graph cut parameter, and slope were also compared in order to improve segmentation of frames with approaching branching point.

Next, the parameters in the graph cut algorithm were further tweaked in order to achieve better results. It was observed that the key thing to working with graph cuts is that it needs to be really restricted to follow an expected path and look for layers of interest within the vicinity of the set number of pixels. The Allowable variation of slope of the layer contour was changed and the results were compared. Three hundred frames from PIG 2 Airway volume were segmented for two layers- lumen and mucosa. Segmentation was achieved sequentially using graph cut.

3D Lumen, Mucosa and Submucosa Segmentation

Submucosa segmentation was also performed after lumen segmentation either with additional masking outside the search area or without.

1. Assume submucosa boundary is Z>X pixel below lumen boundary.

2. Mask pixels outside this search area. [OPTIONAL]
3. 3D Graph Cut with lumen as the prior reference contour

The image processing and segmentation experiments are tabulated in Table 1 with the exact parameters used.

Parameter Optimization using RMS Analysis

The performance of the segmentation was quantified in order to choose the best parameter set. There were 6 manually segmented frames per PIG volume data set. Manual segmentation was done by two observers resulting in 2 sets of segmentations per frame. The manual segmentations from both observers served as the ground truth and were used for comparing the performance of the different parameters in the graph cut segmentation algorithm. A training set of 5 volume data sets was used to choose the best parameter set quantitatively. The first five among the volume datasets available formed the training set: PIG2, PIG3, PIG4, PIG5 and PIG6.

RMS error analysis was used against the ground truth frames as a means of performance measure. RMS errors of automated segmentation against each manual segmentation lower than the RMS inter-observer differences was considered as the ideal parameter set determining condition. The parameters were considered better than the other sets if the RMS errors reduced. Different pre-processing techniques or different parameters for pre-processing were used along with graph cut parameter tweaking. The parameters that resulted in the segmentation with the lowest RMS errors against ground truth was considered as the best set and was used for further analyses. The layers of interest- lumen, mucosa and submucosa- were detected sequentially.

The different experiments performed to achieve the different segmentation results in this project are summarised in Table 1 with the exact parameters and methods. The table also indicates the end results of the different experiments in terms of which layers were segmented, if any.

Table 1: List of Experiments

EXP	SMOOTHING	OTHER	LUMEN SEGMENTATION	MUCOSA SEGMENTATION	SUBMUCOSA SEGMENTATION	AIRWAY WALL SEGMENTATION
1	NCDF TMAX = 0.75, 2, 3 BV Steps = 6, 15 λ = 0.001, 0.01 Frame Averaging N = 3, 5		No	No	No	No
2	NCDF TMAX = 0.75	High pass (σ = 5) Otsu's Method Closing (disk, 50) Sobel Edge () Dilation (disk, 5) Erosion (disk, 3)	No	No	No	Yes
3	None	Hysteresis [low, high] = [0.25, 0.8], [0.8, 0.9], [0.82, 0.99] Open (disk, 70) Close (disk, 10)	Yes	Yes	No	No

EXP	**SMOOTHING**	**OTHER**	**LUMEN SEGMENTATION**	**MUCOSA SEGMENTATION**	**SUBMUCOSA SEGMENTATION**	**AIRWAY WALL SEGMENTATION**
4	NCDF TMAX = 0.75	K-Means Clustering K = 3, 5, 7, 9, 11	Yes	Yes	Yes	No
5	NCDF TMAX = 0.75	Hessian Frangi filter: range = [1, 20] step size = 5 Otsu's thresholding Convex Hull	No	No	No	Yes
6A	BV λ = 0.001 Steps = 6	Probe Masked out	GC Param1 = 4 Param2 = dark to bright Param3 = No prior Param4 = NA Param5 = ([8,4]>[4,2]>[2,1]>[1,1]) Param6 = 1	No Mask GC Param1 = 1 Param2 = bright to dark Param3 = yes Param4= 30 Param5 = ([8,4]>[4,2]>[2,1]>[1,1]) Param6 = 5	No	No
6B	BV λ = 0.001 Steps = 6	Probe Masked out	Same as above	Same as above	No	No
6C	BV λ = 0.005 Steps = 25	Probe Masked out	Same as above	Same as above except Param1 = 4	No	No
6D	BV λ = 0.001 Steps = 6	Probe Masked out	Same as above except Param6 = 10	Same as 6A except Param6 = 10	No	No
6E	BV λ = 0.001 Steps = 6	Probe Masked out	Same as 6A except Param6 =70	Same as above	No	No

EXP	SMOOTHING	OTHER	LUMEN SEGMENTATION	MUCOSA SEGMENTATION	SUBMUCOSA SEGMENTATION	AIRWAY WALL SEGMENTATION
6F	BV λ = 0.001 Steps = 6	Probe Masked out	Same as 6A except Param6 =2	Same as 6A except Param6 =2	No	No
6G	BV λ = 0.001 Steps = 6	Probe Masked out	Same as 6A except Param6 = 10	Same as 6A except Mask @ lumen + 40p Param6 = 10	No	No
7A	BV λ = 0.001 Steps = 6	Probe Masked out	Same as 6A except Param1 = 2	Same as 6A except Mask @ lumen + 50p Param1 = 4	No Mask GC Param1 = 4 Param2 = bright to dark Param3 = yes Param4 = 50 Param5 = ([8,4]>[4,2]>[2,1]>[1,1]) Param6 = 5	No
7B	BV λ = 0.001 Steps = 6	Same as 7A	Same as above	Same as above	Same as 7A except Mask @ lumen + 70p Param4 = 30	No
8A	Frame Averaging N = 5	Probe Masked out	Same as above	Same as above except Mask @ lumen + 70p Param4 = 40 Param6 = 5	Same as 7A	No
8B	BV λ = 0.001 Steps = 6	Probe Masked out	Same as above except Param1 = 2	No	No	No

EXP	**SMOOTHING**	**OTHER**	**LUMEN SEGMENTATION**	**MUCOSA SEGMENTATION**	**SUBMUCOSA SEGMENTATION**	**AIRWAY WALL SEGMENTATION**
8C.	Frame Averaging N= 5 BV λ = 0.001 Steps = 6	Probe Masked out	Same as above	No	No	No
8D.	BV λ = 0.001 Steps = 15	Probe Masked out	Same as above	Same as 8A except Param6 = 10	Same as 8A except Param4 = 70 Param6 = 20	No
8E.	NCDF TMAX=10 BV λ = 0.001 Steps = 15	Probe Masked out	Same as above	Same as above	Same as above	No
8F.	BV λ = 0.001 Steps = 6	Probe Masked out	Same as above	Same as above except Param5 = ([4,4]>[2,2]>[1,1])	Same as above except Param5 = ([4,4]>[2,2]>[1,1])	No

Preliminary Experiments

A variety of methods were experimented with to observe their effects on the segmentation of the desired layers of interest. These experiments were performed at the early stages of this project and failed to provide any meaningful results. The experimental methods for the preliminary experiments are shown in Table 2.

Table 2: Preliminary Experiments

Experiment	Methods	Failed?
Prelim1	1) NCDF (TMAX=0.75) 2) HighPass (σ = 5) 3) Otsu's Thresholding	Yes
Prelim2	1) HighPass (σ = 5) 2) Graph cut Parameters same as experiment 6A	Yes
Prelim3	3) BV λ = 0.001 Steps = 25 4) HighPass (σ = 5) 5) Graph cut Parameters same as experiment 6A	Yes
Prelim4	Phase Congruency	Yes

Offsets and calibration

The RMS errors calculated to quantify the goodness of the parameter sets were in pixels. A conversion factor was determined for the calibration of the RMS errors from pixels to mm. The images were 7 mm deep corresponding to 968 pixels. Therefore the conversion factor:

$$f_{pixel\ to\ mm} = \frac{7mm}{968\ pixels} = 0.00723\ mm\ pixel^{-1}$$

Furthermore, the A scans were also calibrated from pixels to the corresponding angle in radians. Each image frame consists of 504 A-scans covering a range of 2π radians. Hence, the conversion factor from pixels to radians for the A-scans was given by:

$$f_{pixel\ to\ rad} = \frac{2\pi\ \text{radians}}{504\ pixels} = 0.01246\ rad\ pixel^{-1}$$

The acquisition of the data also incorporated an offset in the measurements. This offset can be estimated by correctly placing the 7mm A-scan window corresponding to the outer sheath's radius value of 0.45 mm. The outer sheath was highly varying in nature. An estimate of the mean of the sheath radius was thus used as shown in Figure 11.

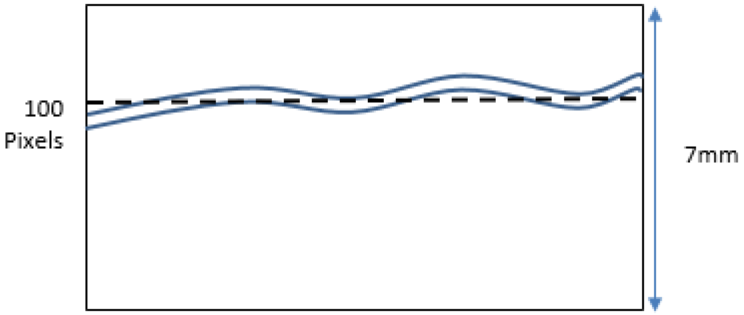

Figure 11: Figure depicting the offset estimation method

The corresponding value of the mean was then found in mm and subtracted from 0.45 mm to find the offset. The offsets were found for each volumetric data set and is reported in Table 3.

Table 3: Offsets calculated for different data sets

Data set	Offset (mm)
1	-0.273
2	-0.172
3	-0.107
4	-0.128
5	-0.078
6	-0.107
7	-0.201
8	-0.056
9	-0.034
10	-0.020

Chapter 7: Results and Discussion

This chapter presents the results of the various pre-processing and segmentation methods investigated in this thesis project. Brief discussions of the observed results are also included in this chapter.

Experiment 1

The aim of this experiment was to find the best parameters for smoothing using the different smoothing methods. The results for TMAX = 0.75, TMAX =2 and TMAX = 3 using non-complex 2D despeckling filter are presented below in Figure 12.

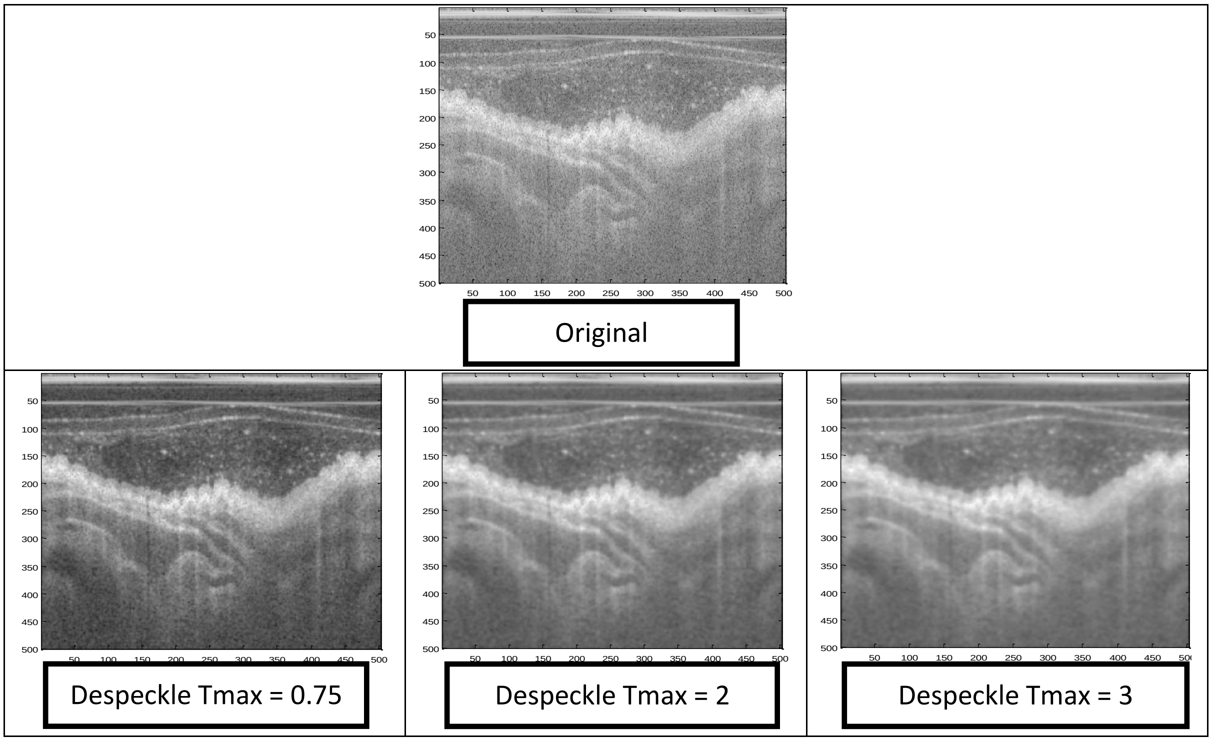

Original

Despeckle Tmax = 0.75

Despeckle Tmax = 2

Despeckle Tmax = 3

Figure 12: Results showing the effects of 2D Despeckling filter

The results for lamdas = 0.1 and 0.001 and for steps = 6 and 15, using BV smoothing method are presented in Figure 12.

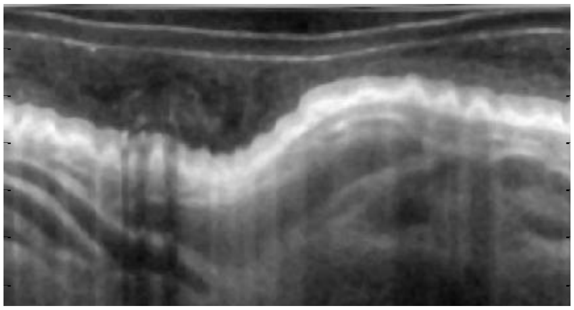

15 steps
Lambda =0.001

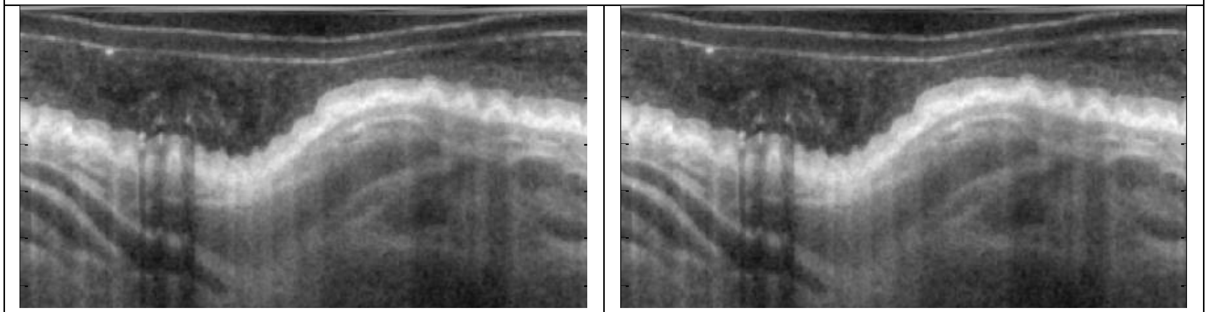

6 steps
Lambda =0.001

6 steps
Lambda =0.1

Figure 13: Results showing the effects of changing different parameters of the BV smoothing function

The results for N = 2 and 5, using frame averaging method are presented in Figure 14.

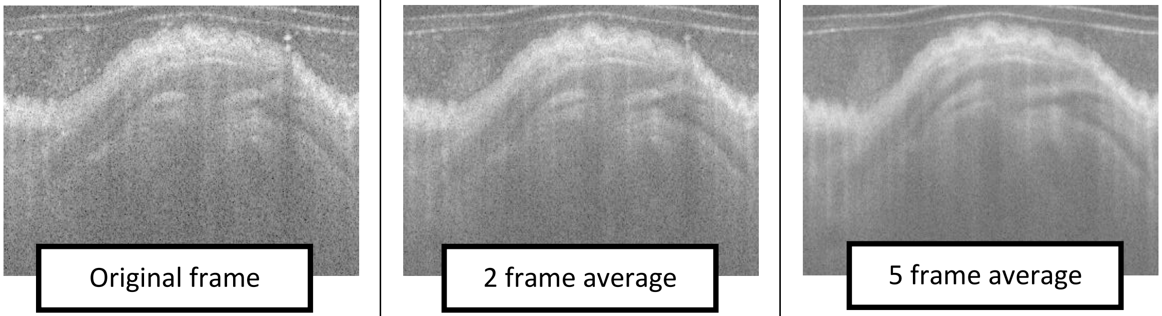

Original frame

2 frame average

5 frame average

Figure 14: Results showing frame averaging

Frame averaging is fast and reduces the speckle noise throughout the image, improving the overall appearance of the images. Frame averaging, however, results in the blurring of the edges reducing edge distinction. Despeckling filter results in smoothing, while preserving the edges. Higher diffusion times resulted in better images in terms of noise reduction. Only a 2D method for despeckling filter was available, therefore applying the despeckling filter to the entire volume was time consuming. BV smoothing method also smoothened images while preserving edges. BV smoothing had the added benefit of being much less time consuming compared to the despeckling filter. It was also observed that the smoothing was significantly sensitive to number of iterations or steps of the BV smoothing method compared to the lambda value. Higher values of number of steps resulted in better images in terms of noise reduction, but added to the time.

Experiment 2

The aim of this experiment was to segment the outer airway wall which is the outer boundary of the cartilage layer. Results of using Otsu's thresholding for segmenting outer wall layer are presented in Figure 15 below.

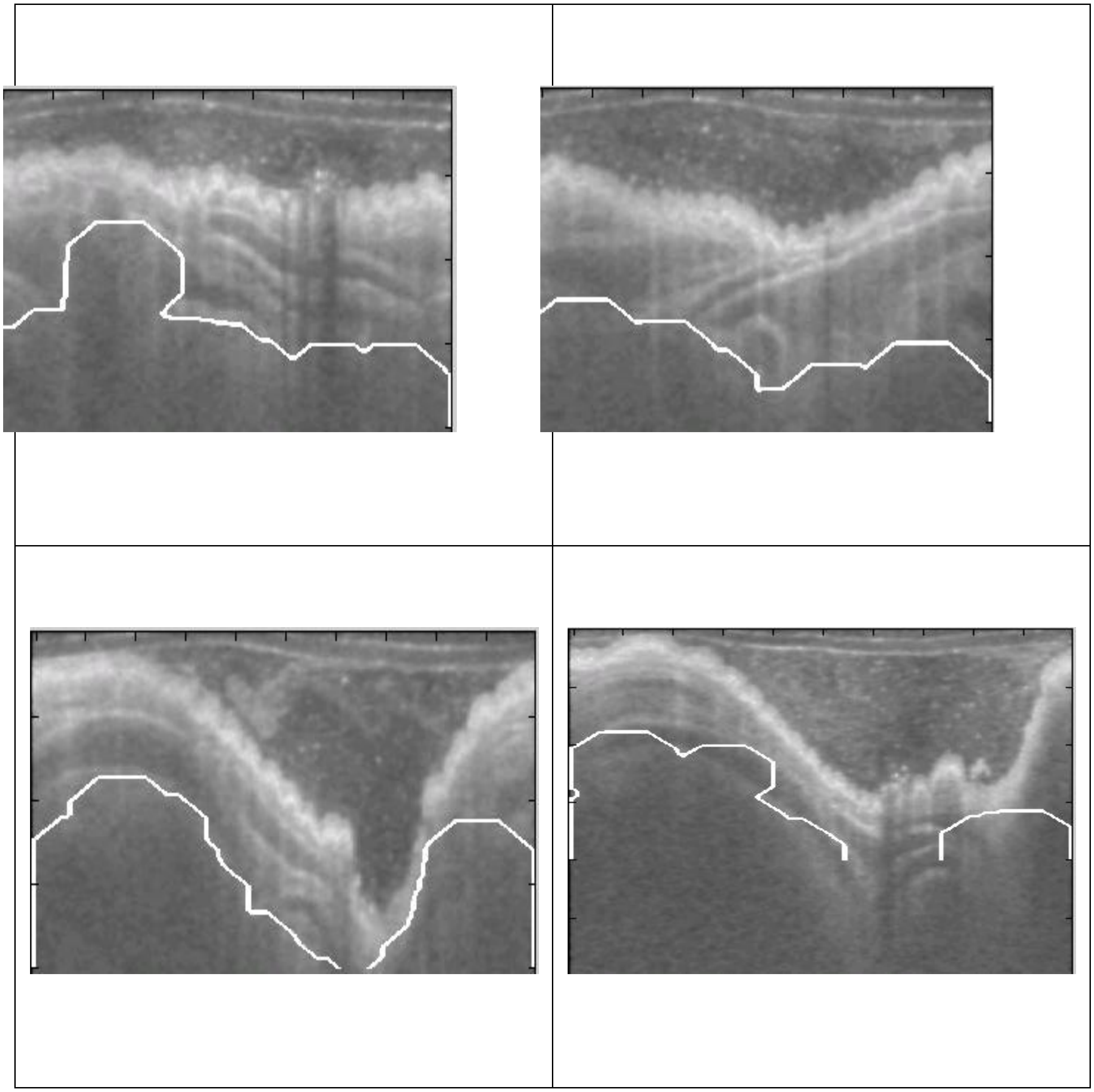

Figure 15: Otsu's Thresholding for Outer Wall Segmentation

As can be seen from Figure 15, the Otsu's thresholding method fails to achieve a continuous detection of the airway outer wall boundary. It also results in detection of undesired edges along the direction of

Axial scans (into the depth of the tissue). Furthermore, it is 2D method which varies with each frame and thus is not very cost effective to employ for segmentation of large volumetric data.

Experiment 3

The aim of this experiment was to segment the lamina propria whose boundaries mark the lumen and mucosa boundaries. Figure 16 shows the results of applying different low and high threshold values in 3D hysteresis function applied on the images.

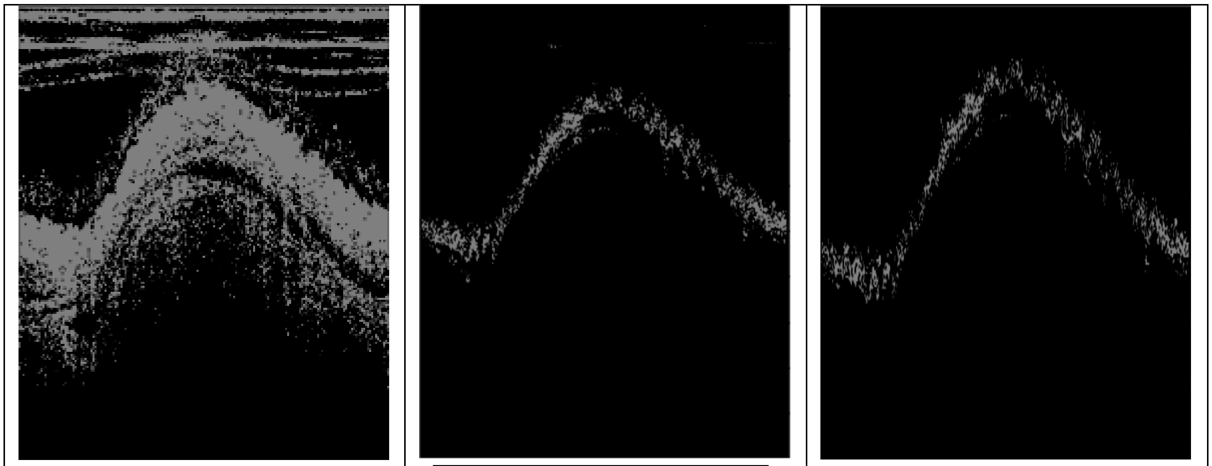

Low = 0.25, High = 0.8

Low = 0.8, High = 0.9

Low = 0.82, High = 0.99

Figure 16: Results showing the effects of different parameters of 3D hysteresis thresholding function

The parameter set of [0.82, 0.99] gave the best result among the trials investigated. The lamina Propria (brightest layer) was thresholded against all the other airway wall components. The thresholded layer, however, was not continuous. Figure 17 shows the results of applying morphological opening and closing on a frame thresholded with the best parameters for lamina propria.

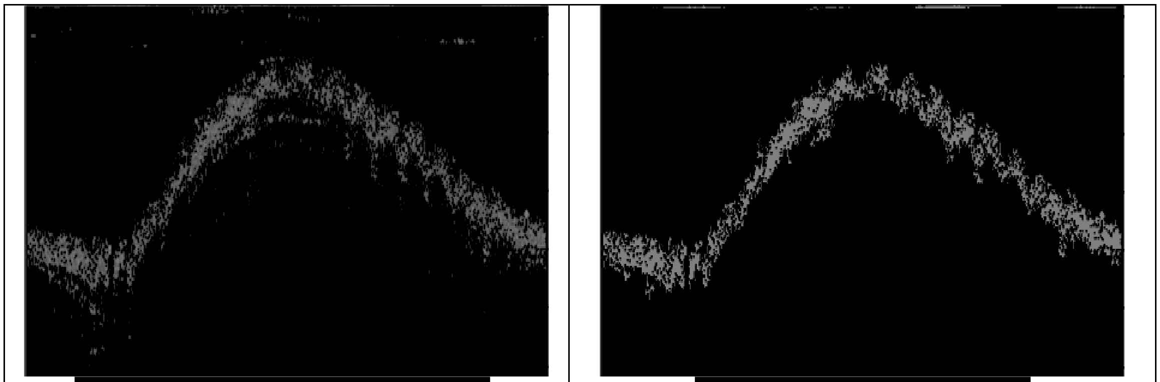

Thresholded frame

Opening, 70 pixels

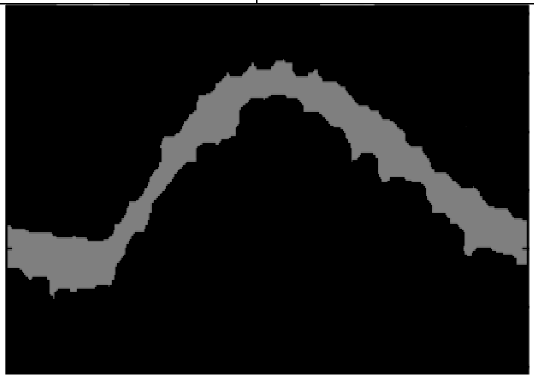

Closing, SE = disc 10

Figure 17: Results showing 2D- hysteresis followed by morphological opening and closing

The results of morphological opening and closing on thresholded images do provide enhancement of the brightest layer- lamina propria. The boundaries, however, are distorted as a result of inclusion of undesired pixels around the layer with similar intensities in the detection of the layer of interest. This is clinically unacceptable as the biomarkers for existence of diseases include changes in the thickness of the layers or decrease in the areas enclosed by layer boundaries as mentioned earlier in chapter 2 of this document.

Experiment 4

The aim of this experiment was to segment lumen, mucosa and submucosa using 2D clustering method with different parameters.

K-means Clustering

Figure 18 shows the results of clustering method applied with different K values, i.e. different numbers of expected clusters in an image.

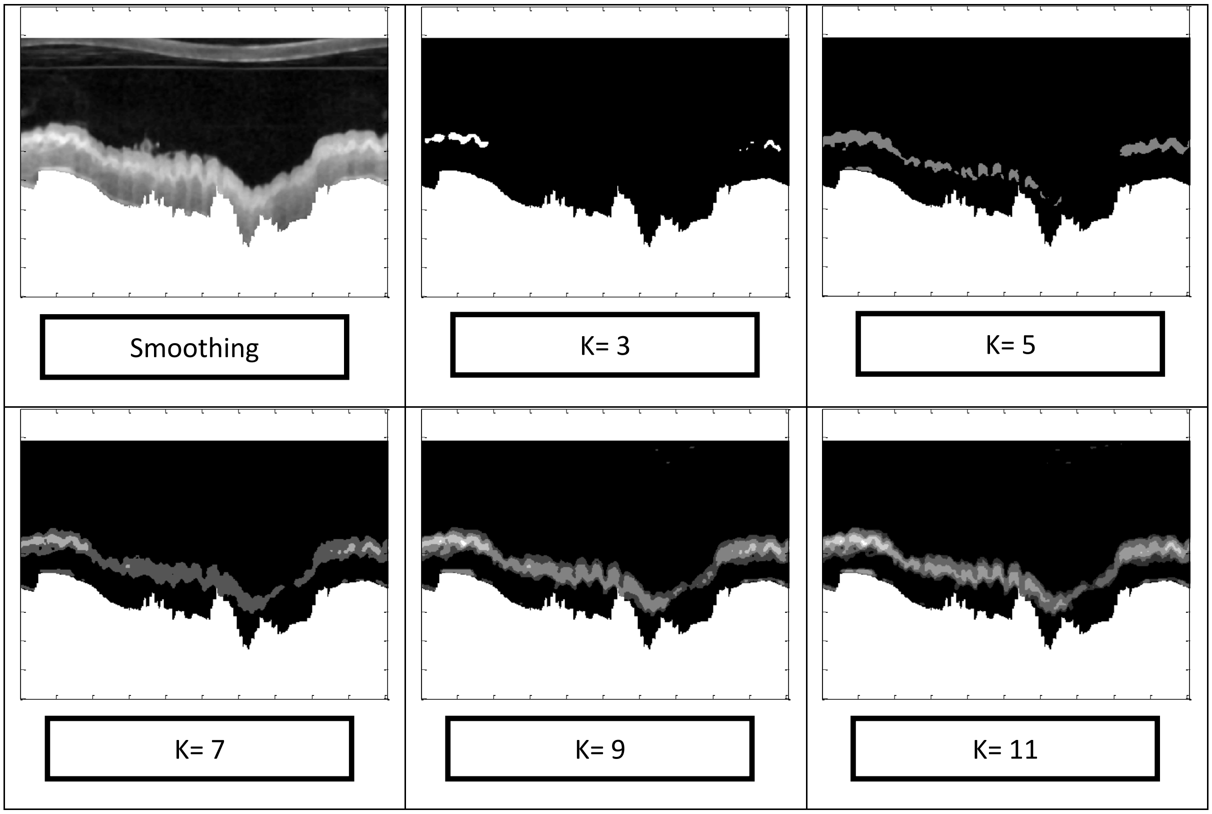

Figure 18: Results showing the effects of choosing various number of clusters

Clustering with K = 9 and K = 11 gave the best results among the investigated K values for enhancing the luminal boundary as well as the mucosa. The layers, however, still lacked continuity and the method is also a 2D method which makes it costly for segmenting a large number of frames that a volumetric data set is composed of.

Experiment 5

The aim of this experiment was to perform the segmentation of outer airway wall using convex hulls on the segmentation of the cartilage layer achieved using hessian-based Frangi filter and thresholding. Figure 19 show the results of hessian-based filtering applied for vessel-like-structure detection and the overlay of the result on the original frame.

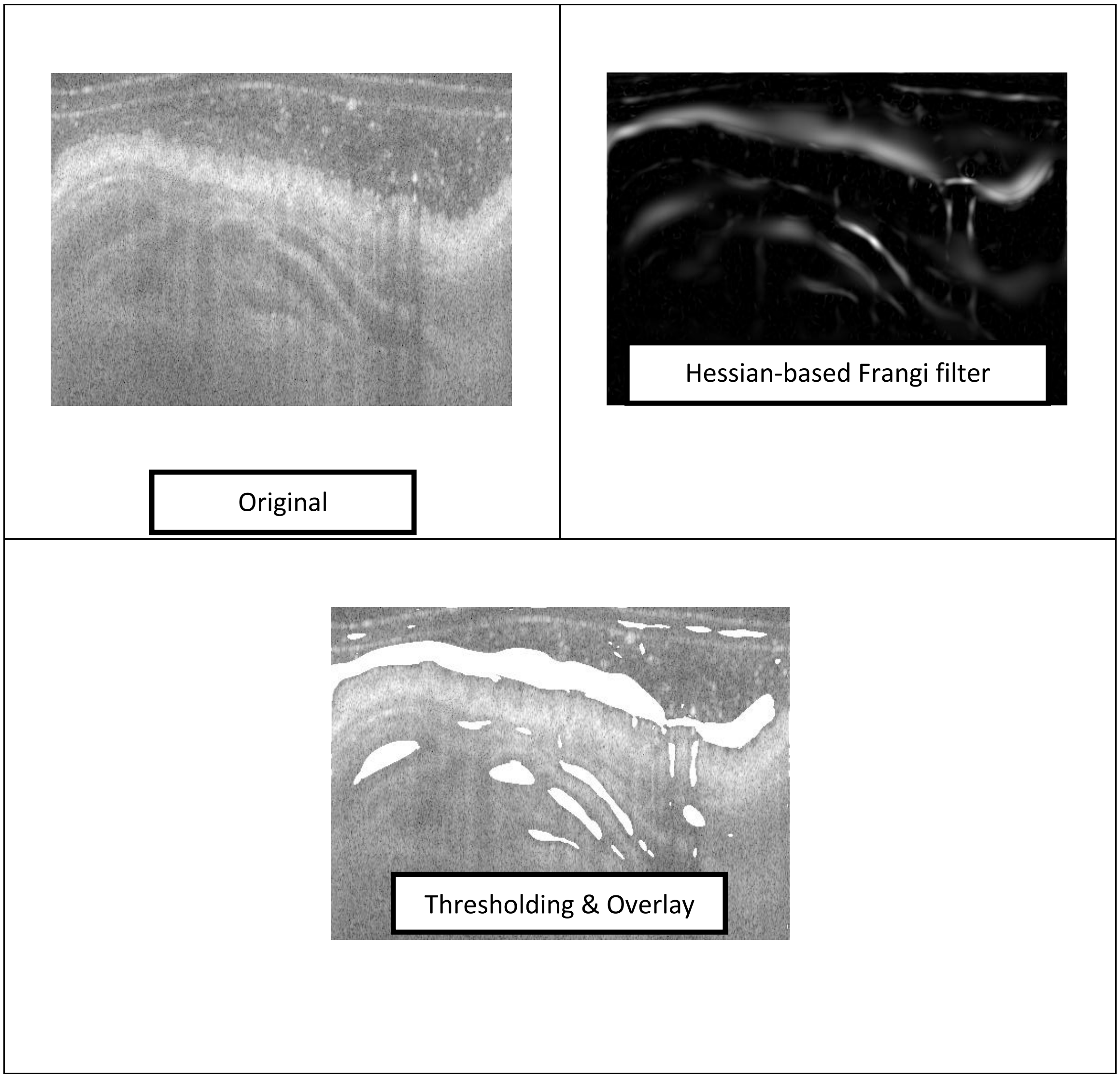

Figure 19: Results showing Hessian-based filtering followed by thresholding

Thresholding and overlaying was used to qualitatively analyse the detection of cartilage in the images. It was observed that hessian-based filtering can accurately detect the locations of the cartilage in the images, but not the actual size of the cartilage.

Figure 20 shows the result of applying thresholding and convex hull on an image showing the positions of cartilage after hessian-based filtering.

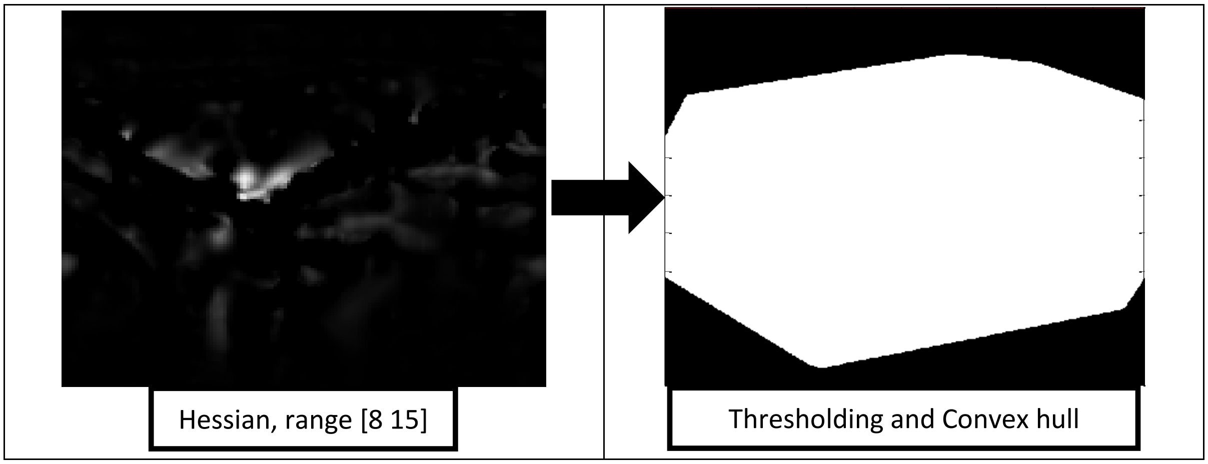

Figure 20: Results showing hessian based filtering followed by the results of applying the Convex hull

It was qualitatively observed that the convex hull successfully envelopes the end of the cartilage in the image. Thus, the lower boundary of the convex hull can be used as a crude segmentation of the outer wall of the airways.

Experiment 6

The aim of experiment 6 was to achieve the segmentation of Lumen and Mucosa. Initial tests of the Graph cut-based segmentation on a pig lung volume data of 40 frames gave accurate segmentation results for the top most layer (mucosa) boundary, but not for the bottom boundary. Different parameters were tried to improve segmentation of the bottom boundary. The parameters that were modified for the initial trials for qualitative analysis are shown in Table 4.

Table 4: Parameters changed in the experiment for improving segmentation accuracy

Experiment 6	Parameters			
	BV smoothing 3D		Graph Cut 3D	
	Number of steps	lambda	Slope for Lumen	Slope for Mucosa
A	6	0.001	4	1
B	6	0.001	4	4
C	25	0.005	4	4

Frame 1 and 10 from trial 1 are shown in Figure 21, where the first frame corresponds to frame 201 of 1201 frames that form one OCT volume set.

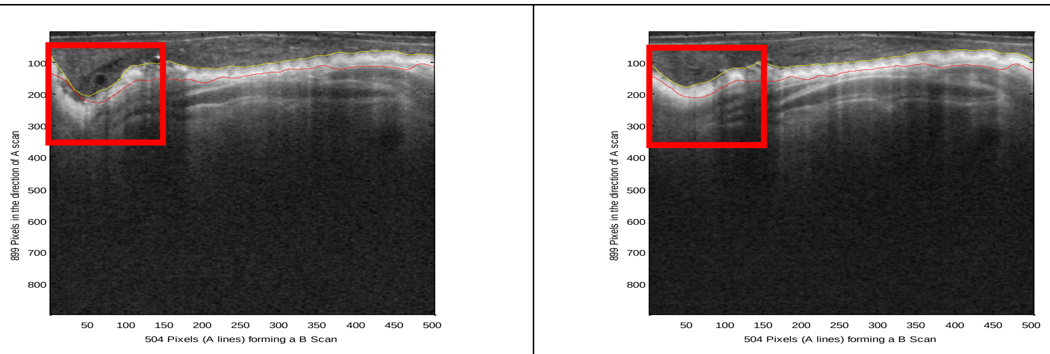

Frame 1

Frame 10

Figure 21: Result of Graph-cut Segmentation after applying 3D smoothing algorithm (BVsmooth

The red regions marked in Figure 21 (above) are shown in Table 5 below for different parameters (trials).

Table 5: Images highlighting the changes in segmentation with different parameters

	EXPERIMENT		
FRAME#	6A	6B	6C
1	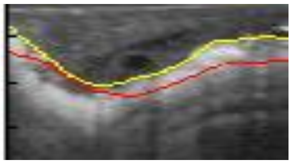	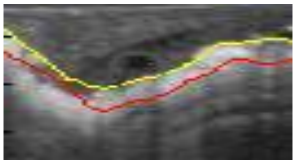	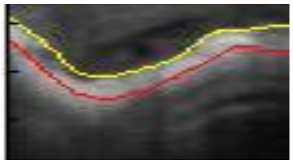
10	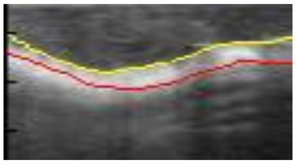	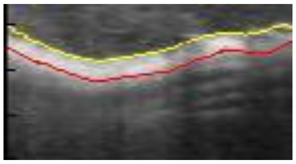	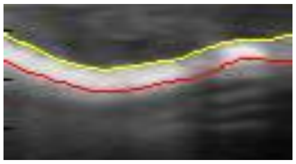

It was qualitatively observed that aggressive BV smoothing gave slightly better results. The segmentation for both the layers, lumen and mucosa, improved with increasing the smoothing of the images. This occurred at a cost of a longer time however.

On changing the allowable variation of edge contour, a trade off was observed. There are two types of frames in the data used in this project- one with an approaching airway branch point characterised by a dip like structure in the layers and other frames which are more consistent with their slopes, i.e. have less variation in their contour. While increasing the allowable variation in the contour of the layer of interest detected the dip like structure better, it also resulted in detection of cartilage as part of the mucosa as can be seen marked by a red circle in the Figure 22.

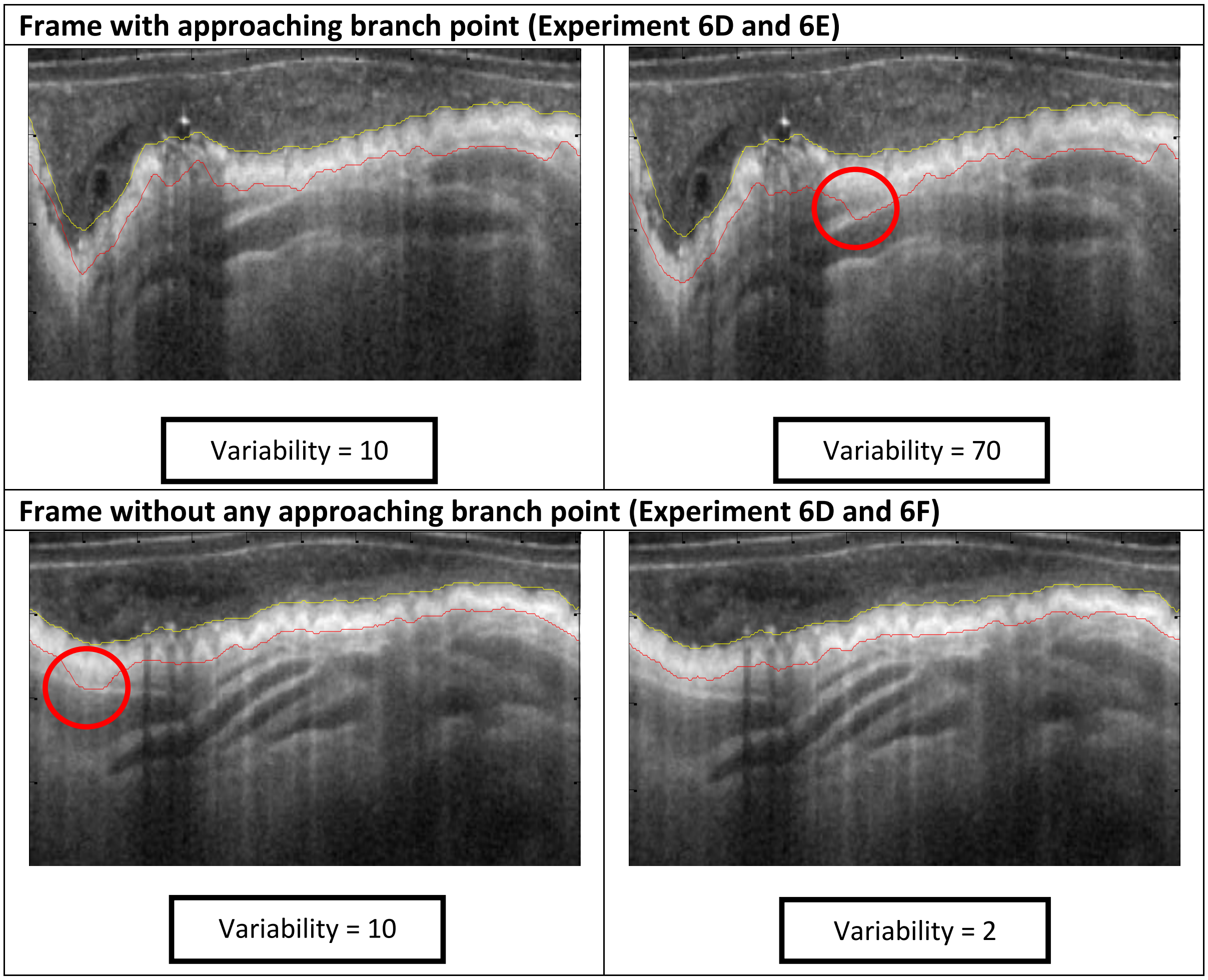

Figure 22: Different variability parameters for Layer contour

Figure 23 shows the intermediate as well as the final results of the sequential segmentation of two layers of interest.

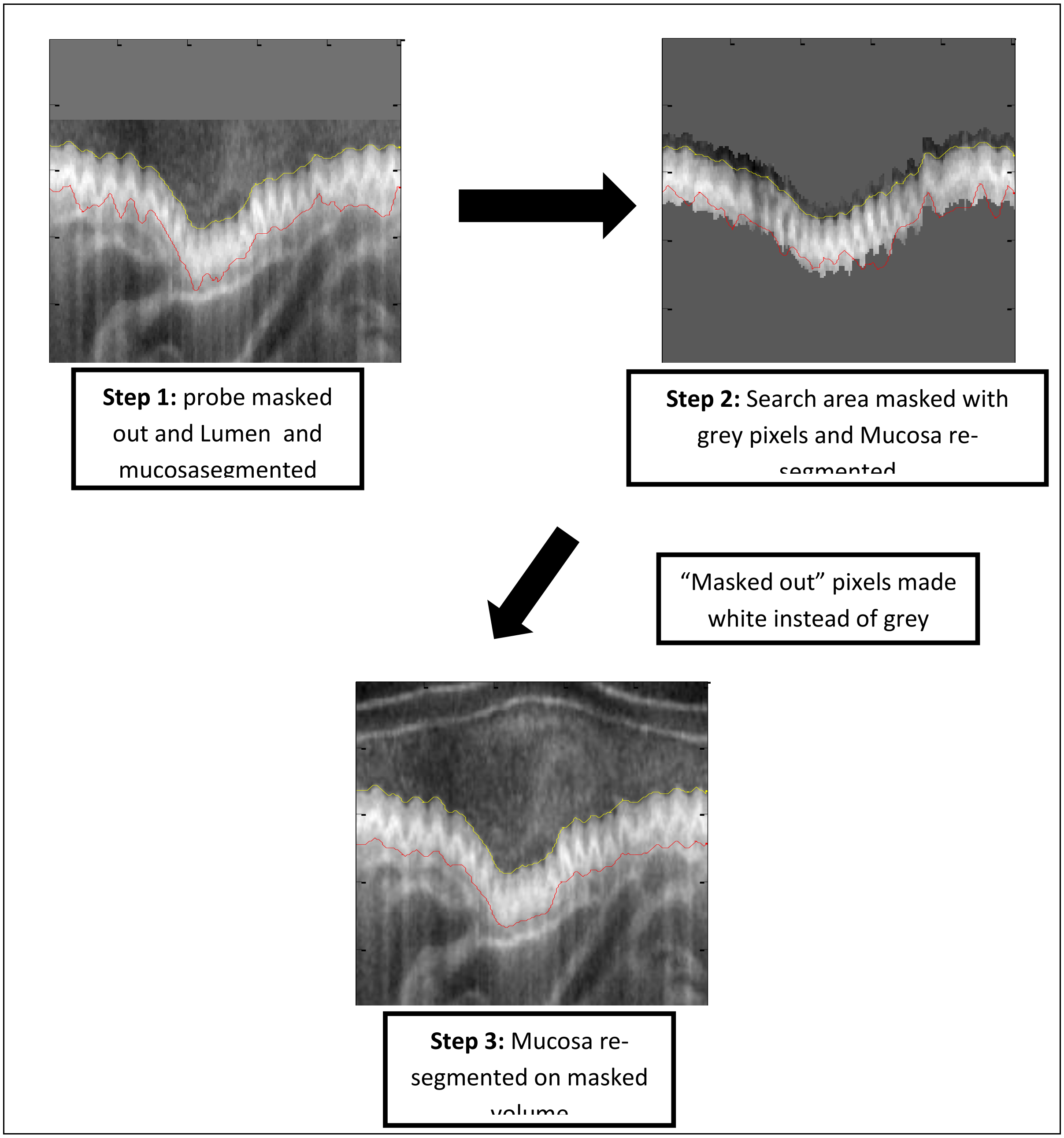

Step 1: probe masked out and Lumen and mucosasegmented

Step 2: Search area masked with grey pixels and Mucosa re-segmented

“Masked out” pixels made white instead of grey

Step 3: Mucosa re-segmented on masked volume

Figure 23: Step wise detection of two layers of interest (experiment 6G)

Sequential approach to segmentation significantly improved the segmentation results for the detection of mucosa. The segmentation results were achieved in 13 minutes for a volumetric set of 300 frames. Removal of the probe as the first step prevented the detection of probe's sheath as part of the layers of interest. Furthermore, removal of pixels relative to the detected lumen boundary reduced the interference of cartilage with the detection of mucosa.

Experiment 7

The aim of this experiment was to achieve 3D segmentation of lumen, mucosa and submucosa. Figure 24 shows the intermediate as well as the final results of segmenting 3 layers of interest- lumen, mucosa and submucosa sequentially.

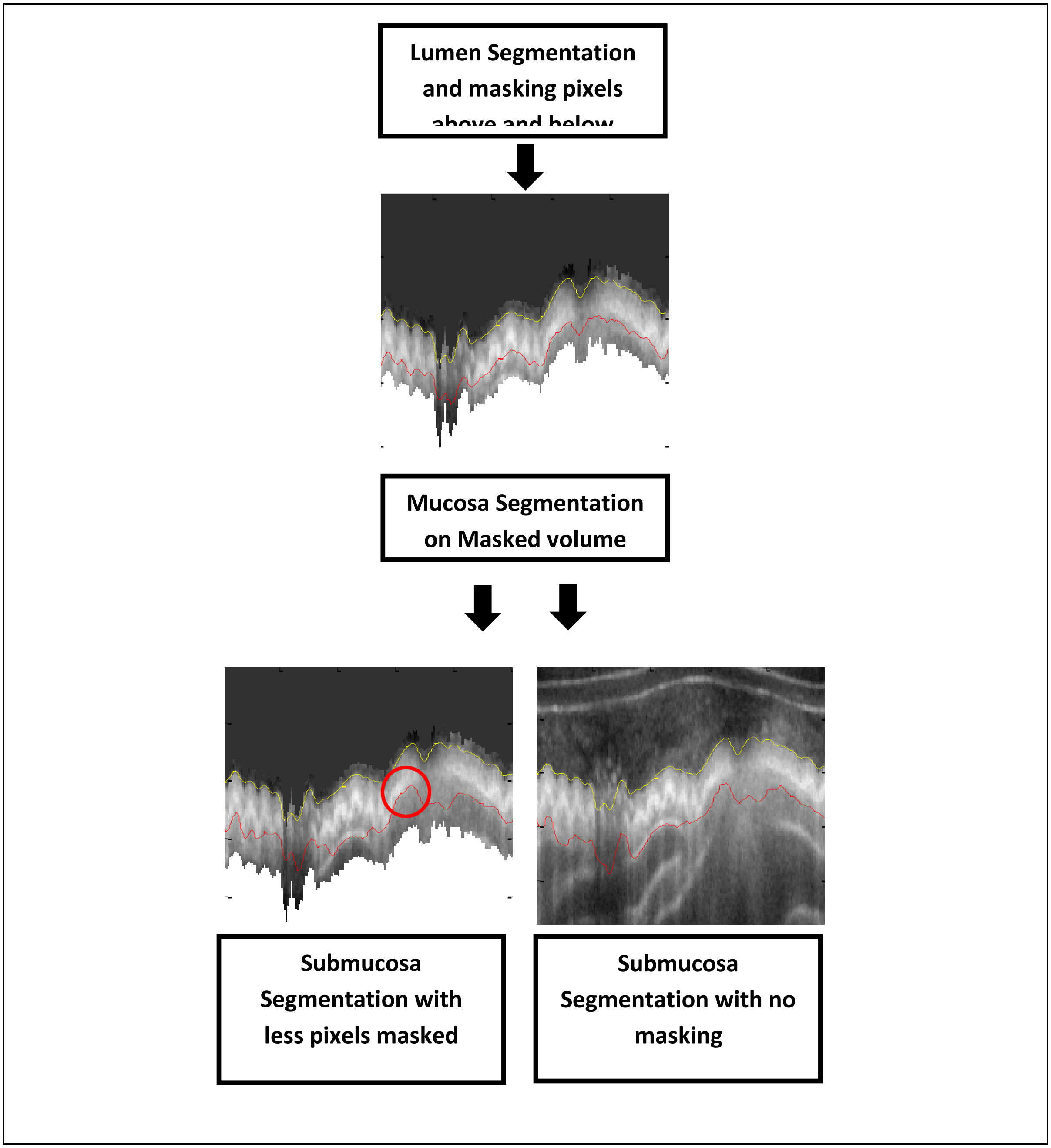

Figure 24: Step wise detection of 3 layers of interest

Extending the sequential approach to the segmentation of the third layer (submucosa) resulted in the interference of the second layer (mucosa) with the detection of the third layer as can be seen in the region marked by the red circle. A non-sequential approach provided better results for the detection of the submucosa. Figure 25 shows an example of the automated segmentation of three layers in comparison to the ground truth segmentation.

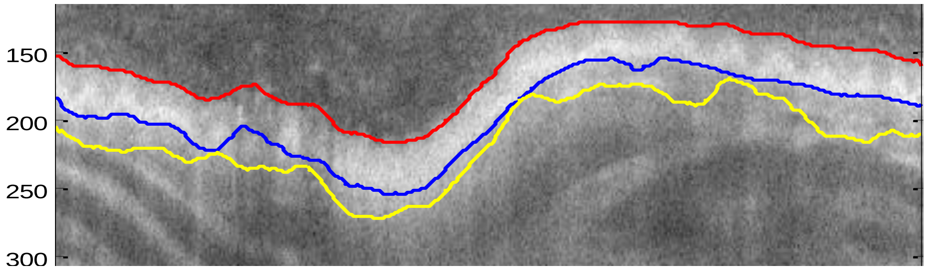

Automated Segmentation

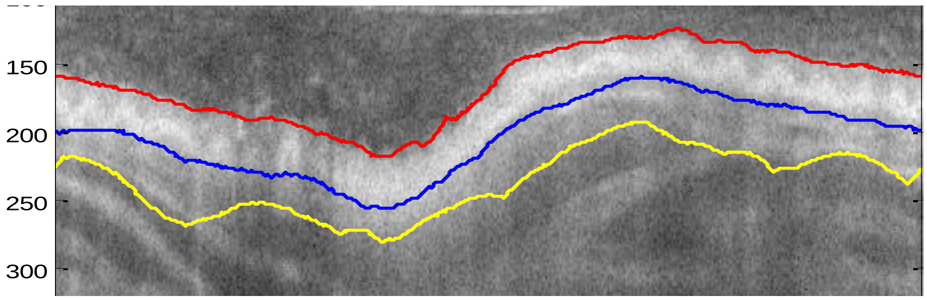

Ground truth

Figure 25: Example Segmentation result shown in comparison to a ground truth set

Experiment 8

The aim of this experiment was to find the best parameter set for the segmentation of lumen, mucosa, and submucosa using quantitative analysis.

Performance measure of the graph cut parameter choosing test cases – RMS

Table 6 shows the RMS errors for each trial. Trials 2 and 3 only concentrated on improving the segmentation of the lumen. Where, ’Lumen Avg Obsv 1’ refers to the average RMS errors between automated segmentation and observer 1 from the 5 porcine airways for lumen, ’Lumen Avg Obsv 2’ refers to the average RMS errors between automated segmentation and observer 2 from the 5 porcine airways for lumen and 'Lumen Avg inter obsv' refers to the average RMS discrepancies between observer1 and observer 2 segmentations from the 5 porcine airways for lumen. Similarly the meanings extend to the table columns for mucosa and submucosa.

Table 6: RMS values for test cases

Trials	Lumen Avg Obsv 1	Lumen Avg Obsv 2	Lumen Avg Inter obsv	Mucosa Avg rms Obsv 1	Mucosa Avg Obsv 2	Mucosa Avg Inter obsv	Submucosa Avg Obsv 1	Submucosa Avg Obsv 2	Submucosa Avg Inter obsv
1	7.40	8.45	6.21	9.49	10	7.01	28.45	25.31	12.68
4	5.76	6.83		9.37	9.75		19.93	20.79	
5	5.36	6.44		9.74	9.78		17.02	19.14	

Due to high RMS errors for the first data set (PIG2) itself, trials 2 and 3 were not carried out for the other 4 data sets. Furthermore, trial 6 took a very long time in achieving segmentation, due to a lower down sampling used, and also resulted in poorly segmented images. Trial 6 was therefore excluded from the RMS performance analysis as the parameter set for this trial was rejected upon qualitative observations of the segmented images.

It can be observed from the amalgamated RMS error values listed in Table 6 that trial 4 provided the least overall RMS errors for the three layers of interest. Although trial 5 parameter set was slightly better for lumen segmentation compared to trial 4 parameter set, it was a very costly procedure due to the application of the 2D despeckling filter on all the 300 frames to be segmented.

Best Results

Airway wall components can either have straight appearance (minimal slope) or have a much higher slope, especially when approaching a branch point.

Detection of 3 Layers in images with minimal slope – branch point not approaching

Figure 26 and Figure 27 show examples of segmented frames with no airway branch point approaching.

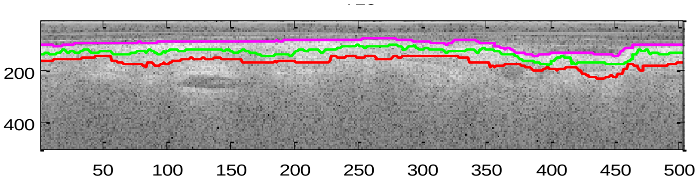

Figure 26: PIG3 – frame 726

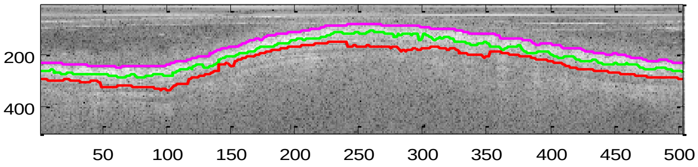

Figure 27: PIG 4-frame433

The best parameter set for automated segmentation of lumen, mucosa and submucosa can be qualitatively said to be successful in detecting the layers accurately when the frames don't have any airway branch points approaching.

Detection of 3 Layers in images with approaching branch point, hence greater slope

Figure 28 shows an example of a segmented frames with airway branch point approaching.

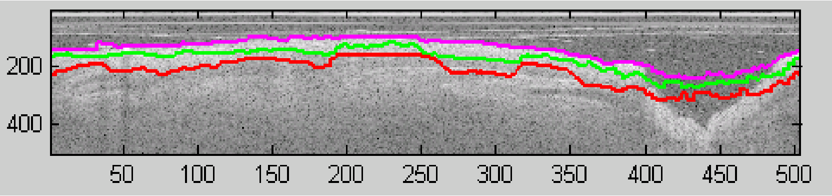

Figure 28: PIG 6-frame492

As can be qualitatively observed from Figure 28, the best parameter set for automated segmentation of lumen, mucosa and submucosa fails to successfully detect the layers accurately when the frames have airway branch points approaching.

3D Visualization of Results

Figure 29 shows an example 3D figure, prior to segmentation, comprising of 300 frames. Cartesian form of the images was used for this purpose in order to better visualise the structure of the porcine airway. The volume presented also consists of a branching point as labelled in Figure 29.

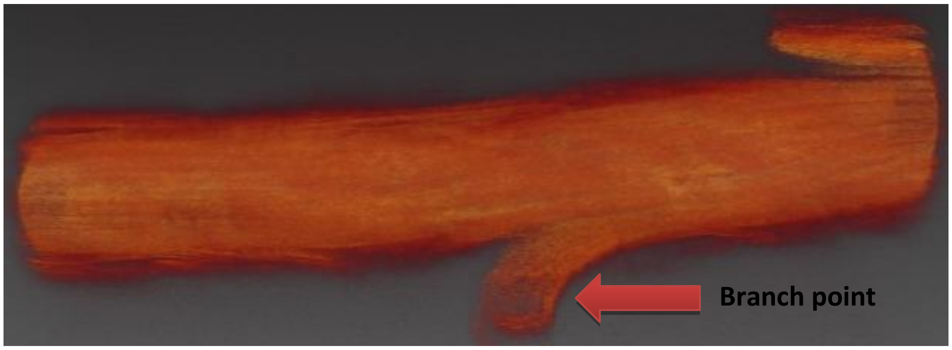

Figure 29: Volume Rendering of 300 Cartesian Frames

Figure 30 shows the polar form of the data rendered along with one of the corresponding 300 frames that form the volume. The volume is positioned to highlight the different layers and hence the branching point is not observed.

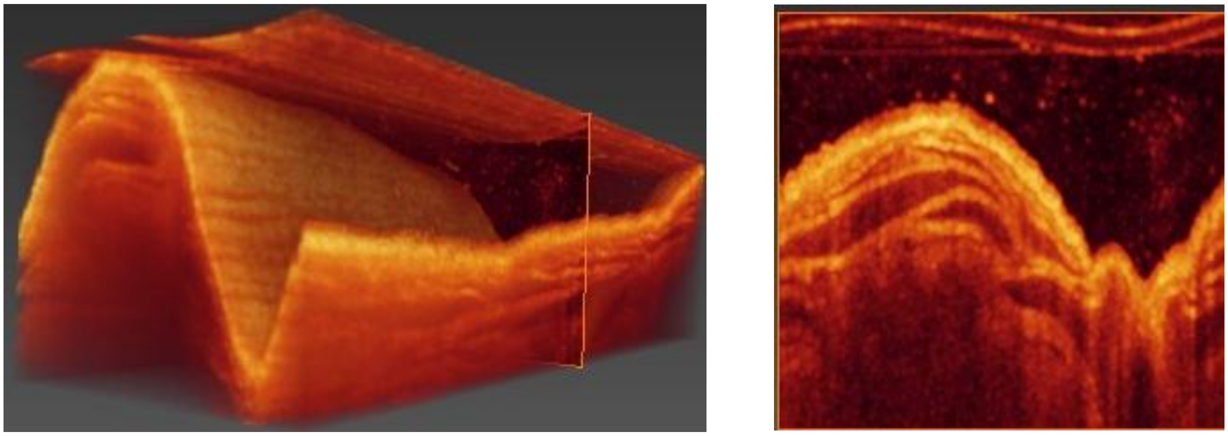

Figure 30: Volume Rendering of Polar form of frames showing one of the corresponding frames

Figure 31 shows rendering of the segmentation results for lumen, mucosa and submucosa along with one of the corresponding 300 frames that form the volume.

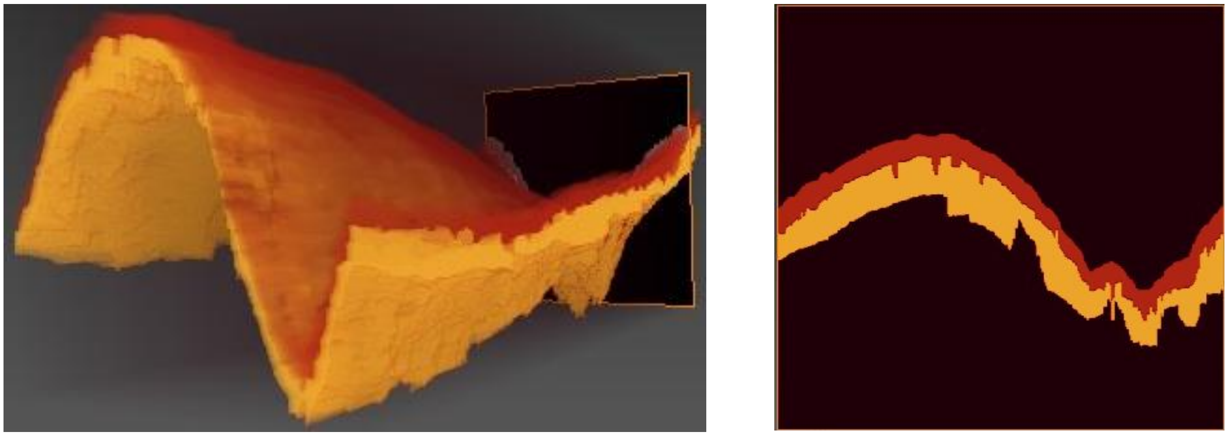

Figure 31: Volume Rendering of Segmented Result in polar form (300 frames) showing a corresponding segmented frame

Branching Points

Figure 31 shows the polar volumes, both before and after segmentation, along with an image frame corresponding to the branch point. The volumes are positioned in order to observe the location of the branch point which appears as holes in the polar form of the volume. The volume from the segmented frames fails to show the branching point due to inaccurate segmentation in this region, as expected.

	Volume	Branch Point-Corresponding Image Frame
Original (polar form)		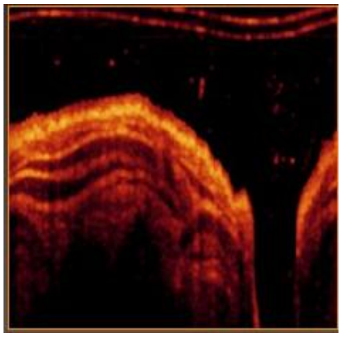
Segmentation Rendered (polar form)		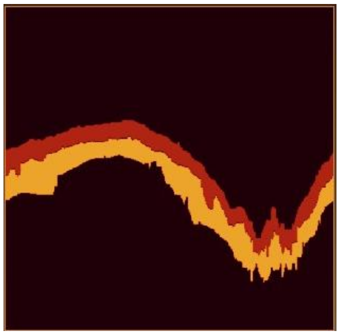

Figure 32: Branch Points in Polar Volume

Validation of Best Segmentation Results

Trial 4a gave the lowest RMS errors among the test cases and therefore was chosen as the best parameter set. Trial 4a was then performed on all the porcine airway data set. The segmentation results were compared and analysed against the two sets of ground truth using RMS errors, Jaccard Similarities and Bland-Altman plots for area measurements.

Root mean square errors

Root mean square errors refer to root mean square differences between the contours for the layers of interest. RMS analysis was done between the following pairs for each layer of interest (lumen, mucosa, and submucosa):

i. Automated segmentation and Observer 1 segmentation- referred to as RMS error
ii. Automated segmentation and Observer 2 segmentation- referred to as RMS error
iii. Observer 1 and Observer 2 segmentations- referred to as inter-observer RMS discrepancy

Figure 33 shows the RMS analysis for Lumen.’ Lumen avg inter’ refers to average inter observer discrepancies. ’Lumen avg Obsv1’ refers to average rms errors between automated segmentation and observer 1 segmentation. Finally, ’Lumen avg Obsv2’ refers to average rms errors between automated segmentation and observer 2 segmentation. All averages were calculated as an average of 6 rms analysis per porcine airway.

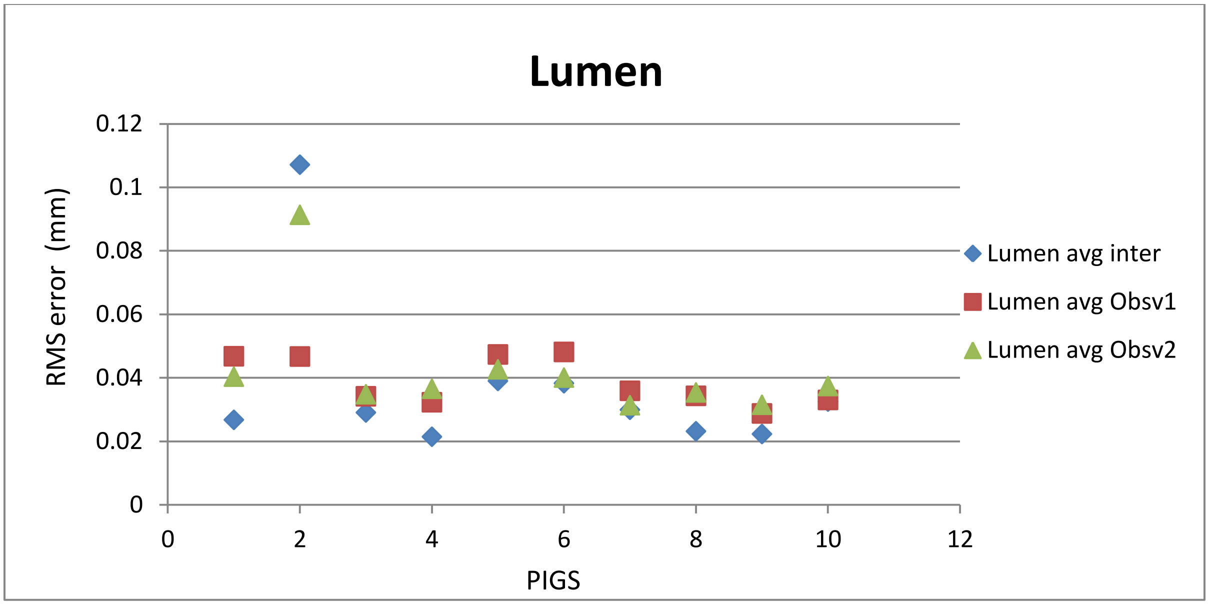

Figure 33: RMS error plot for Lumen Contour

The mean RMS error between observer 1 and automated segmentation was 0.039 mm and the mean RMS error between observer 2 and automated segmentation was 0.042 mm. The mean inter observer RMS discrepancy between the observers 1 and 2 was 0.0037 mm. Therefore RMS error from observer 1 was 5.4% higher than inter observer discrepancy whereas RMS error from observer 2 was 13.5% higher.

Figure 34 shows the RMS analysis for Mucosa.' Mucosa avg inter' refers to average inter observer discrepancies. 'Mucosa avg Obsv1' refers to average rms errors between automated segmentation and observer 1 segmentation. Finally, 'Mucosa avg Obsv2' refers to average rms errors between automated segmentation and observer 2 segmentation. All averages were calculated as an average of 6 rms analysis per porcine airway.

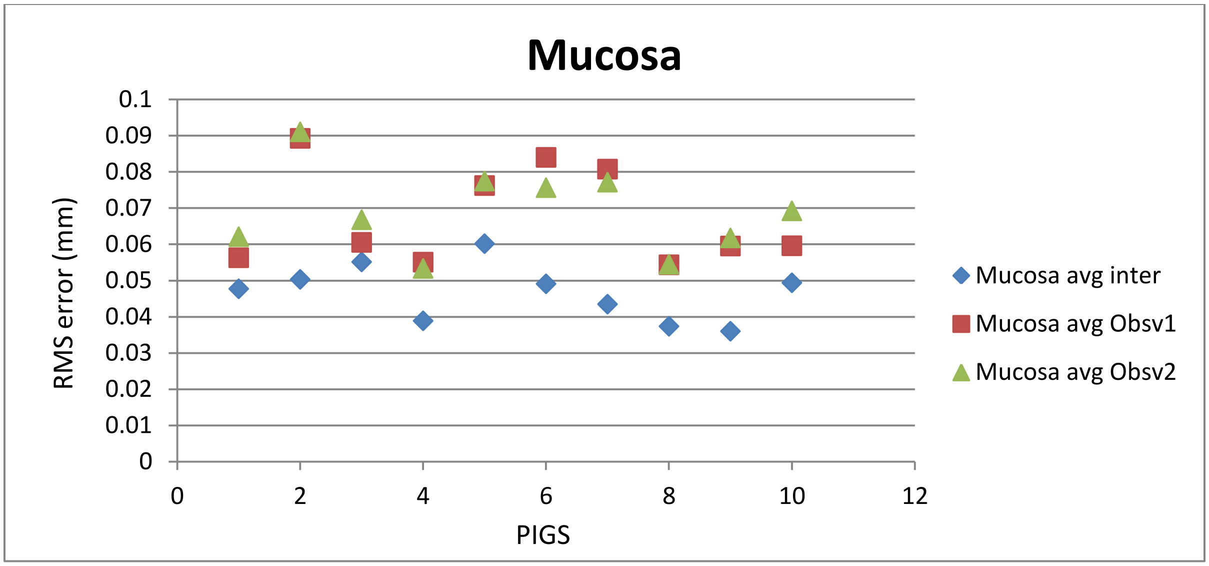

Figure 34: RMS error plot for Mucosa contour

The mean RMS error between observer 1 and automated segmentation was 0.066 mm and the mean RMS error between observer 2 and automated segmentation was 0.069 mm. The mean inter observer RMS discrepancy between the observers 1 and 2 was 0.047 mm. Therefore RMS error from observer 1 was 40% higher than inter observer discrepancy whereas RMS error from observer 2 was 47% higher.

Figure 35 shows the RMS analysis for Submucosa.' Cart avg inter' refers to average inter observer discrepancies. 'Cart avg Obsv1' refers to average rms errors between automated segmentation and observer 1 segmentation. Finally, 'Cart avg Obsv2' refers to average rms errors between automated segmentation and observer 2 segmentation. All averages were calculated as an average of 6 rms analysis per porcine airway.

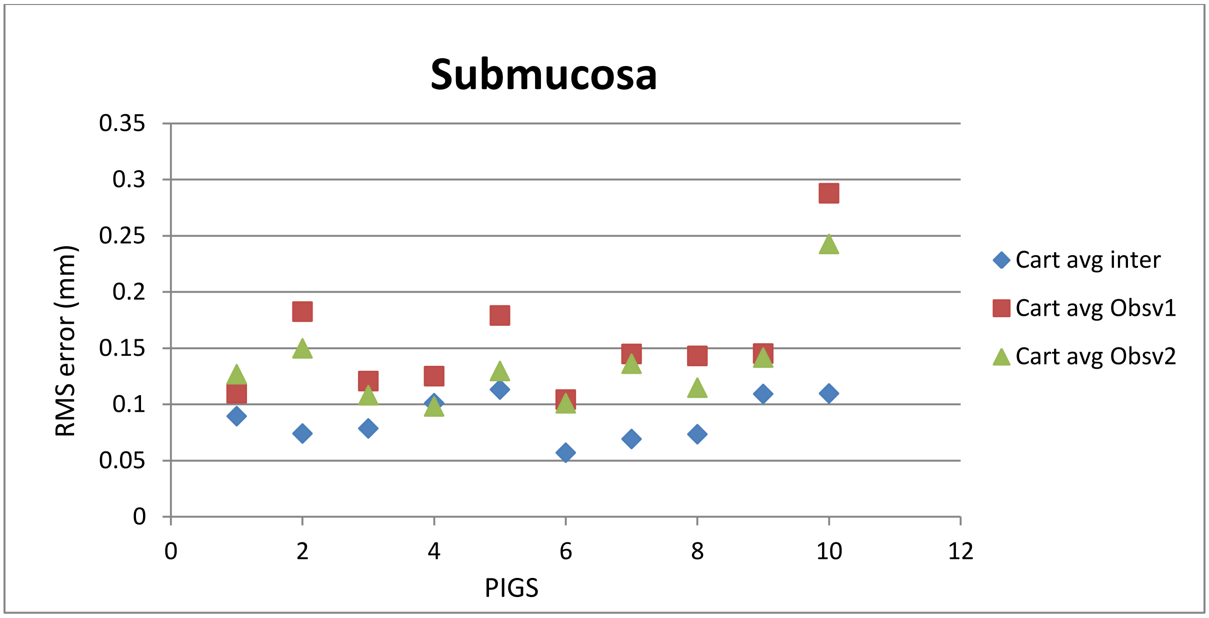

Figure 35: RMS error plot for Submucosa contour

The mean RMS error between observer 1 and automated segmentation was 0.15 mm and the mean RMS error between observer 2 and automated segmentation was 0.13 mm. The mean inter observer RMS discrepancy between the observers 1 and 2 was 0.088 mm. Therefore RMS error from observer 1 was 70% higher than inter observer discrepancy whereas RMS error from observer 2 was 48% higher.

Jaccard Similarity

The segmented contours of the layers of interest were first used to create respective binary images with the white pixels depiction the region enclosed by the contour as shown in Figure 36. These images were also created for respective manually segmented contours. The images were then analysed for similarity using the Jaccard coefficient given by the fraction of similar regions over union:

$$J = \frac{intersection}{union}$$

The similarities were calculated for the same pairs as used in the RMS analysis:

i. Automated and Observer 1 manual segmentations for Lumen, Mucosa and Submucosa
ii. Automated and Observer 2 manual segmentations for Lumen, Mucosa and Submucosa
iii. Observer 1 and Observer 2 manual segmentations for Lumen, Mucosa and Submucosa

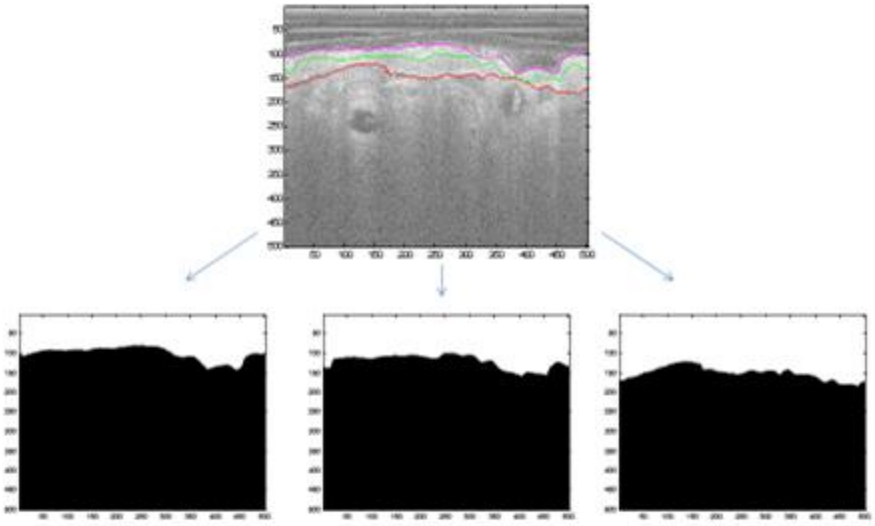

Figure 36: Jacard figures for Lumen, Mucosa and Submucosa

Figure 37 shows the Jaccard similarity indices between the automated segmentation and observer 1 segmentation, automated segmentation and observer 2 segmentation as well as the inter observer Jaccard similarity for lumen.

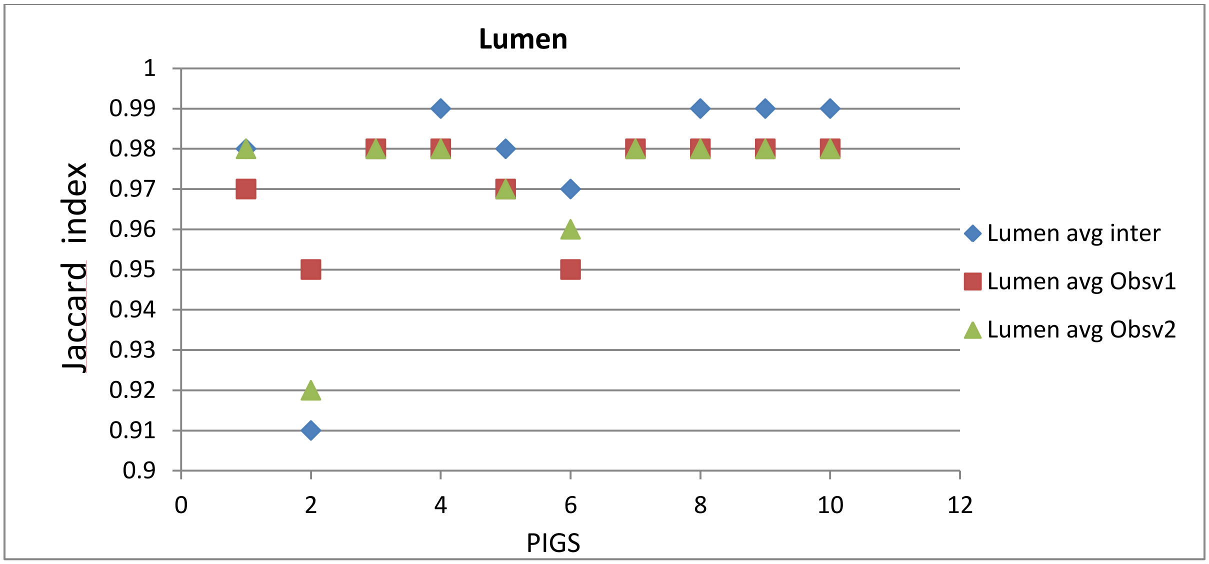

Figure 37: Plot showing Jaccard similarities in percentages for Lumen Segmentation

The mean Jaccard similarity index between observer 1 and automated segmentation was 0.972 with a standard error of 0.004 and the mean Jaccard similarity index between observer 2 and automated segmentation was 0.971 with a standard error of 0.007. The mean inter observer Jaccard similarity index between the observers 1 and 2 was 0.976 with a standard error of 0.008. Therefore Jaccard similarities of automated segmentation with standard errors were the same as the Jaccard similarity between the two observer’s segmentations.

Figure 38 shows the Jaccard similarity indices between the automated segmentation and observer 1 segmentation, automated segmentation and observer 2 segmentation as well as the inter observer Jaccard similarity for mucosa.

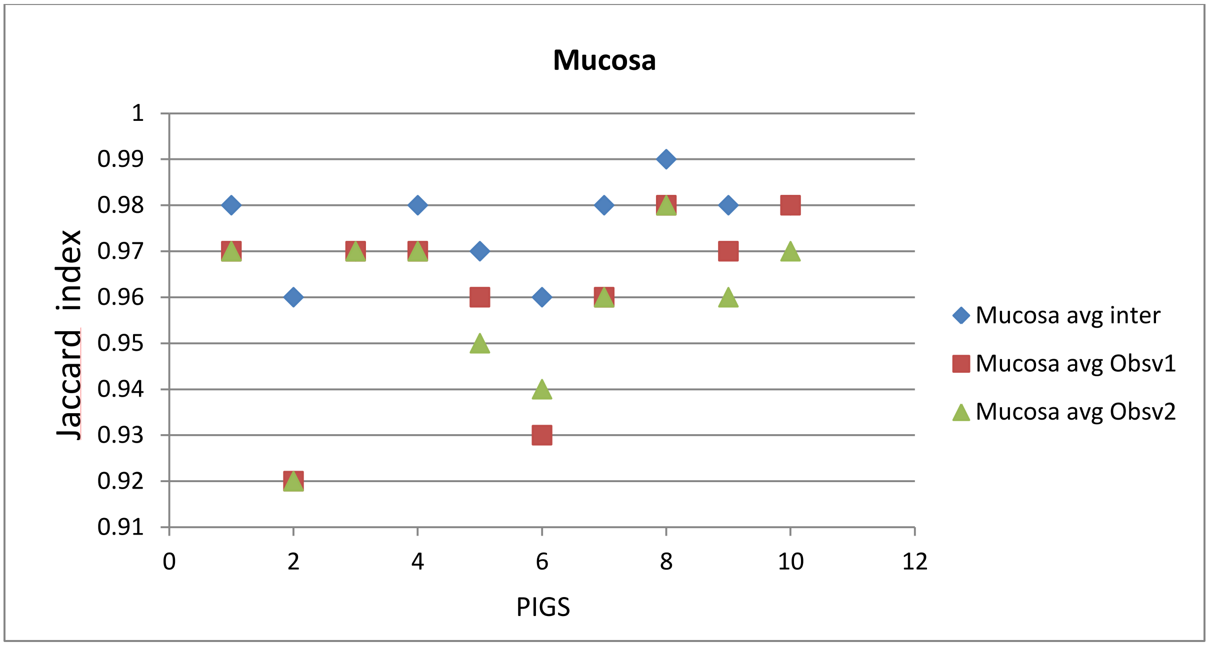

Figure 38: Plot showing Jaccard similarities in percentages for mucosa Segmentation

The mean Jaccard similarity index between observer 1 and automated segmentation was 0.961 with a standard error of 0.007 and the mean Jaccard similarity index between observer 2 and automated segmentation was 0.959 with a standard error of 0.006. The mean inter observer Jaccard similarity index between the observers 1 and 2 was 0.975 with a standard error of 0.003. Therefore Jaccard similarities of automated segmentation with standard errors were comparable to the Jaccard similarity between the two observer's segmentations.

Figure 39 shows the RMS errors between the automated segmentation and observer 1 segmentation, automated segmentation and observer 2 segmentation as well as the inter observer RMS discrepancies for Submucosa.

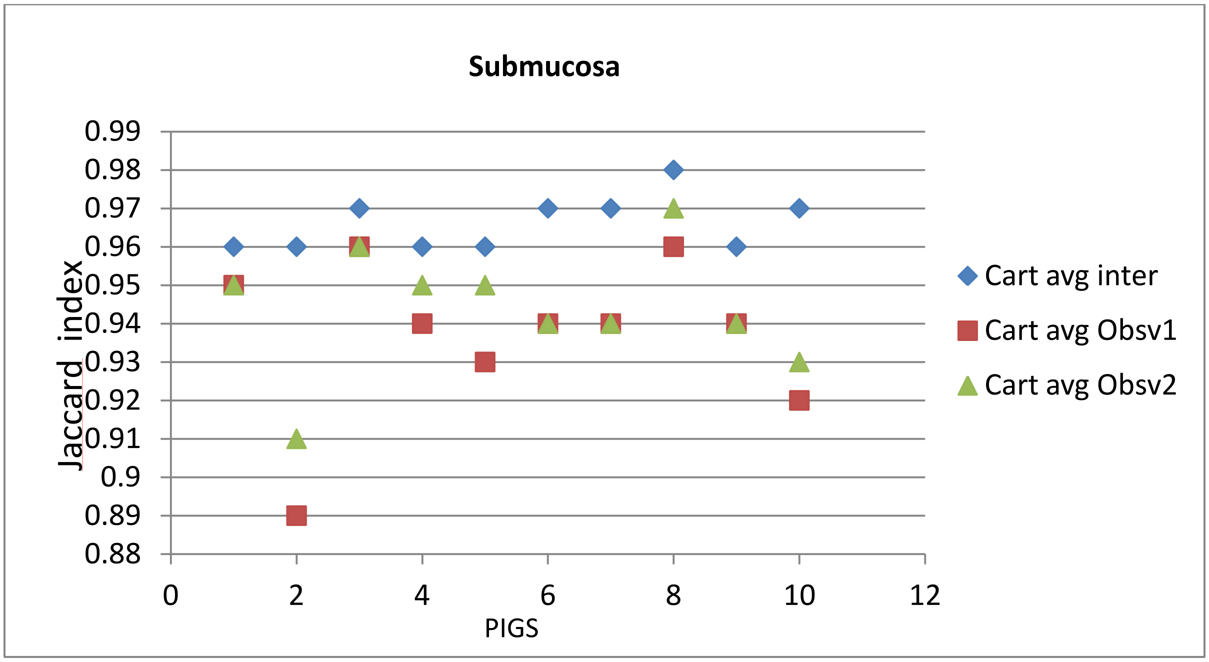

Figure 39: Plot showing Jaccard similarities in percentages for submucosa Segmentation

The mean Jaccard similarity index between observer 1 and automated segmentation was 0.937 with a standard error of 0.007 and the mean Jaccard similarity index between observer 2 and automated segmentation was 0.944 with a standard error of 0.006. The mean inter observer Jaccard similarity index between the observers 1 and 2 was 0.966 with a standard error of 0.002. Therefore Jaccard similarities of automated segmentation with standard errors were within 2% of the Jaccard similarity between the two observer's segmentations with standard error.

Bland-Altman plots for Area

Figure 40 and Figure 41 show Bland-Altman plots for the Lumen areas measured by automated segmentation versus observer 1 and observer 2 respectively.

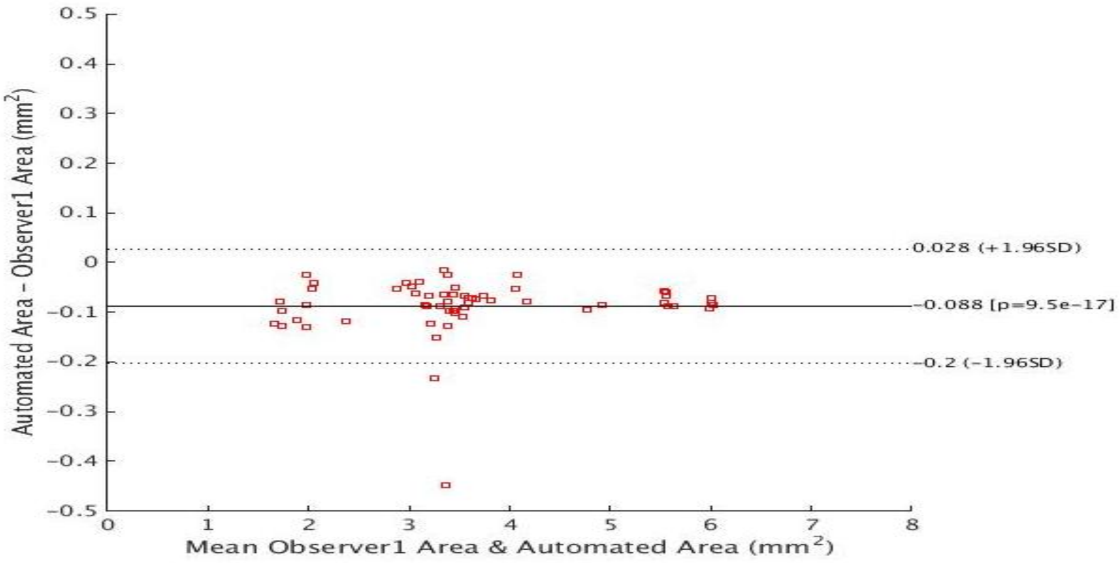

Figure 40: Bland-Altman Area plot for Lumen automated segmentation vs Observer 1 Segmentation

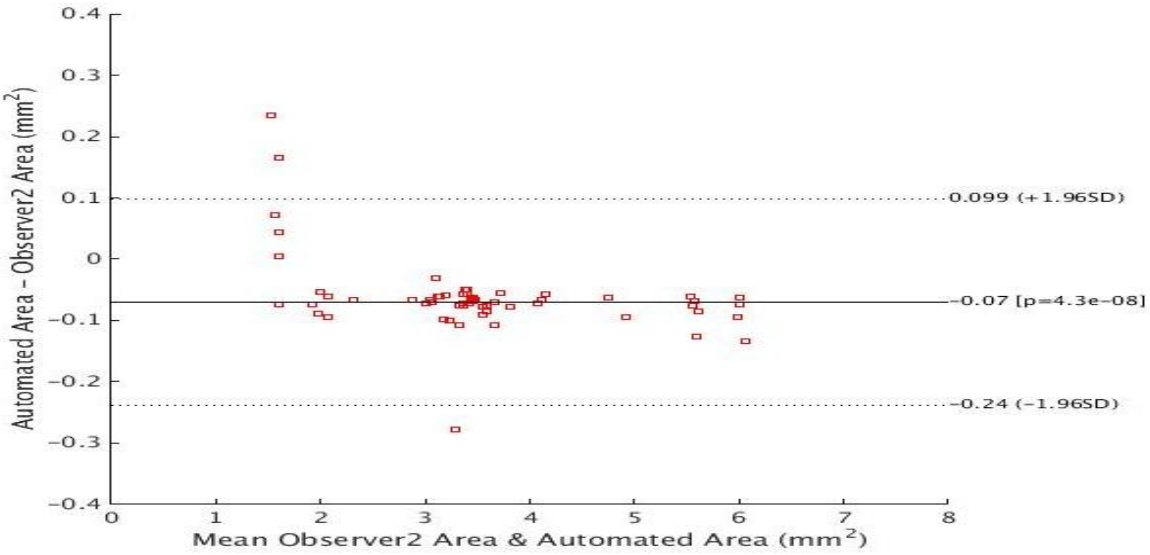

Figure 41: Bland-Altman Area plot for Lumen automated segmentation vs Observer 2 Segmentation

The measurements resulting from the automated segmentations had very little bias compared to observer 1 (2.5%) and observer 2(2%). The correlations between measurements from automated segmentations and observer 1 and observer 2 segmentations were 0.9977 and 0.9976 respectively.

Figure 42 shows the Bland-Altman plot for the Lumen areas measured by observer 1 versus observer 2, the two ground truth measurement sets.

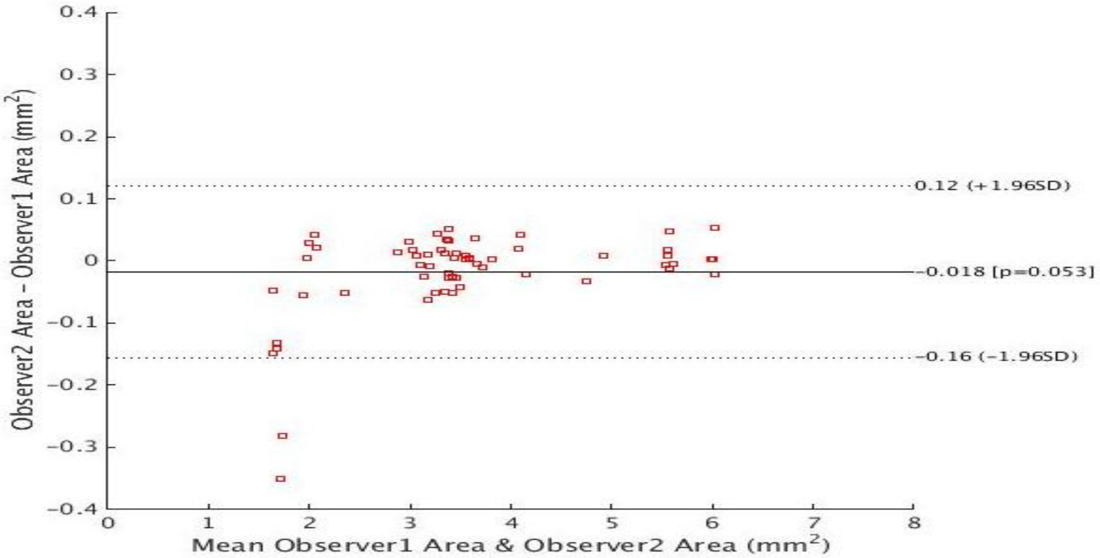

Figure 42: Bland-Altman Area plot for Lumen Observer 1 segmentation vs Observer 2 Segmentation

The correlation between measurements from observer 1 and observer 2 segmentations was 0.9974. The bias between the measurements was 0.5%.

Figure 43 and Figure 44 show Bland-Altman plots for the Mucosa areas measured by automated segmentation versus Observer 1 and observer 2 respectively.

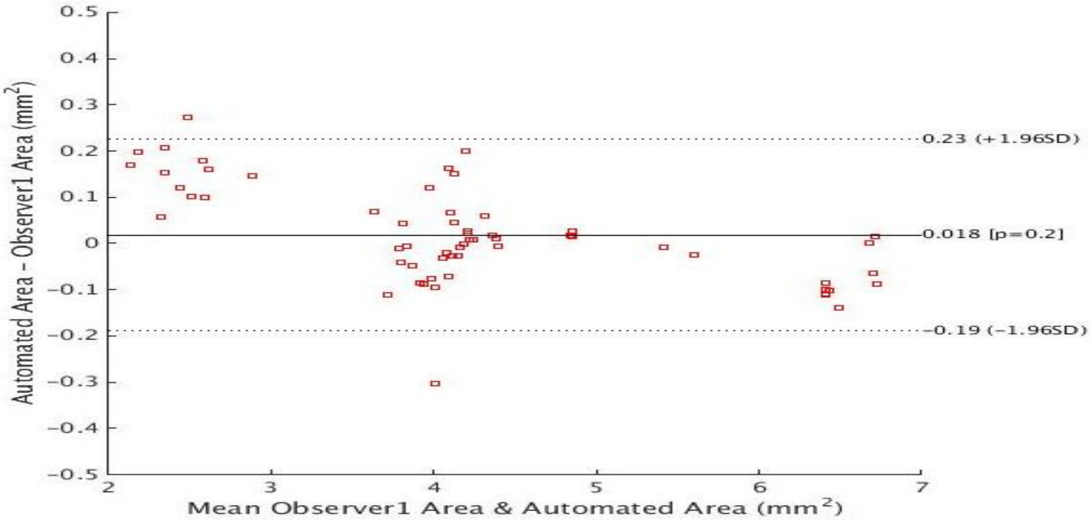

Figure 43: Bland-Altman Area plot for Mucosa automated segmentation vs Observer 1 Segmentation

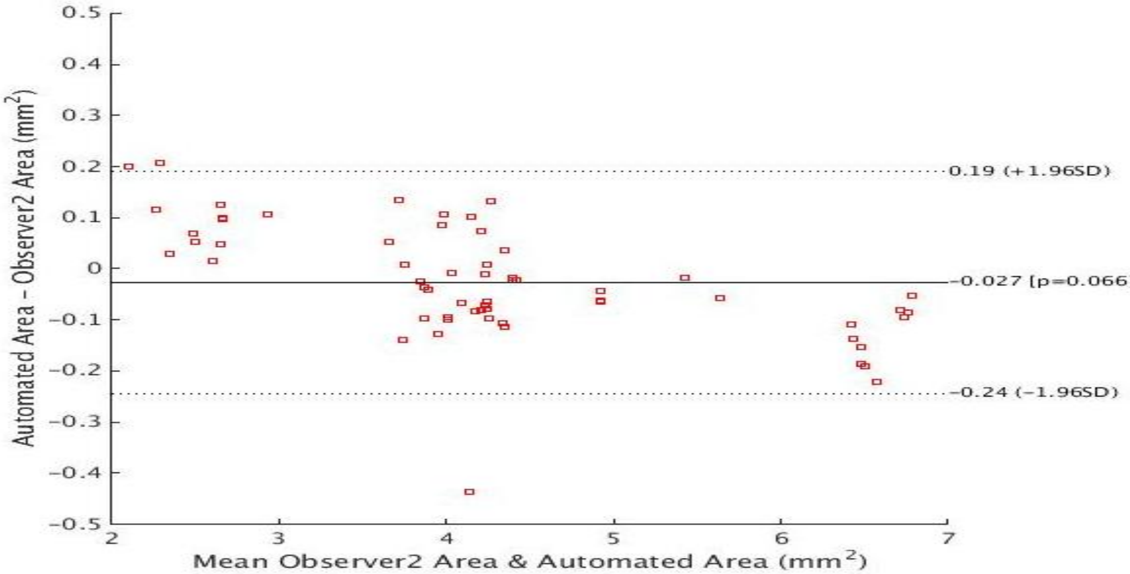

Figure 44: Bland-Altman Area plot for Mucosa automated segmentation vs Observer 2 Segmentation

Once Again, the measurements resulting from the automated segmentations had negligible bias compared to observer 1 (0.4%) and observer 2(0.6%). The correlations between measurements from automated segmentations and observer 1 and observer 2 segmentations were 0.9954 and 0.9949 respectively.

Figure 45 shows the Bland-Altman plot for the Mucosa areas measured by observer 1 versus observer 2, the two ground truth measurement sets.

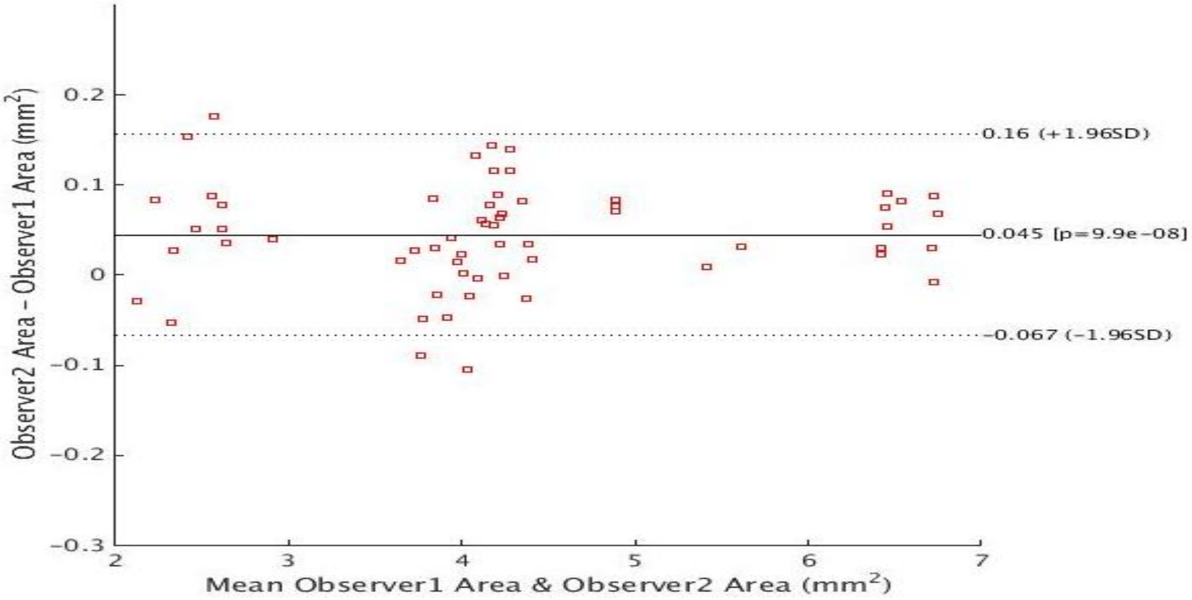

Figure 45: Bland-Altman Area plot for Mucosa observer 1 segmentation vs Observer 2 Segmentation

The correlation between measurements from observer 1 and observer 2 segmentations was 0.9981. The bias between the measurements was 1%.

Figure 46 and Figure 47 show Bland-Altman plots for the Submucosa areas measured by automated segmentation versus Observer 1 and observer 2 respectively.

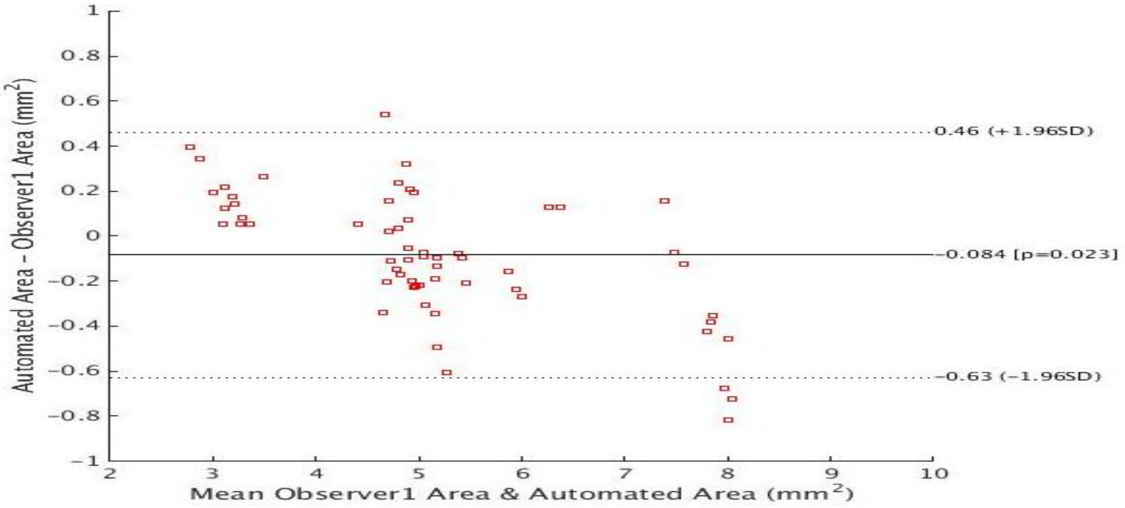

Figure 46:Bland-Altman Area plot for Submucosa automated segmentation vs Observer 1 Segmentation

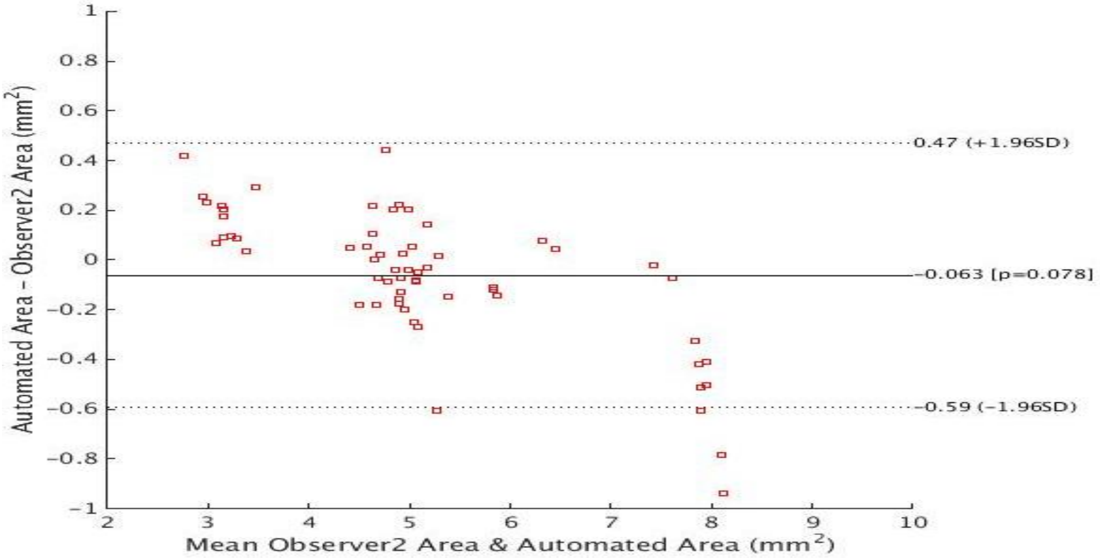

Figure 47: Bland-Altman Area plot for Submucosa automated segmentation vs Observer 2 Segmentation

Finally, the measurements resulting from the automated segmentations of submucosa also had very little bias compared to observer 1 (1.6%) and observer 2(1.2%). The correlations between measurements from automated segmentations and observer 1 and observer 2 segmentations were 0.9734 and 0.9807 respectively.

Figure 48 shows the bland-Altman plot for the Submucosa areas measured by observer 1 versus observer 2, the two ground truth measurement sets.

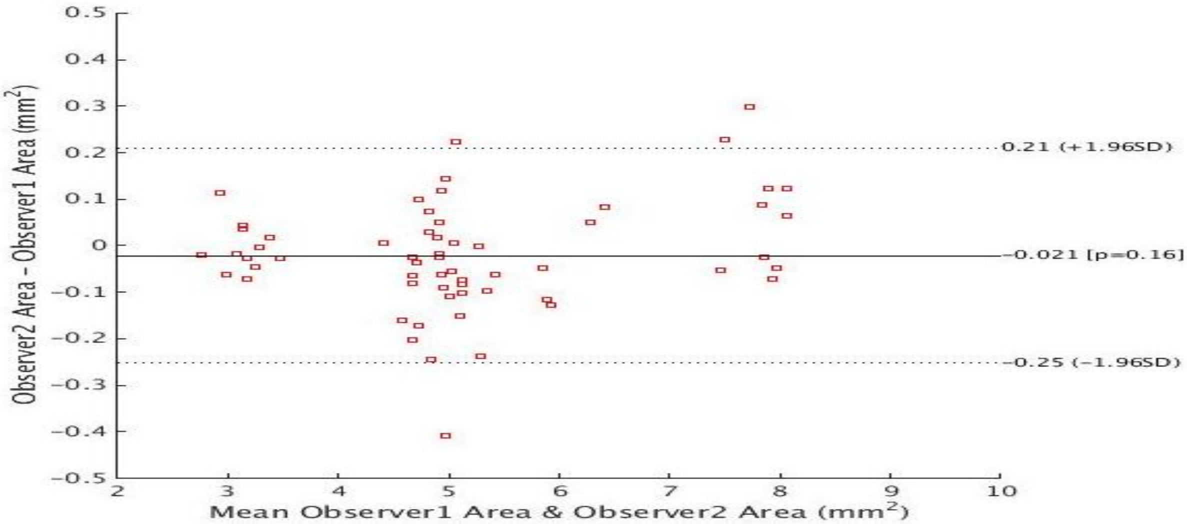

Figure 48: Bland-Altman Area plot for Submucosa observer 2 segmentation vs Observer 1 Segmentation

The correlation between measurements from observer 1 and observer 2 segmentations was 0.994. The bias between the measurements was 0.4%.

Table 7 shows a summary of the bias and correlation data obtained from Bland-Altman analysis for area measurements on automated segmentation data versus ground truth data.

Table 7: Bland Altman data for Area Measurement Comparisons against Ground Truth

Lumen Auto vs Obsv1	**Lumen Auto vs Obsv2**	**Lumen Inter-obsv**	**Mucosa Auto vs Obsv1**	**Mucosa Auto vs Obsv2**	**Mucosa Inter-obsv**	**Submucosa Auto vs Obsv1**	**Submucosa Auto vs Obsv2**	**Submucosa Inter-obsv**
Bias 2.5%	Bias 2%	Bias 0.5%	Bias 0.4%	Bias 0.6%	Bias 1%	Bias 1.6%	Bias 1.2%	Bias 0.4%
Corr 0.9977	Corr 0.9976	Corr 0.9974	Corr 0.9954	Corr 0.9949	Corr 0.9981	Corr 0.9734	Corr 0.9807	Corr 0.994

Bias refers to the discrepancy in the measurements obtained by the two methods under consideration. In the Bland Altman analysis presented here, comparisons were made between segmentation result and observer 1, segmentation result and observer 2, and results from two observers (inter observer discrepancy). The bias values were less than 5% for all measurement comparisons and the correlations between measurements were very close to 1 with a minimum observed correlation value of 0.9734, as can be seen in Table 7. It can also be observed that the bias values of measurements from automatic segmentation versus ground truth, were comparable to the bias values among the two ground truth data sets.

Chapter 8: Summary and Conclusion

In this thesis, 3D automated segmentation based on previously demonstrated graph cut and BV smoothing methods was achieved for the airway wall components in pigs- lumen and mucosal layers. A total of 10 excised pig airways comprised the data set under consideration and 300 frames per pig airway volume were segmented in this project.

The segmentation was compared against two manually segmented data sets comprising the ground truth achieved by two observers. Comparison methods included root mean square analysis and Jaccard similarity for segmentation contours and bland-altman plots for area measurement comparisons. The results were presented against the inter observer discrepancies. The proposed segmentation algorithm gave comparable results to the manually segmented results in a much shorter time window. The discrepancies of automated segmentation results from individual ground truth data sets were comparable to the inter-observer discrepancies which was the necessary condition for the algorithm's success.

Chapter 9: Future Work

A number of preprocessing techniques were explored to work alongside the graph cut-based algorithm for improvement of the segmentation results. Although most of them did not give the desired results in the preliminary approach tried in this project, many preprocessing techniques show great potential for future work in improving the segmentation results.

Segmentation of the outer most layer of the airway wall can be achieved by combining A-line decay compensation, 3D thresholding (hysteresis) and convex hulls. Moreover, the detection of cartilage inner boundary (third layer/bottom most layer reported in the results) and the mucosa (second/middle layer) currently interfere with each other and this can be improved by applying a 3D hessian filter, taking a convex hull and removing the cartilaginous region to segment the (accurate) mucosa and the top boundary of the convex hull will be the (accurate) inner cartilage layer.

Appendices

Appendix A: Gaussian High Pass filter function

```
%% GAUSSIAN HIGH PASS FILTER
%Rashika Raizada, 301133696
%%
function [high] = GaussianHighpass(I, std)
a=im2double(I);
%figure(1)
%imshow(a)
[m n]=size(a);
f_transform=fft2(a);
f_shift=fftshift(f_transform);
p=m/2;
q=n/2;
d0=std;
for i=1:m
for j=1:n
distance=sqrt((i-p)^2+(j-q)^2);
high_filter(i,j)= 1-exp(-(distance)^2/(2*(d0^2)));
end
end
filter_apply=f_shift.*high_filter;
image_orignal=ifftshift(filter_apply);
image_filter_apply=abs(ifft2(image_orignal));
high = image_filter_apply;
%figure(2)
%imshow(image_filter_apply,[])
%imwrite(image_filter_apply,'hight.pgm');
```

Appendix B: Otsu's Thresholding Matlab script

```
 %% Thresholding for segmentation outermost layer of the airway wall
  colormap('gray')
  despec = twodncdf(im_int);  % im_int (without A line compensation)
  %imagesc(despec)
  high=GaussianHighpass(despec,5);
  img_bw = otsu(high);
  %imagesc(img_bw)
  se = strel('disk',50);
  cls = imclose(img_bw,se);
 % imagesc(cls)
  ed = edge(cls,'sobel');
  se = strel('disk',5);
  dil = imdilate(ed,se);
  se = strel('disk',3);
  er = imerode(dil,se);
 % imagesc(er)
  for i =1:504
   for j = 1:899
     if(er(i,j)>0)
       if(j<400)
         despec(i,j)=256;
       end
     end
   end
  end
imagesc(despec')
```

Appendix C: Matlab script for segmentation of 3 layers

```
% Segment and Display
%% Load Volume
% load('\\bluebell\IMAGEBORG\STUDENTS\RRAIZADA\TINCAN\piglung 2 OCT data (light lab)\Post
Formalin\Volumes and workspaces\Shifted and flipped\Volume.mat');
% load('\\bluebell\IMAGEBORG\STUDENTS\RRAIZADA\Corrected TINCAN\PigLung2_B4\Post
Formalin\volume2.mat');

matvol = volume4;
%matvol = despec_enhanced_vol;

%% Crop Volume
frame_strt = 500; %
frame_end = 800; %
matvol = matvol(:,:,frame_strt:frame_end);
matvol_or = volume3(:,:,frame_strt:frame_end); % volume2
  %% BVvolume
BVvol = BVsmooth3D(matvol,1,0.001,15); % BVsmooth3D(matvol,1,0.001,6);
BVvol(end,:,:) = BVvol(end-1,:,:);
BVvol(1,:,:) = BVvol(2,:,:);
% scaling
if max(BVvol(:))<2
    BVvol = -32768+ (2*32768)/(max(BVvol(:))-min(BVvol(:)))*(BVvol-min(BVvol(:)));
end
BVvol = double(BVvol);

gcBM = []; % output
%% Remove probe
% no 5 frame average
maxBV = max(BVvol(:));
BVvol(1:66,:,:) = maxBV; %-2854; % gray-ish color %BVvol(1:60,:,:) before shift and flip of volume set

%% 3 Layer Segmentation: LumenMucosa and Cartilage inner layer (Submucosa)

%% Top most layer [Lumen]
slope = 4; noop=@(M) M; negate = @(M) -M;
surflines = [4,1]; numSurf = size(surflines,1); % surflines = [4,1] when four lines of instructions


instructions = {{[]},        [0],        8, 4,     zeros(0,2),     1, noop; ... % 1, noop;... % ILM


{[1,1]},       [0],        4, 2,      zeros(0,2),     1, noop; ... % 4, noop;...


{[2,1]},       [0],        2, 1,      zeros(0,2),     1, noop; ... % 4, noop;...
```

```
{[3,1]},        [0],            1, 1,       zeros(0,2),     1, noop; ... % 4, noop;... % IO based on ILM

};



% instructions = {{[]},           [0],            4, 4,       zeros(0,2),     1, noop;...   % 1, noop;... % ILM

%               {[1,1]},        [0],            2, 2,       zeros(0,2),     1, noop;...   % 4, noop;...

%               {[2,1]},        [0],            1, 1,       zeros(0,2),     1, noop;...   % 4, noop;...

%               };

gc = graphCut3D_prior(BVvol, numSurf, slope, instructions, surflines,0); % mavol5_new
gcBM = squeeze(gc{1});

%% Bottom most layer [Submucosa]
slope = 4; noop=@(M) M; negate = @(M) -M; %% slope =4: best so far, slope = 1: default;
prior{1} = reshape(gcBM,[1 size(gcBM,1) size(gcBM,2)]);
%surflines = [4,1]
surflines = [4,1]; numSurf = size(surflines,1);
%

% instructions = {{[100,1]},      [-50],          4, 2,       zeros(0,2),     5, noop;...   % 1, noop;... % ILM

%               {[1,1]},        [0],            2, 1,       zeros(0,2),     2, noop;...   % 4, noop;...

%               {[2,1]},        [0],            1, 1,       zeros(0,2),     2, noop;...   % 4, noop;...

%               };

instructions = {{[100,1]},      [-70],          8, 4,       zeros(0,2),     20, negate; ... %10, negate;... % {{[100,1]}
% [-30] for lamina, [-50] for submucosa


{[1,1]},        [0],            4, 2,       zeros(0,2),     2, negate; ... %10, negate;...


{[2,1]},        [0],            2, 1,       zeros(0,2),     2, negate; ... %2, negate;...


{[3,1]},        [0],            1, 1,       zeros(0,2),     2, negate; ... %2, negate;...

};
gc = graphCut3D_prior(BVvol, numSurf, slope, instructions, surflines,prior); %BVvol
gcBM3 = squeeze(gc{1});

%Wipe off Pixels below outer most layer (gcBM3)
maxBV = max(BVvol(:));
```

```
for myi=1:size(BVvol,3)
    for i = 1: size(BVvol,1) % 431 points (depth)

for j = 1: size(BVvol,2) % 504 points

if ( i > gcBM3(j, myi))

BVvol(i,j,myi) =maxBV;

end

end
    end
end

%% Detect Mucosa

slope = 4; noop=@(M) M; negate = @(M) -M; %% slope =4: best so far, slope = 1: default;
prior{1} = reshape(gcBM,[1 size(gcBM,1) size(gcBM,2)]);
surflines = [4,1]; numSurf = size(surflines,1);

% instructions = {{[100,1]},       [-30],          4, 2,       zeros(0,2),     5, noop;...   % 1, noop;... % ILM

%              {[1,1]},          [0],            2, 1,       zeros(0,2),     2, noop;...   % 4, noop;...

%              {[2,1]},          [0],            1, 1,       zeros(0,2),     2, noop;...   % 4, noop;...

%             };
%

instructions = {{[100,1]},       [-30],          8, 4,       zeros(0,2),     10, negate; ... %10, negate;... % {{[100,1]}
% [-30], 5 negate for lamina, [-50], 5 noop for submucosa


{[1,1]},          [0],            4, 2,       zeros(0,2),     2, negate; ... %10, negate;...



{[2,1]},          [0],            2, 1,       zeros(0,2),     2, negate; ... %2, negate;...



{[3,1]},          [0],            1, 1,       zeros(0,2),     2, negate; ... %2, negate;...

};
gc = graphCut3D_prior(BVvol, numSurf, slope, instructions, surflines,prior); % mavol5_new
gcBM2 = squeeze(gc{1});

%% Display
  for myi= 1:size(BVvol,3)
    %figure
```

```
    clf;
    myi
    subplot(1,2,1);imagesc(matvol_or(:,:,myi), [0 255]); colormap gray
    subplot(1,2,2);
    imagesc(matvol_or(:,:,myi)); colormap gray    % was above this line in subplot %imagesc(BVvol
    xlabel( '504 Pixels (A lines) forming a B Scan' );
    ylabel( '899 Pixels in the direction of A scan' );
    title(myi);
    hold on ;
%     plot(1:size(gcBM,1),smooth(gcBM(:,myi),0.03),'r','LineWidth',2)
%    plot(1:size(gcBM2,1),smooth(gcBM2(:,myi),0.03),'b','LineWidth',2)
%     plot(1:size(gcBM3,1),smooth(gcBM3(:,myi),0.03),'-y','LineWidth',2)
%     plot(1:size(gcBM,1),smooth(gcBM(:,myi),0.05),'r','LineWidth',2)
%    plot(1:size(gcBM2,1),smooth(gcBM2(:,myi),0.05),'b','LineWidth',2)
%     plot(1:size(gcBM3,1),smooth(gcBM3(:,myi),0.05),'-y','LineWidth',2)
    plot(1:size(gcBM,1),gcBM(:,myi), 'r' , 'LineWidth' ,2)
    plot(1:size(gcBM2,1),gcBM2(:,myi), 'b' , 'LineWidth' ,2)
    plot(1:size(gcBM3,1),gcBM3(:,myi), '-y' , 'LineWidth' ,2)


     pause;
  end
```

Appendix D: Matlab script for converting ground truth segmentation to a one to one mapping

```
%% Get Average Y Value for each x value in Ground Truth
  % http://stackoverflow.com/questions/15479533/get-average-y-value-per-x-po

function [xs, ys, frequencies] = One2One(x,y)
xs = unique(x);
[frequencies, xb] = histc(x, xs);
ysp = sparse(1:numel(x), xb, y);
ys = full(sum(ysp)./sum(ysp>0));
```

Appendix E: Matlab script for RMS errors

```
%% Load Frame
%% CORRECTED PIG 2

%AUTOMATED
%5 frame average
%load('\\bluebell\IMAGEBORG\STUDENTS\RRAIZADA\Corrected TINCAN\PigLung2_B4\Post Formalin\AutomaticSegmentation\Trial1_5Avg_205_to_315\matlab.mat');

%MANUAL FRAMES
% start_frame = 205;
%Frame220
% load('\\bluebell\IMAGEBORG\STUDENTS\RRAIZADA\Corrected TINCAN\PigLung2_B4\Post Formalin\Frame 220\segmentation.mat');
  % indx = 11; %frames 210:310, 210+10 = 220, therefore index = 1+10 = 11
  % indx = 21; %when 200:500 frames used
% indx = 16; % when 205:315 frames used
%Frame277
% load('\\bluebell\IMAGEBORG\STUDENTS\RRAIZADA\Corrected TINCAN\PigLung2_B4\Post Formalin\Frame 277\segmentation.mat');

%    indx = 73; % when 205:315 frames used
%Frame283
% load('\\bluebell\IMAGEBORG\STUDENTS\RRAIZADA\Corrected TINCAN\PigLung2_B4\Post Formalin\Frame 283\segmentation.mat');

%    indx = 79; % when 205:315 frames used

%Frame286
% load('\\bluebell\IMAGEBORG\STUDENTS\RRAIZADA\Corrected TINCAN\PigLung2_B4\Post Formalin\Frame 286\segmentation.mat');

%    indx = 82; % when 205:315 frames used

%Frame290
% load('\\bluebell\IMAGEBORG\STUDENTS\RRAIZADA\Corrected TINCAN\PigLung2_B4\Post Formalin\Frame 290\segmentation.mat');

%    indx = 86; % when 205:315 frames used
```

```
%Frame 303
% load('\\bluebell\IMAGEBORG\STUDENTS\RRAIZADA\Corrected TINCAN\PigLung2_B4\Post
Formalin\Frame 303\segmentation.mat');

%    indx = 99; % when 205:315 frames used
%

%% PIG3 3
%AUTOMATED
%load('\\bluebell\IMAGEBORG\STUDENTS\RRAIZADA\Corrected TINCAN\PigLung3_B\Post
Formalin\AutomaticSegmentation\Trial1_5Avg_500_800\matlab.mat');
% start_frame = 500;
%MANUAL
% Frame 530
% load('\\bluebell\IMAGEBORG\STUDENTS\RRAIZADA\Corrected TINCAN\PigLung3_B\Post Formalin\Frame
530\segmentation.mat');
% indx = 31;
%
%Frame 678
% load('\\bluebell\IMAGEBORG\STUDENTS\RRAIZADA\Corrected TINCAN\PigLung3_B\Post Formalin\Frame
678\segmentation.mat');
% indx = 179;

%Frame 702
% load('\\bluebell\IMAGEBORG\STUDENTS\RRAIZADA\Corrected TINCAN\PigLung3_B\Post Formalin\Frame
702\segmentation.mat');
% indx = 203;

%Frame 726
% load('\\bluebell\IMAGEBORG\STUDENTS\RRAIZADA\Corrected TINCAN\PigLung3_B\Post Formalin\Frame
726\segmentation.mat');
% indx = 227;

%Frame 774
% load('\\bluebell\IMAGEBORG\STUDENTS\RRAIZADA\Corrected TINCAN\PigLung3_B\Post Formalin\Frame
774\segmentation.mat');
% indx = 275;

%Frame 785
% load('\\bluebell\IMAGEBORG\STUDENTS\RRAIZADA\Corrected TINCAN\PigLung3_B\Post Formalin\Frame
785\segmentation.mat');
% indx = 286;
%% CORRECTED PIG 4

%AUTOMATED
%5 frame average
%load('\\bluebell\IMAGEBORG\STUDENTS\RRAIZADA\Corrected TINCAN\PigLung4_A2\Post
Formalin\AutomaticSegmentation\Trial1_5frameAvg_400_500\matlab.mat');

%MANUAL FRAMES
% start_frame = 400;
% start_frame = 610;
%Frame 433
```

```
% load('\\bluebell\IMAGEBORG\STUDENTS\RRAIZADA\Corrected TINCAN\PigLung4_A2\Post Formalin\Frame 433\segmentation.mat');

%    indx = 34; % when 400:500 frames used
%Frame 449
% load('\\bluebell\IMAGEBORG\STUDENTS\RRAIZADA\Corrected TINCAN\PigLung4_A2\Post Formalin\Frame 449\segmentation.mat');

%    indx = 50; % when 400:500 frames used
%
%Frame 457
% load('\\bluebell\IMAGEBORG\STUDENTS\RRAIZADA\Corrected TINCAN\PigLung4_A2\Post Formalin\Frame 457\segmentation.mat');

%    indx = 58; % when 400:500 frames used


%Frame 661
% load('\\bluebell\IMAGEBORG\STUDENTS\RRAIZADA\Corrected TINCAN\PigLung4_A2\Post Formalin\Frame 661\segmentation.mat');

%    indx = 52; % when 610:710 frames used

%      indx = 262; %400:700 frames used
%Frame 670
% load('\\bluebell\IMAGEBORG\STUDENTS\RRAIZADA\Corrected TINCAN\PigLung4_A2\Post Formalin\Frame 670\segmentation.mat');

%    indx = 61; % when 610:710 frames used
% indx = 271; %400:700 frames used
%Frame 680
% load('\\bluebell\IMAGEBORG\STUDENTS\RRAIZADA\Corrected TINCAN\PigLung4_A2\Post Formalin\Frame 680\segmentation.mat');

%    indx = 71; % when 610:710 frames used
% indx = 281; %400:700 frames used


%% PIG 5


%AUTOMATED
%load('\\bluebell\IMAGEBORG\STUDENTS\RRAIZADA\Corrected TINCAN\PigLung5_A1\Post Formalin\AutomaticSegmentation\Trial1_5Avg_800_1100\matlab.mat');


%MANUAL
% start_frame = 800;
%Frame 842
% load('\\bluebell\IMAGEBORG\STUDENTS\RRAIZADA\Corrected TINCAN\PigLung5_A1\Post Formalin\Frame 842\segmentation.mat');

%     indx = 43; % when 800:1100 frames used
%Frame 860
% load('\\bluebell\IMAGEBORG\STUDENTS\RRAIZADA\Corrected TINCAN\PigLung5_A1\Post Formalin\Frame 860\segmentation.mat');

%     indx = 61; % when 800:1100 frames used
%Frame 887
```

```
% load('\\bluebell\IMAGEBORG\STUDENTS\RRAIZADA\Corrected TINCAN\PigLung5_A1\Post
Formalin\Frame 887\segmentation.mat');

%     indx = 88; % when 800:1100 frames used
%Frame 922
% load('\\bluebell\IMAGEBORG\STUDENTS\RRAIZADA\Corrected TINCAN\PigLung5_A1\Post
Formalin\Frame 922\segmentation.mat');

%     indx = 123; % when 800:1100 frames used
%Frame 948
% load('\\bluebell\IMAGEBORG\STUDENTS\RRAIZADA\Corrected TINCAN\PigLung5_A1\Post
Formalin\Frame 948\segmentation.mat');

%     indx = 149; % when 800:1100 frames used
%Frame 1010
% load('\\bluebell\IMAGEBORG\STUDENTS\RRAIZADA\Corrected TINCAN\PigLung5_A1\Post
Formalin\Frame 1010\segmentation.mat');

%     indx = 211; % when 800:1100 frames used
%% PIG 6

%AUTOMATED
%load('\\bluebell\IMAGEBORG\STUDENTS\RRAIZADA\Corrected TINCAN\PigLung6_B2\Post
Formalin\AutomaticSgmentation\Trial1_5Avg_400_700\matlab.mat');

%MANUAL
% start_frame = 400;
%Frame 465

%    load('\\bluebell\IMAGEBORG\STUDENTS\RRAIZADA\Corrected TINCAN\PigLung6_B2\Post
Formalin\Frame 465\segmentation.mat');

%      indx = 66; % when 400:700 frames used
%Frame 492

%    load('\\bluebell\IMAGEBORG\STUDENTS\RRAIZADA\Corrected TINCAN\PigLung6_B2\Post
Formalin\Frame 492\segmentation.mat');

%      indx = 93; % when 400:700 frames used
%Frame 502

%    load('\\bluebell\IMAGEBORG\STUDENTS\RRAIZADA\Corrected TINCAN\PigLung6_B2\Post
Formalin\Frame 502\segmentation.mat');

%      indx = 103; % when 400:700 frames used
%Frame 530

%    load('\\bluebell\IMAGEBORG\STUDENTS\RRAIZADA\Corrected TINCAN\PigLung6_B2\Post
Formalin\Frame 530\segmentation.mat');

%      indx = 131; % when 400:700 frames used
%Frame 585

%    load('\\bluebell\IMAGEBORG\STUDENTS\RRAIZADA\Corrected TINCAN\PigLung6_B2\Post
Formalin\Frame 585\segmentation.mat');
```

```
%      indx = 186; % when 400:700 frames used
%Frame 607

%    load('\\bluebell\IMAGEBORG\STUDENTS\RRAIZADA\Corrected TINCAN\PigLung6_B2\Post
Formalin\Frame 607\segmentation.mat');

%      indx = 208; % when 400:700 frames used
%% PIG 7

%AUTOMATED
%load('\\bluebell\IMAGEBORG\STUDENTS\RRAIZADA\Corrected TINCAN\PigLung7_C1\Post
Formalin\AutomaticSegmentation\Trial4_BV(15,0_001)_lumen_450_to_750_pixel wiped below cartilage(like
5a)\matlab.mat');

%MANUAL
% start_frame = 450;
%Frame 516

%    load('\\bluebell\IMAGEBORG\STUDENTS\RRAIZADA\Corrected TINCAN\PigLung7_C1\Post
Formalin\Frame 516\segmentation.mat');

%      indx = 67; % when 450:750 frames used
%Frame 526

%    load('\\bluebell\IMAGEBORG\STUDENTS\RRAIZADA\Corrected TINCAN\PigLung7_C1\Post
Formalin\Frame 526\segmentation.mat');

%      indx = 77; % when 450:750 frames used
%Frame 556

%    load('\\bluebell\IMAGEBORG\STUDENTS\RRAIZADA\Corrected TINCAN\PigLung7_C1\Post
Formalin\Frame 556\segmentation.mat');

%      indx = 107; % when 450:750 frames used
%Frame 577

%    load('\\bluebell\IMAGEBORG\STUDENTS\RRAIZADA\Corrected TINCAN\PigLung7_C1\Post
Formalin\Frame 577\segmentation.mat');

%      indx = 128; % when 450:750 frames used
%Frame 590

%    load('\\bluebell\IMAGEBORG\STUDENTS\RRAIZADA\Corrected TINCAN\PigLung7_C1\Post
Formalin\Frame 590\segmentation.mat');

%      indx = 141; % when 450:750 frames used
%Frame 704

%    load('\\bluebell\IMAGEBORG\STUDENTS\RRAIZADA\Corrected TINCAN\PigLung7_C1\Post
Formalin\Frame 704\segmentation.mat');

%      indx = 255; % when 450:750 frames used
%% PIG 8
```

```
%AUTOMATED
% load('\\bluebell\IMAGEBORG\STUDENTS\RRAIZADA\Corrected TINCAN\PigLung8_A2\Post
Formalin\AutomaticSegmentation\Trial4_BV(15,0_001)_lumen_300_to_600_pixel wiped below cartilage(like
5a)\matlab.mat');

%MANUAL
% start_frame = 300;
%Frame 312

%    load('\\bluebell\IMAGEBORG\STUDENTS\RRAIZADA\Corrected TINCAN\PigLung8_A2\Post
Formalin\Frame 312\segmentation.mat');

%      indx = 13; % when 300:600 frames used
%Frame 449

%    load('\\bluebell\IMAGEBORG\STUDENTS\RRAIZADA\Corrected TINCAN\PigLung8_A2\Post
Formalin\Frame 449\segmentation.mat');

%      indx = 150; % when 300:600 frames used
%Frame 467

%    load('\\bluebell\IMAGEBORG\STUDENTS\RRAIZADA\Corrected TINCAN\PigLung8_A2\Post
Formalin\Frame 467\segmentation.mat');

%      indx = 168; % when 300:600 frames used
%Frame 514

%    load('\\bluebell\IMAGEBORG\STUDENTS\RRAIZADA\Corrected TINCAN\PigLung8_A2\Post
Formalin\Frame 514\segmentation.mat');

%      indx = 215; % when 300:600 frames used
%Frame 534

%    load('\\bluebell\IMAGEBORG\STUDENTS\RRAIZADA\Corrected TINCAN\PigLung8_A2\Post
Formalin\Frame 534\segmentation.mat');

%      indx = 235; % when 300:600 frames used
%Frame 558

%    load('\\bluebell\IMAGEBORG\STUDENTS\RRAIZADA\Corrected TINCAN\PigLung8_A2\Post
Formalin\Frame 558\segmentation.mat');

%      indx = 259; % when 300:600 frames used
%% PIG 10

%AUTOMATED
% load('\\bluebell\IMAGEBORG\STUDENTS\RRAIZADA\Corrected TINCAN\PigLung10_A1\Post
Formalin\AutomaticSegmentation\Trial4_BV(15,0_001)_lumen_550_to_850_pixel wiped below cartilage(like
5a)\matlab.mat');

%MANUAL
% start_frame = 550;
%Frame 645
```

```
%    load('\\bluebell\IMAGEBORG\STUDENTS\RRAIZADA\Corrected TINCAN\PigLung10_A1\Post Formalin\Frame 645\segmentation.mat');

%      indx = 96; % when 550:850 frames used
%Frame 683

%    load('\\bluebell\IMAGEBORG\STUDENTS\RRAIZADA\Corrected TINCAN\PigLung10_A1\Post Formalin\Frame 683\segmentation.mat');

%      indx = 134; % when 550:850 frames used
%Frame 755

%    load('\\bluebell\IMAGEBORG\STUDENTS\RRAIZADA\Corrected TINCAN\PigLung10_A1\Post Formalin\Frame 755\segmentation.mat');

%      indx = 206; % when 550:850 frames used
%Frame 764

%    load('\\bluebell\IMAGEBORG\STUDENTS\RRAIZADA\Corrected TINCAN\PigLung10_A1\Post Formalin\Frame 764\segmentation.mat');

%      indx = 215; % when 550:850 frames used
%Frame 777

%    load('\\bluebell\IMAGEBORG\STUDENTS\RRAIZADA\Corrected TINCAN\PigLung10_A1\Post Formalin\Frame 777\segmentation.mat');

%      indx = 228; % when 550:850 frames used
%Frame 790

%    load('\\bluebell\IMAGEBORG\STUDENTS\RRAIZADA\Corrected TINCAN\PigLung10_A1\Post Formalin\Frame 790\segmentation.mat');

%      indx = 241; % when 550:850 frames used


%% PIG 11

%AUTOMATED
% load('\\bluebell\IMAGEBORG\STUDENTS\RRAIZADA\Corrected TINCAN\PigLung11_B2\Post Formalin\AutomaticSegmentation\Trial4_BV(15,0_001)_lumen_450_to_750_pixel wiped below cartilage(like 5a)\matlab.mat');

%MANUAL
% start_frame = 450;
%Frame 550

%    load('\\bluebell\IMAGEBORG\STUDENTS\RRAIZADA\Corrected TINCAN\PigLung11_B2\Post Formalin\Frame 550\segmentation.mat');

%      indx = 101; % when 450:750 frames used
%Frame 565

%    load('\\bluebell\IMAGEBORG\STUDENTS\RRAIZADA\Corrected TINCAN\PigLung11_B2\Post Formalin\Frame 565\segmentation.mat');
```

```
%      indx = 116; % when 450:750 frames used
%Frame 576

%    load('\\bluebell\IMAGEBORG\STUDENTS\RRAIZADA\Corrected TINCAN\PigLung11_B2\Post Formalin\Frame 576\segmentation.mat');

%      indx = 127; % when 450:750 frames used
%Frame 589

%    load('\\bluebell\IMAGEBORG\STUDENTS\RRAIZADA\Corrected TINCAN\PigLung11_B2\Post Formalin\Frame 589\segmentation.mat');

%      indx = 140; % when 450:750 frames used
%Frame 598

%    load('\\bluebell\IMAGEBORG\STUDENTS\RRAIZADA\Corrected TINCAN\PigLung11_B2\Post Formalin\Frame 598\segmentation.mat');

%      indx = 149; % when 450:750 frames used
%Frame 607

%    load('\\bluebell\IMAGEBORG\STUDENTS\RRAIZADA\Corrected TINCAN\PigLung11_B2\Post Formalin\Frame 607\segmentation.mat');

%      indx = 158; % when 450:750 frames used
%% PIG 12

%AUTOMATED
  %load('\\bluebell\IMAGEBORG\STUDENTS\RRAIZADA\Corrected TINCAN\PigLung12_A3\Post Formalin\AutomaticSegmentation\Trial4_BV(15,0_001)_lumen_250_to_550_pixel wiped below cartilage(like 5a)\matlab.mat');

%MANUAL
   start_frame = 250;
%Frame 341

%    load('\\bluebell\IMAGEBORG\STUDENTS\RRAIZADA\Corrected TINCAN\PigLung12_A3\Post Formalin\Frame 341\segmentation.mat');

%      indx = 92; % when 250:550 frames used
%Frame 351

%    load('\\bluebell\IMAGEBORG\STUDENTS\RRAIZADA\Corrected TINCAN\PigLung12_A3\Post Formalin\Frame 351\segmentation.mat');

%      indx = 102; % when 250:550 frames used
%Frame 361

%    load('\\bluebell\IMAGEBORG\STUDENTS\RRAIZADA\Corrected TINCAN\PigLung12_A3\Post Formalin\Frame 361\segmentation.mat');

%      indx = 112; % when 250:550 frames used
%Frame 372
```

```
%    load('\\bluebell\IMAGEBORG\STUDENTS\RRAIZADA\Corrected TINCAN\PigLung12_A3\Post Formalin\Frame 372\segmentation.mat');

%      indx = 123; % when 250:550 frames used
%Frame 381

%    load('\\bluebell\IMAGEBORG\STUDENTS\RRAIZADA\Corrected TINCAN\PigLung12_A3\Post Formalin\Frame 381\segmentation.mat');

%      indx = 132; % when 250:550 frames used
%Frame 411

%    load('\\bluebell\IMAGEBORG\STUDENTS\RRAIZADA\Corrected TINCAN\PigLung12_A3\Post Formalin\Frame 411\segmentation.mat');

%      indx = 162; % when 250:550 frames used
  %% Lumen
x = BP{2,1}.Lumen(:,1);
y = BP{2,1}.Lumen(:,2);
%Max
maxobsv2L = max(y);
%Min
minobsv2L = min(y);
%Convert to a one to one function: # of x values = # of y values
[xs, ys, frequecnies] = One2One(x,y); clear x    y ;
  ys = ys';

%error
er_l = gcBM(:,indx) - ys;
er_l_sum = sum(er_l.^2);
er_l_rms = sqrt(er_l_sum/length(er_l)); clear er_l    er_l_sum ;

%Observer 1
y1 = BP{1,1}.Lumen(:,2);
x1 = BP{1,1}.Lumen(:,1);
%Max
maxobsv1L = max(y1);
%Min
minobsv1L = min(y1);
[xs1, ys1, frequecnies1] = One2One(x1,y1); clear x1    y1 ;
  ys1 = ys1';
%error
er_l1 = gcBM(:,indx) - ys1;
er_l_sum1 = sum(er_l1.^2);
er_l_rms1 = sqrt(er_l_sum1/length(er_l1)); clear er_l1    er_l_sum1 ;


%MAX Automated
maxgc_lumen = max(gcBM(:,indx));
%Min
mingc_lumen = min(gcBM(:,indx));
```

```
%interobserver error
er_obsvl = ys - ys1;
er_obsvl_sum = sum(er_obsvl.^2);
er_obsv_rms_Lum = sqrt(er_obsvl_sum /length(er_obsvl)); clear er_obsvl  er_obsvl_sum ;

%% Dice Coefficient
% segIm = gcBM(:,indx);
% % similarity with obsv1
% grndTruth1 = ys1;
% [Jaccard1,Dice1,rfp1,rfn1]=sevaluate(grndTruth1(:,1),segIm); clear Jaccard1 rfp1 rfn1
% %dice1 = 2*nnz(segIm&grndTruth1)/(nnz(segIm) + nnz(grndTruth1));
% % similarity with obsv2
% grndTruth2 = ys;
% [Jaccard1,Dice2,rfp1,rfn1]=sevaluate(grndTruth2,segIm); clear Jaccard1 rfp1 rfn1
% %dice2 = 2*nnz(segIm&grndTruth2)/(nnz(segIm) + nnz(grndTruth2));
% % inter-observer similarity
% [Jaccard1,Dice_inter,rfp1,rfn1]=sevaluate(grndTruth1,grndTruth2); clear Jaccard1 rfp1 rfn1
% %dice_inter = 2*nnz(grndTruth1&grndTruth2)/(nnz(grndTruth1) + nnz(grndTruth2));
%%
%% Mucosa
x_m = BP{2,1}.Mucosa(:,1);
y_m = BP{2,1}.Mucosa(:,2);
%Max
maxobsv2M = max(y_m);
%Min
minobsv2M = min(y_m);
[xs_m, ys_m, frequecnies_m] = One2One(x_m,y_m); clear x_m  y_m ;
  ys_m = ys_m';
%error
er_m = gcBM2(:,indx) - ys_m;
er_m_sum = sum(er_m.^2);
er_m_rms = sqrt(er_m_sum/length(er_m)); clear er_m  er_m_sum ;

%Observer 1
y_m1 = BP{1,1}.Mucosa(:,2);
x_m1 = BP{1,1}.Mucosa(:,1);
%Max
maxobsv1M = max(y_m1);
%Min
minobsv1M = min(y_m1);
[xs_m1, ys_m1, frequecnies_m1] = One2One(x_m1,y_m1); clear x_m1  y_m1 ;
ys_m1 = ys_m1';
%error
er_m1 = gcBM2(:,indx) - ys_m1;
er_m_sum1 = sum(er_m1.^2);
er_m_rms1 = sqrt(er_m_sum1/length(er_m1)); clear er_m1  er_m_sum1 ;

%MAX Automated
maxgc_mucosa = max(gcBM2(:,indx));
%Min
mingc_mucosa = min(gcBM2(:,indx));
%interobserver error
er_obsvm = ys_m - ys_m1;
```

```
er_obsvm_sum = sum(er_obsvm.^2);
er_obsv_rms_MUC = sqrt(er_obsvm_sum /length(er_obsvm)); clear er_obsvm   er_obsvm_sum ;

%% Cartilage
x_c = BP{2,1}.Cartilage(:,1);
y_c = BP{2,1}.Cartilage(:,2);
%Max
maxobsv2C = max(y_c);
%Min
minobsv2C = min(y_c);
[xs_c, ys_c, frequecnies_c] = One2One(x_c,y_c); clear x_c   y_c ;
ys_c = ys_c';
%error
er_c = gcBM3(:,indx) - ys_c;
er_c_sum = sum(er_c.^2);
er_c_rms = sqrt(er_c_sum/length(er_c)); clear er_c   er_c_sum ;

%Observer 1
x_c1 = BP{1,1}.Cartilage(:,1);
y_c1 = BP{1,1}.Cartilage(:,2);
%Max
maxobsv1C = max(y_c1);
%Min
minobsv1C = min(y_c1);
[xs_c1, ys_c1, frequecnies_c1] = One2One(x_c1,y_c1); clear x_c1   y_c1 ;
ys_c1 = ys_c1';
%error
er_c1 = gcBM3(:,indx) - ys_c1;
er_c_sum1 = sum(er_c1.^2);
er_c_rms1 = sqrt(er_c_sum1/length(er_c1)); clear er_c1   er_c_sum1 ;

%MAX Automated
maxgc_cart = max(gcBM3(:,indx));
%Min Automated
mingc_cart = min(gcBM3(:,indx));

%interobserver error
er_obsvc = ys_c - ys_c1;
er_obsvc_sum = sum(er_obsvc.^2);
er_obsv_rms_CART = sqrt(er_obsvc_sum /length(er_obsvc)); clear er_obsvc   er_obsvc_sum ;
%% Plot result
figure
%ground truth observer 1
subplot(3,1,1);imagesc(matvol_or(:,:,indx)), colormap( 'gray' )
title( 'Observer 1' );
hold on
    plot(xs1,ys1, 'm' , 'LineWidth' ,2) %Lumen
    plot(xs_m1,ys_m1, 'g' , 'LineWidth' ,2) %Mucosa
    plot(xs_c1,ys_c1, 'r' , 'LineWidth' ,2) %Cartilage
%ground truth observer 2
subplot(3,1,2);imagesc(matvol_or(:,:,indx)), colormap( 'gray' )
```

```
title( 'Observer 2' );
hold on
    plot(xs,ys, 'm' , 'LineWidth' ,2) %Lumen
    plot(xs_m,ys_m, 'g' , 'LineWidth' ,2) %Mucosa
    plot(xs_c,ys_c, 'r' , 'LineWidth' ,2) %Cartilage
% Automatic segmentation
subplot(3,1,3);imagesc(matvol_or(:,:,indx)), colormap( 'gray' )
title(start_frame+indx-1);
hold on
    plot(1:size(gcBM,1),gcBM(:,indx), 'm' , 'LineWidth' ,2) %Lumen
    plot(1:size(gcBM2,1),gcBM2(:,indx), 'g' , 'LineWidth' ,2) %Mucosa
    plot(1:size(gcBM3,1),gcBM3(:,indx), 'r' , 'LineWidth' ,2) %Cartilage
```

Appendix F: Matlab script for Areas

```
%% Area
% per frame
% To be used after RmsErrorCorrected
% y's, index come from RmsErrorCorrected

% OFFSETS
% PIG2
% offset = -0.273;
% PIG3
% offset = -0.172;
% PIG 4
% offset = -0.107;
% PIG 5
% offset = -0.128;
% PIG 6
% offset = -0.107;
% PIG 7
% offset = -0.078;
% PIG 8
% offset = -0.201;
% PIG 10
% offset = -0.0561;
% PIG 11
% offset = -0.0344;
%PIG 12
offset = -0.0200;

% r vector
r_calib = 0.00723; % mm/pix
r_lum_obsv1 = ys1*r_calib + offset;
r_lum_obsv2 = ys*r_calib + offset;
r_lum_auto = gcBM(:,indx)*r_calib + offset;

r_muc_obsv1 = ys_m1*r_calib+ offset;
```

```
r_muc_obsv2 = ys_m*r_calib+ offset;
r_muc_auto = gcBM2(:,indx)*r_calib+ offset;

r_cart_obsv1 = ys_c1*r_calib+ offset;
r_cart_obsv2 = ys_c*r_calib+ offset;
r_cart_auto = gcBM3(:,indx)*r_calib+ offset;



% theta vector
theta_calib = 0.01246; % mm/pix
vector = [1:504]';
theta = vector*theta_calib;



% Polar area

%lumen
A_lum_obsv1 = 0.5*trapz(theta,r_lum_obsv1);
A_lum_obsv2 = 0.5*trapz(theta,r_lum_obsv2);
A_lum_auto = 0.5*trapz(theta,r_lum_auto);

%Mucosa
A_muc_obsv1 = 0.5*trapz(theta,r_muc_obsv1);
A_muc_obsv2 = 0.5*trapz(theta,r_muc_obsv2);
A_muc_auto = 0.5*trapz(theta,r_muc_auto);

%Cartilage
A_cart_obsv1 = 0.5*trapz(theta,r_cart_obsv1);
A_cart_obsv2 = 0.5*trapz(theta,r_cart_obsv2);
A_cart_auto = 0.5*trapz(theta,r_cart_auto);

% Array of areas
Arr = [A_lum_obsv1, A_lum_obsv2, A_lum_auto,A_muc_obsv1,A_muc_obsv2, A_muc_auto,A_cart_obsv1,
A_cart_obsv2, A_cart_auto];
% rows PIG2(4:9),PIG3(10:15),PIG4(16:21), PIG5(22:27), PIG6(28:33),
% PIG7(34:39), PIG8(40:45), PIG10(46:51), PIG11(52:57), PIG12(58:63)
xlswrite( '\\bluebell\IMAGEBORG\STUDENTS\RRAIZADA\Corrected TINCAN\Excel Data for Parameter
Optimization\Trial4_BV(15,0_001)_lumen\All pigs-(a)\Polar Areas with offsets.xls' ,Arr, 'B63:J63' );
```

Appendix F: Matlab script for Jaccard Indices

```
  %To be used after RmsErrorCorrected

%% Lumen
```

```
original = matvol_or(:,:,indx);
im_lum1 = matvol_or(:,:,indx); %obsv1
im_lum2 = matvol_or(:,:,indx); %obsv2
im_lum_aut = matvol_or(:,:,indx); %automated
figure, imagesc(original),colormap( 'gray' );

%Dice image for obsv1
for i = 1: size(im_lum2 ,1) % 500 points (depth)
    for j = 1: size(im_lum2 ,2) % 504 points


if ( i > ys1(j))

im_lum1(i,j) =0;

else

im_lum1(i,j) =255;

end
    end
end
figure, imagesc(im_lum1),colormap( 'gray' );
%Dice image for obsv2
for i = 1: size(im_lum2 ,1) % 500 points (depth)
    for j = 1: size(im_lum2 ,2) % 504 points


if ( i > ys(j))

im_lum2(i,j) =0;

else

im_lum2(i,j) =255;

end
    end
end

%Dice image for automated
for i = 1: size(im_lum2 ,1) % 500 points (depth)
    for j = 1: size(im_lum2 ,2) % 504 points


if ( i > gcBM(j,indx))

im_lum_aut(i,j) =0;

else
```

```
im_lum_aut(i,j) =255;

end
     end
end
%JACCARD
  [Jaccard_L_inter,Dice,rfp,rfn]=sevaluate(im_lum1,im_lum2);
  [Jaccard_L_obsv1,Dice,rfp,rfn]=sevaluate(im_lum1,im_lum_aut);
  [Jaccard_L_obsv2,Dice,rfp,rfn]= sevaluate(im_lum2,im_lum_aut);clear Dice  rfp  rfn


  %% Mucosa
im_m1 = matvol_or(:,:,indx); %obsv1
im_m2 = matvol_or(:,:,indx); %obsv2
im_m_aut = matvol_or(:,:,indx); %automated

%Dice image for obsv1
for i = 1: size(im_m2 ,1) % 500 points (depth)
     for j = 1: size(im_m2 ,2) % 504 points


if ( i > ys_m1(j))

im_m1(i,j) =0;

else

im_m1(i,j) =255;

end
     end
end
figure, imagesc(im_m1),colormap( 'gray' );;
%Dice image for obsv2
for i = 1: size(im_m2 ,1) % 500 points (depth)
     for j = 1: size(im_m2 ,2) % 504 points
        if ( i > ys_m(j))

im_m2(i,j) =0;
        else

im_m2(i,j) =255;

end
     end
end

%Dice image for automated
for i = 1: size(im_m2 ,1) % 500 points (depth)
```

```
      for j = 1: size(im_m2 ,2) % 504 points

if ( i >gcBM2(j,indx))

im_m_aut(i,j) =0;

else

im_m_aut(i,j) =255;

end
      end
end
%JACCARD
  [Jaccard_M_inter,Dice,rfp,rfn]=sevaluate(im_m1,im_m2);
  [Jaccard_M_obsv1,Dice,rfp,rfn]= sevaluate(im_m1,im_m_aut);
  [Jaccard_M_obsv2,Dice,rfp,rfn]= sevaluate(im_m2,im_m_aut);clear Dice   rfp   rfn

   %% Cartilage
im_c1 = matvol_or(:,:,indx); %obsv1
im_c2 = matvol_or(:,:,indx); %obsv2
im_c_aut = matvol_or(:,:,indx); %automated

%Dice image for obsv1
for i = 1: size(im_c2 ,1) % 500 points (depth)
      for j = 1: size(im_c2 ,2) % 504 points

if ( i > ys_c1(j))

im_c1(i,j) =0;

else

im_c1(i,j) =255;

end
      end
end
figure, imagesc(im_c1),colormap( 'gray' );;
%Dice image for obsv2
for i = 1: size(im_c2 ,1) % 500 points (depth)
      for j = 1: size(im_c2 ,2) % 504 points
         if ( i > ys_c(j))

im_c2(i,j) =0;
         else
```

```
im_c2(i,j) =255;

end
     end
end

%Dice image for automated
for i = 1: size(im_c2 ,1) % 500 points (depth)
     for j = 1: size(im_c2 ,2) % 504 points


if ( i >gcBM3(j,indx))

im_c_aut(i,j) =0;

else

im_c_aut(i,j) =255;

end
     end
end
%JACCARD
  [Jaccard_C_inter,Dice,rfp,rfn]=sevaluate(im_c1,im_c2);
  [Jaccard_C_obsv1,Dice,rfp,rfn]= sevaluate(im_c1,im_c_aut);
  [Jaccard_C_obsv2,Dice,rfp,rfn]= sevaluate(im_c2,im_c_aut);clear Dice   rfp   rfn
```

References

1. Yang P, Sun Z, Krowka MJ, Aubry MC, Bamlet WR, et al. (2008) Alpha1-antitrypsin deficiency carriers, tobacco smoke, chronic obstructive pulmonary disease, and lung cancer risk. Arch Intern Med 168: 1097–1103.
2. Nakawah, M. O., Hawkins, C., & Barbandi, F. (2013). Asthma, chronic obstructive pulmonary disease (COPD), and the overlap syndrome. *The Journal of the American Board of Family Medicine*, *26*(4), 470-477.
3. Canadian Lung Association. “Lung Facts.” 1994 Update.
4. Athanazio, R. (2012). Airway disease: similarities and differences between asthma, COPD and bronchiectasis. *Clinics*, *67*(11), 1335-1343.
5. Hogg, J. C. (2004). Pathophysiology of airflow limitation in chronic obstructive pulmonary disease. *The Lancet*, *364*(9435), 709-721.
6. Yanai, M., Sekizawa, K. I. Y. O. H. I. S. A., Ohrui, T. A. K. A. S. H. I., Sasaki, H. I. D. E. T. A. D. A., & Takishima, T. A. M. O. T. S. U. (1992). Site of airway obstruction in pulmonary disease: direct measurement of intrabronchial pressure. *J Appl Physiol*, *72*(3), 1016-1023.
7. Mullen, J. B., Wright, J. L., Wiggs, B. R., Pare, P. D., & Hogg, J. C. (1985). Reassessment of inflammation of airways in chronic bronchitis. *British medical journal (Clinical research ed.)*, *291*(6504), 1235.
8. Dunnill MS, Massarella GR, Anderson JA. A comparison of the quantitative anatomy of the bronchi in normal subjects, in status asthmaticus, in chronic bronchitis, and in emphysema. *Thorax* 1969; **24:** 176–79.
9. Fabbri, L. M., Romagnoli, M., Corbetta, L., Casoni, G., Busljetic, K., Turato, G., ... & Papi, A. (2003). Differences in airway inflammation in patients with fixed airflow obstruction due to asthma or

chronic obstructive pulmonary disease.*American journal of respiratory and critical care medicine*, *167*(3), 418-424.

10. Jeffery, P. K. (2001). Remodeling in asthma and chronic obstructive lung disease. *American journal of respiratory and critical care medicine*,*164*(supplement_2), S28-S38.
11. Asthma Society of Canada (2014, July 2). "*What Is Asthma?".* Retrieved from http://www.asthma.ca/adults/about/whatIsAsthma.php
12. World Health Organization. *Global surveillance, prevention and control of chronic respiratory diseases: a comprehensive approach, 2007*.
13. L-P Boulet, TR Bai, A Becker, et al. What is new since the last (1999) Canadian Asthma Consensus Guidelines? Can Respir J 2001;8(Suppl A): 5A-27A.
14. ref 13 in Airway pathogenesis
15. Coxson HO, Rogers RM, Whittall KP, et al. A quantification of the lung surface area in emphysema using computed tomography. *J Respir Crit Care Med* 1999; **159:** 851–56.
16. Bai A, Eidelman DH, Hogg JC, James AL, Lambert RK, et al. (1 393 994) Proposed nomenclature for quantifying subdivisions of the bronchial wall. Journal of Applied Physiology 77: 1011-1014.
17. Lambert, R. K. (1991). Role of bronchial basement membrane in airway collapse. *J Appl Physiol*, *71*(2), 666-73.
18. Miranda Kirby ; Anthony M. D. Lee ; Tara Candido ; Calum MacAulay ; Pierre Lane ; Stephen Lam ; Harvey O. Coxson. Automated segmentation of porcine airway wall layers using optical coherence tomography: comparison with manual segmentation and histology. Proc. SPIE 8927, Endoscopic Microscopy IX; and Optical Techniques in Pulmonary Medicine, 89271D (March 4, 2014); doi:10.1117/12.2040866.
19. Optical coherence tomography. (2014, June 13). In *Wikipedia, The Free Encyclopedia*. Retrieved 05:07, July 19, 2014, from http://en.wikipedia.org/wiki/Optical_coherence_tomography

20. Whiteman, S. C., Yang, Y., van Pittius, D. G., Stephens, M., Parmer, J., & Spiteri, M. A. (2006). Optical coherence tomography: real-time imaging of bronchial airways microstructure and detection of inflammatory/neoplastic morphologic changes. *Clinical Cancer Research*, *12*(3), 813-818.
21. Lee AMD, Kirby M, Ohtani K, Candido T, Shalansky R, et al. (2014) Validation of Airway Wall Measurements by Optical Coherence Tomography in Porcine Airways. PLoS ONE 9(6): e100145. doi:10.1371/journal.pone.0100145
22. Tsuboi, M., Hayashi, A., Ikeda, N., Honda, H., Kato, Y., Ichinose, S., & Kato, H. (2005). Optical coherence tomography in the diagnosis of bronchial lesions.*Lung Cancer*, *49*(3), 387-394.
23. Hanna, N., Saltzman, D., Mukai, D., Chen, Z., Sasse, S., Milliken, J., ... & Brenner, M. (2005). Two-dimensional and 3-dimensional optical coherence tomographic imaging of the airway, lung, and pleura. *The Journal of thoracic and cardiovascular surgery*, *129*(3), 615-622.
24. M. Kaus, S. K. Warfield, F. A. Jolesz, and R. Kikinis. Adaptive template moderated brain tumor segmentation in MRI. In Bildverarbeitung fur die Medizin, pages 102–106. Springer Verlag, 1998
25. Heydarian, M., Choy, S., Wheatley, A., McCormack, D., Coxson, H. O., Lam, S., & Parraga, G. (2011, March). Automated segmentation of lung airway wall area measurements from bronchoscopic optical coherence tomography imaging. In *SPIE Medical Imaging* (pp. 79651M-79651M). International Society for Optics and Photonics.
26. Lee, S., Fallah, N., Forooghian, F., Ko, A., Pakzad-Vaezi, K., Merkur, A. B., ... & Beg, M. F. (2013). Comparative analysis of repeatability of manual and automated choroidal thickness measurements in nonneovascular age-related macular degeneration. *Investigative ophthalmology & visual science*, *54*(4), 2864-2871.
27. Li K, Wu X, Chen DZ, Sonka M. Optimal surface segmentation in volumetric images – a graph-theoretic approach. *IEEE T Pattern Anal*. 2006;28:119–134.

28. Coxson, H. O., Quiney, B., Sin, D. D., Xing, L., McWilliams, A. M., Mayo, J. R., & Lam, S. (2008). Airway wall thickness assessed using computed tomography and optical coherence tomography. *American journal of respiratory and critical care medicine*, *177*(11), 1201-1206.
29. Heydarian, M., Choy, S., Wheatley, A., McCormack, D., Coxson, H. O., Lam, S., & Parraga, G. (2011, March). Automated segmentation of lung airway wall area measurements from bronchoscopic optical coherence tomography imaging. In *SPIE Medical Imaging* (pp. 79651M-79651M). International Society for Optics and Photonics.
30. Bernardes, R., Maduro, C., Serranho, P., Araújo, A., Barbeiro, S., & Cunha-Vaz, J. (2010). Improved adaptive complex diffusion despeckling filter. *Optics express*, *18*(23), 24048-24059.
31. G. Gilboa, N. Sochen, and Y. Y. Zeevi, "Image enhancement and denoising by complex diffusion processes," IEEE Trans. Pattern Anal. Mach. Intell. 26(8), 1020–1036 (2004).
32. L. Younes, "Mathematical image analysis," Center for Imaging Sciences.Institute for Computational Medicine, Johns Hopkins University.
33. Otsu, N. (1975). A threshold selection method from gray-level histograms.*Automatica*, *11*(285-296), 23-27.
34. Canny edge detector. (2014, August 9). In *Wikipedia, The Free Encyclopedia*. Retrieved 04:27, November 16, 2014, from http://en.wikipedia.org/w/index.php?title=Canny_edge_detector&oldid=620521247
35. K-means clustering. (2014, November 11). In *Wikipedia, The Free Encyclopedia*. Retrieved 09:00, November 17, 2014, fromhttp://en.wikipedia.org/w/index.php?title=K-means_clustering&oldid=633411037
36. Frangi, A. F., Niessen, W. J., Vincken, K. L., & Viergever, M. A. (1998). Multiscale vessel enhancement filtering. In *Medical Image Computing and Computer-Assisted Intervention—MICCAI'98* (pp. 130-137). Springer Berlin Heidelberg.

37. Convex hull. (2014, November 2). In *Wikipedia, The Free Encyclopedia*. Retrieved 04:46, November 16, 2014, from http://en.wikipedia.org/w/index.php?title=Convex_hull&oldid=632173115

38. M. Sonka, V. Hlavac, and R. Boyle, Image Processing, Analysis, and Machine Vision, second ed. Brooks/Cole Publishing Company,1999.